



Trinity College Dublin
Coláiste na Tríonóide, Baile Átha Cliath
The University of Dublin

Metal Nanoparticles for application in Luminescent Solar Concentrators

A Thesis submitted to the University of Dublin for the
degree of Doctor of Philosophy

April 2020

Prepared by:
Arunima Sethi

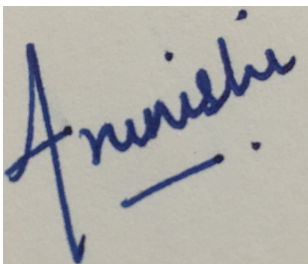
Supervisor: Asst. Prof. Dr. Sarah McCormack
Co-Supervisors: Dr. Subhash Chandra
Dr. Hind Ahmed

Department of Civil, Structural and Environmental
Engineering
University of Dublin
Trinity College Dublin

Declaration

I declare that this thesis has not been submitted as an exercise for a degree at this or any other university and it is entirely my own work.

I agree to deposit this thesis in the University's open access institutional repository or allow the library to do so on my behalf, subject to Irish Copyright Legislation and Trinity College Library conditions of use and acknowledgement.

A handwritten signature in blue ink, reading "Arunima Sethi". The signature is written in a cursive style with a long vertical stroke for the letter 'A'.

Arunima Sethi

September 2019

Abstract

Rising global temperature calls for innovative ways to deal with the ever-growing energy demand. Luminescent Solar Concentrators (LSC) are low concentration, solar radiation collectors. LSCs have the potential to be used as building-integrated photovoltaics due to their ability to be architecturally integrated into the facade without compromising the aesthetic of the building. They can concentrate both diffuse and direct solar radiation and that is essential for northern latitude countries where 50% of solar radiation can be diffuse. The various energy loss mechanisms in LSC inhibit the device efficiency from reaching its thermodynamic limit. Plasmonic LSC (PLSC) is a novel concept to reduce the escape cone losses and increase the edge power output of an LSC device. A PLSC comprises of metal nanoparticles (MNPs) and fluorophores embedded in an optical waveguide. The plasmonic coupling between the fluorophore and MNP can increase the fluorescence intensity of the fluorophore by increasing its excitation or emission rate or both. In this Ph.D., work is carried out to synthesize MNPs for application in PLSC and to fabricate and test PLSC device in the European climate.

Anisotropic MNPs were synthesized to tune the surface plasmon resonance band position to the absorption or emission peak of the fluorophore. A 1.2 times increase in the power conversion efficiency was observed for optimized PLSC device as compared to an LSC without any MNPs. PLSC device was studied in different lighting conditions outdoors and higher efficiency than bare PV cell was observed in diffuse radiation. As compared to the month of July, the PLSC device performs 45% better than the PV cell in December.

To my spiritual master Nalin K. Nirula

Acknowledgements

The past four years were a great learning curve for me and I would like to take this opportunity to express my heartfelt gratitude. This doctoral thesis would not have been possible without the insurmountable help and support of many people who not only helped in the completion of this thesis but also in making me a better human. Like with any research I faced many technical challenges during the beginning of this project and they were overcome with the help of researchers and technicians from Trinity College Dublin.

First and foremost I would like to express my heartfelt gratitude to the thesis supervisor Dr. Sarah McCormack. Throughout my time in TCD, Sarah has shown utmost patience with me even when I felt demotivated during the difficult times. During the course of my thesis, I was able to attend many esteemed international conferences because of Sarah's constant encouragement. Due acknowledgment is also given to the funding agencies European Research Council and Science Foundation of Ireland for the funding of the project PEDAL and my scholarship.

A sincere thanks go to my co-supervisors Dr. Subhash Chandra and Dr. Hind Ahmed for the countless discussions throughout the course of the Ph.D. They were always available to help and guide me when I was confused regarding the subject matter and methodology. They encouraged me to write journal articles and instilled in me the art of independent research.

I would also like to extend my thanks to the technicians and experimental staff of the various departments in TCD for helping in the realization of the devices. Sincere thanks to Dr. Eoin McCarthy from AML, CRANN for taking the TEM im-

ages. David McAuley and Mark Gilligan for making the molds for the LSC/PLSC devices and for sharing innumerable laughs and light-hearted conversations. Mary O'Shea and Robert Fitzpatrick for helping in the outdoor setup of the LSC/PLSC system. Patrick Veale for always being helpful in getting chemicals at short notices for the experiments. Dr. Manuel Reuther and Christopher Smith for giving the training on Fluoromax and Cary-50 respectively.

Another aspect of the thesis work is the support and inspiration I got from my colleagues who have also become my friends in the course of four years in TCD. Mehran Rafiee for the countless late evening discussions in the office while also sharing the joys and sorrows of Ph.D. life. Sarah Gilligan for the laughs and conversations. Anita Ortega for helping in the outdoor setup of the PLSC/LSC devices, without whom the outdoor experiments would not have been as much fun.

None of this would have been possible without the love and support of my parents. They always believed in me and instilled in me the values to be a strong independent woman and I am grateful to them for that. A special mention to my brother Raghav for the laughs and conversations. A heartfelt thanks to Dhruv for the formatting of this thesis and the invaluable encouragement during difficult times. A special thanks to Gary for being extremely supportive and for all the hiking trips. Last but not the least a big thanks to all my friends in Dublin and back home in India for the much-needed breaks from work.

Arunima Sethi

Contents

| | |
|---|--------------|
| Declaration | iii |
| Abstract | v |
| Aknowledgements | ix |
| Contents | xiv |
| List of Figures | xxii |
| List of Tables | xxiii |
| 1 Introduction | 1 |
| 1.1 Photovoltaic Technologies | 2 |
| 1.2 Research Objectives | 6 |
| 1.3 Thesis roadmap | 6 |
| 2 Literature Review | 9 |
| 2.1 Operating Parameters of a PV cell | 9 |
| 2.2 Concentration Photovoltaics | 11 |
| 2.3 LSC Review | 13 |
| 2.3.1 Fluorophores | 15 |
| 2.4 Operating Parameters of LSC | 17 |
| 2.5 Energy loss mechanisms in an LSC | 18 |
| 2.6 Recent advances in LSC | 21 |

| | | |
|----------|--|-----------|
| 2.7 | SPR Revision | 27 |
| 2.8 | Surface plasmon resonance in MNPs | 28 |
| 2.9 | Local electric field enhancement | 29 |
| 2.10 | Factors influencing the SPR | 30 |
| 2.11 | Metal enhanced fluorescence | 33 |
| 2.12 | Silver a unique metal for plasmonics | 36 |
| 2.13 | Alignment of nanorods in external electric field | 37 |
| 2.14 | Synthesis of Gold Nanorods | 38 |
| 2.15 | Synthesis of gold core silver shell nanocuboids | 41 |
| 2.16 | Conclusions | 43 |
| 3 | Materials and methods | 45 |
| 3.1 | Materials | 45 |
| 3.2 | Centrifugation | 48 |
| 3.3 | UV-VIS spectrometry | 49 |
| 3.3.1 | Transmission measurement of solid samples | 51 |
| 3.4 | Scanning electron microscopy | 51 |
| 3.4.1 | Transmission electron microscopy | 54 |
| 3.5 | ICP-MS | 54 |
| 3.6 | Fluorescence spectroscopy | 56 |
| 3.6.1 | PLQY of solid samples | 57 |
| 3.7 | Device fabrication | 59 |
| 3.8 | LSC/PLSC characterization | 61 |
| 3.8.1 | Optical characterization | 61 |
| 3.8.2 | Indoor electrical characterization | 62 |
| 3.8.3 | Outdoor electrical characterization | 63 |
| 3.9 | Conclusions | 66 |
| 4 | MNP Nanocomposite | 69 |
| 4.1 | Synthesis of anisotropic MNPs | 70 |

| | |
|---|------------|
| <i>CONTENTS</i> | xiii |
| 4.1.1 Synthesis of gold nanorods | 70 |
| 4.1.2 Synthesis of gold core silver shell nanocuboids | 72 |
| 4.1.3 Reproducibility of Au NRs and Au@Ag NCs synthesis | 74 |
| 4.2 Purification of anisotropic MNPs | 76 |
| 4.2.1 Purification of gold nanorods | 77 |
| 4.2.2 Purification of gold core silver shell nanocuboids | 78 |
| 4.3 Morphology analysis of anisotropic MNPs | 80 |
| 4.3.1 Morphology analysis of gold nanorods | 80 |
| 4.3.2 Morphology analysis of gold core silver shell nanocuboids | 80 |
| 4.4 Concentration of MNPs | 83 |
| 4.4.1 Assumptions made to calculate MNP concentration | 85 |
| 4.5 Surface functionalization | 85 |
| 4.6 Phase transfer of anisotropic MNPs | 88 |
| 4.7 MNPs in Silicone polymer | 92 |
| 4.8 Conclusions | 93 |
| 5 LSC Characterization | 95 |
| 5.1 Fluorophore characterization | 96 |
| 5.2 Red305 LSC | 99 |
| 5.2.1 Absorption profile of Red305 LSC | 99 |
| 5.2.2 Total emission profile of Red305 LSC | 100 |
| 5.2.3 Edge emission profile of Red305 LSC | 102 |
| 5.3 Outdoor electrical characterization | 104 |
| 5.4 Diffuse reflectors | 107 |
| 5.4.1 Titanium Dioxide nanoparticles for diffuse reflectors | 108 |
| 5.5 Conclusions | 112 |
| 6 Plasmonic LSC | 115 |
| 6.1 Red305 dye and Au@Ag NCs PLSC | 116 |
| 6.2 Edge emission of PLSC | 118 |

| | | |
|----------|--|------------|
| 6.3 | Indoor performance of plasmonic luminescent solar concentrator . . | 121 |
| 6.4 | Outdoor performance of PLSC | 122 |
| 6.4.1 | Effect of sun's position on performance | 125 |
| 6.4.2 | Effect of light intensity on performance | 126 |
| 6.4.3 | Effect of diffuse reflector on performance | 128 |
| 6.4.4 | Seasonal performance of PLSC device | 128 |
| 7 | Conclusions and Future work | 133 |
| 7.1 | Contribution to knowledge | 135 |
| 7.2 | Recommendations for future work | 136 |
| | Appendices | 139 |
| | Appendix A Silver Nanowires | 141 |
| A.1 | Detailed synthesis process of Ag NRs | 141 |
| A.2 | Optical properties of silver nanorods | 144 |
| A.3 | Purification of the silver nanorods | 145 |
| A.4 | Morphology analysis of silver nanorods | 146 |
| A.5 | Challenges in Ag NR synthesis | 146 |
| | Appendix B Gold nanospheres Quantitation | 149 |
| | Appendix C Lumogen Yellow083 dye in Silicone | 153 |
| | List of Publications | 157 |
| | References | 178 |

List of Figures

| | | |
|-----|--|----|
| 1.1 | World's total primary energy supply by fuel in 2016 (IEA, 2016) . . . | 1 |
| 1.2 | Global total solar PV installed capacity. Data taken from (<i>Global-MarketOutlook 2018</i>). | 3 |
| 1.3 | Efficiency and cost projections of (I), (II) and (III) generation PV technologies (Conibeer, 2007) | 3 |
| 1.4 | Different generations and existing technologies of PV. | 5 |
| 2.1 | Graph of cell output current (red line) and power (blue line) as a function of voltage. | 10 |
| 2.2 | Loss processes in a standard solar cell: (1) thermalization losses, (2) recombination losses, (3) junction losses. | 11 |
| 2.3 | Direct normal irradiation and global horizontal irradiation for Dublin in 2016. Data available in (<i>SolarEuropa PVGIS</i>). | 13 |
| 2.4 | Red-dye LSC illuminated in the center by a light source. | 14 |
| 2.5 | a) LSC based greenhouse (Corrado et al., 2016), b) LSC based roof tiles 'Leaf Roof' (Reinders et al., 2016). | 15 |
| 2.6 | a) Jablonski energy level diagram of an organic dye, b) Hypothetical electronic absorption and emission bands showing transition from ground state to lowest excited energy state. | 16 |
| 2.7 | Cross-section of an LSC device with PV cell attached to one edge. . . | 19 |

| | | |
|------|---|----|
| 2.8 | PLQY of different dyes vs their emission wavelength. The red data point corresponds to Lumogen Red305 dye. Adapted from (Zastrow, 1994). | 20 |
| 2.9 | Photograph and schematic representation of a neutral-density LSC consisting of QDs. | 23 |
| 2.10 | Tandem LSCs and LSCs with photonic band filters. | 24 |
| 2.11 | Schematic of thin-film and stacked plate LSCs with MNPs. | 26 |
| 2.12 | Schematic of LSC in PV windows and panels. | 26 |
| 2.13 | Schematic of light interaction with a spherical MNP. | 27 |
| 2.14 | Illustration of electric field created by a MNP. | 29 |
| 2.15 | Extinction spectra of differently shaped Au and Ag MNPs. | 30 |
| 2.16 | Effect of the surface chemicals on SPR of MNPs. | 32 |
| 2.17 | Mie model calculation of SPR of 20 nm Au MNPs. | 33 |
| 2.18 | a) Simplified Jablonski diagram of fluorophore in the presence of MNP depicted with black and red arrows respectively, b) Illustration of high photon mode density in the presence of MNP around a fluorophore. | 35 |
| 2.19 | Plot of the imaginary and real part of the dielectric function as a function of wavelength. | 37 |
| 2.20 | Sketch of the dipole moment on nanorod | 38 |
| 2.21 | TEM images of Au NRs synthesized by various methods. | 39 |
| 2.22 | TEM images of Au@Ag nanocuboids capped with a) CTAC, b) BDAC, c) Citrate, d) PVP. Adapted from (Liu and Guyot-Sionnest, 2004, Tebbe et al., 2015). | 42 |
| 3.1 | Schematic of a centrifuge tube with particles inside that need to be separated and the various forces acting on the particle | 48 |
| 3.2 | Photograph of a) centrifuge b) rotor used in this work, c) diagram of a centrifuge tube with pellet and supernatant after centrifugation. | 49 |

| | | |
|------|--|----|
| 3.3 | Simplified optics ray diagram of a single beam configuration, with the photographs of the light source and spectrophotometer used in this study. | 50 |
| 3.4 | Schematic of an integrating sphere showing different sample placement for transmission and total reflectance measurement of solid samples. | 52 |
| 3.5 | Simplified schematic of an SEM showing the main components. . . . | 53 |
| 3.6 | Photograph of JEOL 2100 LaB TEM used in this work, (inset) schematic of lacey carbon film on 300 mesh copper grid used for the imaging of MNPs. | 55 |
| 3.7 | Simplified schematic of an ICP-MS to understand its working principle. | 56 |
| 3.8 | Schematic of the measurement of fluorescence in a right angle geometry | 57 |
| 3.9 | Photograph of a) samples for measuring PLQY and b) the equipment. | 58 |
| 3.10 | Transmission spectra of silicone and PMMA films. | 60 |
| 3.11 | Schematic of the edge emission setup used to characterize LSC/PLSC waveguides, main components include the light source, integrating sphere, XY translation stage and a spectrometer. | 62 |
| 3.12 | Photograph of a) wavelength selective filters, b) halogen light source, c) sample holder for characterizing solid samples. | 63 |
| 3.13 | a) AM1.5 G spectrum from the Abet solar simulator, b) Photograph of the solar simulator used in this work. | 64 |
| 3.14 | Circuit diagram of the outdoor setup to measure the current, voltage and temperature from different devices. | 64 |
| 3.15 | Photograph of the K type thermocouple grade wire used in this work, a connector was used to check that the thermocouple was reading the accurate temperature, b) Photograph of the data logger used in this work showing the slots where the multiplexer cards are inserted. . . | 65 |

| | | |
|------|---|----|
| 3.16 | Photograph of the roof with focus on the main components and their relative position such as pyranometers, data logger and the device box. | 66 |
| 4.1 | UV-VIS spectra of CTAB capped Au seeds. | 71 |
| 4.2 | a) UV-VIS spectra of two CTAB capped Au NR samples with different aspect ratios, b) Position of the longitudinal plasmon band peak with change in silver to gold ratio in the growth solution. | 72 |
| 4.3 | a) UV-VIS spectra of five CTAC capped Au@Ag NC samples with different silver shell thickness, b) Photograph of as-synthesized Au@Ag NC samples. | 73 |
| 4.4 | UV-VIS spectra of a) Au NRs sample 1 after synthesis and after 24 hours, b) Au@Ag NCs sample 5 immediately after taking out of oven and after 24 hours. | 76 |
| 4.5 | UV-VIS spectra of a) Au NRs sample 1, b) Au NRs sample 2 before and after centrifugation. | 77 |
| 4.6 | UV-VIS spectra of centrifuged Au NRs, indicating the presence of nanospheres in the pellet solution. | 78 |
| 4.7 | UV-VIS spectra of Au@Ag NC samples 5(a), 4(b), 3(c), 2(d) before and after centrifugation. | 79 |
| 4.8 | a),b) SEM images of Au NRs sample 1 and 2 respectively, c),d) TEM images of Au NR samples 1 and 2 respectively giving an insight about the shape of the NRs, d),e) Size distribution of Au NR samples 1 and 2 respectively. | 81 |
| 4.9 | a) SEM image of as-synthesized Au@Ag NCs, b) TEM image of purified Au@Ag NCs showing the Ag shell thickness, c) Size distribution of Au@Ag NCs, d) Shape analysis by aspect ratio distribution of Au@Ag NCs. | 82 |
| 4.10 | Average dimensions of Au NR and Au@Ag NCs based on electron microscopy, used to determine the concentration and surface area of the MNPs. | 84 |

| | |
|--|-----|
| 4.11 Drawing of a Au NR capped by CTAB, CTAB forms a bilayer on the nanorod and consists of a positive bromide headgroup and hydrophobic carbon tail. | 86 |
| 4.12 UV-VIS spectra of a) Au NRs and b) Au@Ag NCs before and after PEGylation depicting the blue shift in the PEGylated MNPs. | 88 |
| 4.13 Phase transfer of the Au NRs after addition of 3 ml of methanol, the transfer process from right to left. | 89 |
| 4.14 Photograph and UV-VIS spectra of a) Au NRs sample 1 and Au@Ag NCs sample 5 before and after phase transfer | 90 |
| 4.15 UV-VIS spectra of Au NRs coated with PEG in water and Au NRs in the aqueous upper layer after phase transfer. | 91 |
| 4.16 UV-VIS spectra of Au NRs and Au@Ag NCs in DCM and Silicone polymer. | 92 |
| 4.17 Extinction spectra of a) Au@Ag NCs taken after six months, b) Au NRs after one year of dispersion in polymer. | 93 |
| 5.1 Normalized absorption and emission spectra of a) Red dye and b) QD used in this work. | 97 |
| 5.2 Photograph and absorption spectra of a blank Silicone polymer and LSC waveguides with 10-100 ppm Red305 doping concentration. . . | 100 |
| 5.3 a) Total emission spectra of LSC waveguides measured using an integrating sphere, b) Position of the emission peak on varying the doping concentration. | 101 |
| 5.4 Variation of total integrated emission from LSC waveguides with Red305 doping concentration, the polynomial fit is by a five degree polynomial equation. | 102 |
| 5.5 a) Edge emission intensity for various Red305 doping concentrations (10-160 ppm), b) Variation of the emission peak position on increasing the Red305 doping concentration in the waveguide. | 104 |

| | | |
|------|--|-----|
| 5.6 | Integrated edge emission of LSC waveguide with variation in Red305 dye concentration. | 104 |
| 5.7 | Photograph of the outdoor setup consisting of different LSC devices, blank reference and PV cell in vertical position. | 105 |
| 5.8 | a) Average solar radiation throughout the day on 22 August 2018, b) Average power output from the LSC devices, blank reference and the stand alone PV cell throughout the day. | 106 |
| 5.9 | a) Average temperature of the PV cell attached to different LSC waveguides under different radiation intensity, b) Relative power conversion efficiency of the LSC devices on increasing the radiation intensity | 107 |
| 5.10 | a) Total reflectance of diffuse reflector with increasing concentration of TiO ₂ nanoparticles in Silicone, b) Scattering reflectance of the fabricated diffuse reflectors | 109 |
| 5.11 | a) Aggregation of TiO ₂ nanoparticles in the polymer at high concentrations. b) 1cm beam spot on the LSC waveguide with a diffuse back reflector. | 110 |
| 5.12 | Edge emission spectra with and without back reflectors from LSC waveguides with doping concentration of a) 30 ppm and b) 70 ppm. | 110 |
| 5.13 | Integrated edge emission of the LSC waveguides with and without diffuse back reflector. | 111 |
| 6.1 | Normalized a) absorption and extinction spectra spectra of Au@Ag NCs and Red305 dye, b) emission and extinction spectra of Red305 dye and Au@Ag NCs showing the overlap between the respective spectra. | 117 |
| 6.2 | a) Absorption spectra of PLSC waveguides with increasing concentration of Au@Ag NCs, b) Photograph of a PLSC waveguide containing 0.6 ppm Au@Ag NCs concentration. | 118 |

6.3 a) Edge emission spectra of PLSC layers with increasing Au@Ag NCs concentration taken using an integrating sphere. (b) Fluorescence enhancement in PLSC layers as a function of NC concentration normalized to the 0ppm sample 119

6.4 a) Current generated from PLSC device as a function of voltage relative to a blank reference and simple LSC device with Si solar cell attached to the edge, b) The power curve of the PLSC device as a function of voltage and depicting the maximum power for each sample. 122

6.5 Photograph of the outdoor setup consisting of PLSC and LSC devices. 123

6.6 Solar irradiance and average power output from sunrise to sunset. . 124

6.7 a) Ratio of power conversion efficiency of PLSC device to the bare PV cell on 3rd July 2019. The time has been divided into three regions based on the sun’s altitude in the sky. and b) Power conversion efficiency of PLSC and PV cell with respect to irradiation intensity on 30th June 2019. 126

6.8 Normalized power conversion efficiency variation of PLSC device and bare PV cell 127

6.9 a) Solar radiation on 14th August 2019 with cloud cover rated 7-8 oktas with intermittent rain. b) Average power output of LSC and PLSC devices with reflector from sunrise to sunset. 128

6.10 a), c) Daily average of solar irradiance for the months of July and December, respectively. b), d) Average power output of the PV cell and PLSC device for July and December, respectively. 130

7.1 a) Stem component with different coloured PLSC devices. b) Periodic structure containing the Stem components, thus, forming a BIPV component. c) Future application of PLSC devices in the facade of the building. 138

| | | |
|-----|---|-----|
| A.1 | UV-VIS spectra of a) Seed A and b) Seed B taken after every half an hour. | 142 |
| A.2 | UV-VIS spectra of the seed solutions with 700, 900, 1100, 1300 rpm for seeds 1-4 respectively. | 143 |
| A.3 | UV-VIS spectra of Ag NRs samples 1-5 in DI water containing 0.05 ml, 0.1 ml, 0.15 ml, 0.35 ml and 0.4 ml seed solution in the growth solution respectively. | 144 |
| A.4 | UV-VIS spectra of a)Ag NRs sample 4 and b)Ag NRs sample 1 taken before and after centrifugation by re-dispersing the pellet in DI water | 146 |
| A.5 | SEM image of Ag NRs sample 1 after purification, the presence of nanotriangles in the solution is evident and they have approximately the same size as the spheres. | 147 |
| B.1 | Photograph and UV/VIS spectra of a) Au NSs sample 2 1 and b) Au NS sample 2. | 150 |
| B.2 | SEM image and size analysis of a) Au NSs sample A and b) Au NSs sample B. | 151 |
| C.1 | UV-VIS spectra of Yellow083 dye in Silicone polymer having a) 1.1 ppm-2.3 ppm concentration, b) 10 ppm to 55 ppm concentration. | 154 |
| C.2 | Total emission spectra of 10 ppm and 30 ppm Yellow083 dye in Silicone polymer. | 156 |

List of Tables

| | | |
|-----|--|-----|
| 2.1 | State of the art LSC upto 2018 using different configurations and advanced fluorophores | 22 |
| 3.1 | Summary of the chemicals, host matrix, fluorophores and their properties used in this study. | 47 |
| 4.1 | Number of Au NRs and Au@Ag NCs in a given volume. | 85 |
| 5.1 | Measured Red305 dye concentrations for Silicone samples. | 98 |
| 5.2 | Different samples concentrations, their excitation wavelengths and measured PLQY. | 99 |
| B.1 | Number of Au NSs in a given volume. | 150 |
| C.1 | Measured Yellow083 dye concentrations for Silicone samples | 155 |

Chapter 1

Introduction

MODERN society is based on the ability of humankind to convert primary energy (coal, crude oil, sunlight) to secondary energy (electricity, gasoline, diesel). According to BP's energy outlook, global energy demand is expected to increase by a third by 2040 (Outlook, 2012). Virtually all of the growth in energy demand is from fast-developing countries like China and India (IEA, 2018a). Basic market mechanism states that more demand for a product that is not balanced by an increase in supply results in a more expensive product. As of 2016, energy infrastructure worldwide heavily depends on fossil fuels (IEA, 2016) as shown in Figure 1.1.

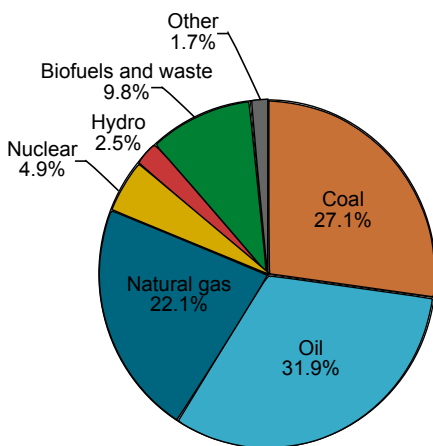


Figure 1.1: World's total primary energy supply by fuel in 2016 (IEA, 2016)

There are many challenges associated with the use of fossil fuels. They are not a sustainable form of energy source; their rate of depletion by humans is faster as compared to their generation by photosynthetic processes. Another problem is that burning of fossil fuels which are essentially hydrocarbons increases the concentration of atmospheric carbon dioxide (CO₂). According to the International Panel on climate change, fifth assessment report, CO₂

emissions have increased by 40% since pre-industrial times (*IPCC 2015*). From the report: "Human activities are estimated to have caused approximately 1.0ÅřC of global warming above pre-industrial levels". To limit the temperature increase to 1.5°C will require zero-carbon emissions from 2030 to 2050 (*IPCC 2015*).

Solar energy has the potential to achieve this goal. New technology framework and strategies are required from industrialized countries to utilize the energy provided by the sun directly to deal with the energy crisis. Renewable energy was the second largest contributor to global electricity production in 2016. Renewables accounted for 23.8% of world electricity generation, after coal (39.2%) and gas (23.6%) (*IEA Atlas of energy 2016*). In OECD (Organisation for Economic Cooperation and Development) countries the total primary energy supply from renewables has increased from 272 Mtoe to 539 Mtoe between 1990 to 2017 (IEA, *2018b*). In 2017, solar photovoltaic (PV) electricity produced in OECD countries amounted to 9.8% of its total renewable electricity production. With an annual growth rate of 34.8% from 1990 to 2017 solar PV is the fastest growing renewable electricity technologies (IEA, *2018b*). The evolution of world total solar photovoltaic installed capacity from 2000 to 2018 can be seen in Figure 1.2. China is the top producer of solar PV electricity and net installed capacity with 22.9% and 25.8% share in world total respectively. At present, it is more expensive to generate electricity from solar energy than from fossil fuels. The future of large scale PV deployment is based on three things 1) cost reduction 2) high power conversion efficiencies and 3) low material usage (MIT, *2015*). It is important to know the current PV technologies to develop strategies for long term reductions in the cost of solar electricity.

1.1 Photovoltaic Technologies

Historically PV technologies can be divided into three distinct generations based on module efficiency and area cost, as shown in Figure 1.3:

First-generation technology consists of wafer-based solar cells of crystalline silicon (c-Si) and gallium arsenide (GaAs). c-Si constitute ~90% of global production

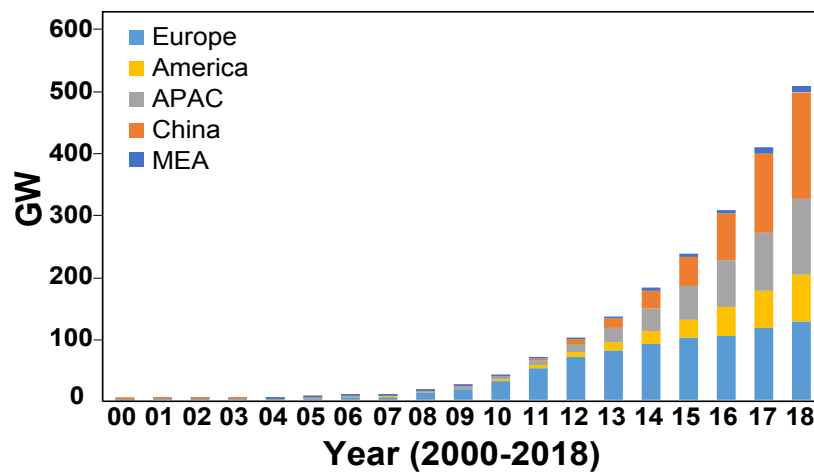


Figure 1.2: Global total solar PV installed capacity. Data taken from (*GlobalMarketOutlook 2018*).

capacity and are the most mature PV technology (Group, 2014). They can be further classified as single crystalline or multi-crystalline with the latter having ~62% market share in 2017 (ISE, 2019). A key fundamental limitation of c-Si is its indirect bandgap, that leads to weak absorption of light and requires wafers with thicknesses on the order of 100 microns in the absence of advanced light-trapping strategies. High material costs limit large scale deployment of current GaAs solar cells.

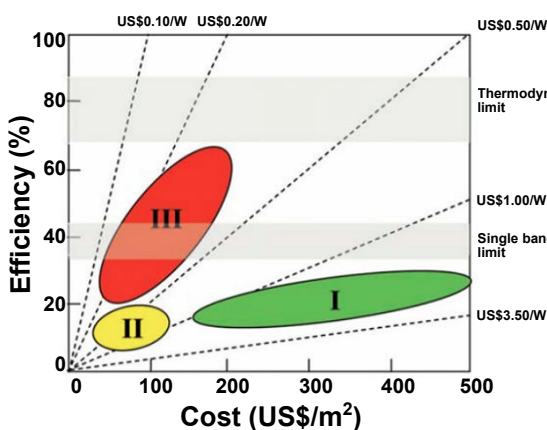


Figure 1.3: Efficiency and cost projections of (I), (II) and (III) generation PV technologies (Conibeer, 2007)

Second-generation technology consists of thin film-based solar cells such as hydrogenated amorphous silicon (aSi:H), cadmium telluride (CdTe) and copper indium gallium diselenide (CIGS). aSi:H has a stronger absorption than c-Si, it has a larger bandgap compared to c-Si (1.12 eV) that reduces the range of absorbed energy (Shah et al., 2004). Amorphous Si held a global market share of 2% in 2013 but their

susceptibility to light-induced degradation and low efficiency compared to other mature thin-film technologies limits their market adoption. CdTe is the leading thin-film technology due to the lowest module costs with a global market share of 5% in 2013. The toxicity of elemental Cadmium (Fthenakis and Zweibel, 2003) and the scarcity of Tellurium has motivated research on different materials. CIGS is a compound semiconductor with a direct bandgap of 1.1 eV and held a global PV market share of 2% in 2013. The key technical challenges with it are the high variability in film stoichiometry and properties, low open-circuit voltage due to structural inhomogeneity (Werner, Mattheis, and Rau, 2005), scarcity of Indium can inhibit large scale adaptation of these modules.

Third-generation technology includes a non-exhaustive list of novel thin-film devices, dye-sensitized solar cells (DSSC), Quantum dot (QD) solar cells, organic solar cells, hot carrier cells, perovskite solar cells, thermo-photovoltaics, and concentrated PV, up and down-conversion. Multi-junction solar cells hold the world record on solar cell performance. The third generation aims to combine the low cost of the second generation and high efficiencies of the first generation. Advancements in cell efficiencies from 1975 to 2018 can be seen in Figure 1.4 (*NREL Cell Efficiency chart 2018*). Even though the most commonly used classification the generation scheme fails to incorporate the upcoming modern PV technology. The technical demands of on-grid and off-grid PV applications have lead research towards the development of alternate PV technologies. This next-gen technology should comprise devices that can offer ultra-high efficiency, unique form factors, and unique aesthetics. Concentration photovoltaics (CPV) is an emerging technology that represents 1% of the global annual market (Mokri and Emziane, 2011). The key principle of CPV is the use of cost-efficient concentrating optics that dramatically reduce the cell area and potentially a leveled cost of electricity (LCOE).

Luminescent solar concentrators (LSCs) fall under the category of low concentration photovoltaics (less than 10). LSCs offer an alternative, inexpensive and non-tracking approach to enhance the PV power output. These semi-transparent

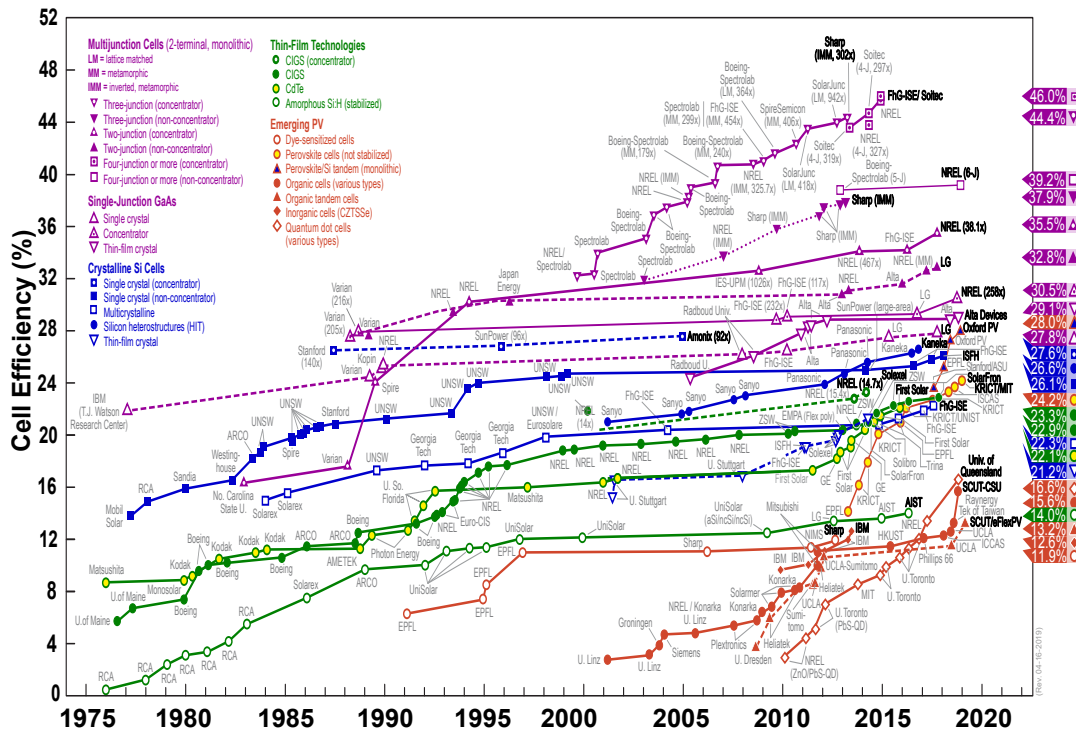


Figure 1.4: Different technologies existing with the first generation (blue), second-generation (green) and rest of them belong to third-generation PV. Multi-junction cells have a high radiation resistance, low-temperature sensitivity and better efficiency than c-Si cells, however, they are very expensive.

PV glazing systems can be integrated into the buildings invisibly without negatively impacting the buildings aesthetic (Meinardi, Bruni, and Brovelli, 2017). The shape, transparency, and flexibility of the LSCs can be controlled. Both diffuse and direct solar radiation can be utilized by an LSC device. Various energy loss mechanisms due to non-unity photoluminescent quantum yield (PLQY) of the fluorophore, inefficient trapping efficiency, self-absorption losses and transport losses in the LSC prevent their large scale use.

A new approach to enhance the light emission from the edge of the LSC device has been proposed to tackle the losses in these devices. Plasmonic Luminescent Solar Concentrator (PLSC) utilizes the plasmonic coupling between a metal nanoparticle (MNP) and fluorophore to enhance the power output from the edge of an LSC. Plasmonic interaction can alter the optical properties of the fluorophores, fluorescence lifetime and quantum yield. Plasmonic interaction depends on many

factors such as the plasmonic frequency of the MNPs, spectral overlap between the MNPs plasmon band and the absorption/emission bands of fluorophores, spacing between the MNPs and fluorophores. Therefore, it is important to understand these effects in a macroscopic level and to optimize the MNPs for application in PLSC.

1.2 Research Objectives

The main aim of this Ph.D. thesis is to understand and optimize the role of MNPs led plasmonic interaction in a PLSC device and the effect of MNP concentration to the power conversion efficiency of the device.

It is important to be able to tune the plasmonic band of the MNPs depending on the fluorophore used in the PLSC device. The first objective is to synthesize various MNPs and have a control over their SPR wavelength.

The MNPs should retain their optical properties while doped in in the PLSC device. Thus, the second objective is to establish a reproducible protocol starting from the synthesis of the MNPs to their incorporation in the host polymer matrix.

The enhancement in the edge emission of the device is dependent on the extent of plasmonic coupling between the MNP and fluorophore. The third objective is to assess the role of the doping concentration of the MNPs, the spectral overlap between MNP's plasmon bands and fluorophore's absorption and emission spectra on the power conversion efficiency of the PLSC device.

The final objective is to test the optimized PLSC device in outdoor conditions in Ireland.

1.3 Thesis roadmap

The thesis is structured into seven chapters.

Chapter 2 sets the foundation for the objectives. It consists of an up to date literature review on LSCs. The recent advances in LSCs concerning materials and device fabrication are stated. The various energy loss mechanisms in an LSC are

discussed in detail. The goal of this Ph.D. is to combine the field of plasmonics with LSC devices by targeting the re-absorption, escape cone losses and increase the edge emission of the device. Therefore, understanding the theory of surface plasmonics in MNPs especially gold (Au), silver (Ag) and the parameters that affect the surface plasmon bands of MNPs is crucial for this study. The effect of placing an MNP in the vicinity of a fluorophore is reviewed. In this work, anisotropic MNPs were used in the PLSC devices to have better control over the tuning of the plasmon bands. The latter part of this chapter focuses on the synthesis processes of anisotropic Au and Ag MNPs, dwelling on the recipes that were used in this work.

Chapter 3 lists all the materials used in the synthesis, functionalization and phase transfer of MNPs in this work. The experimental techniques for the optical characterization of the MNPs and LSC/PLSC waveguides and the IV characteristics of the final devices are discussed. The electron microscopy techniques to know the shape and size of MNPs and the instrument to determine the concentration of MNPs in solution are reviewed. The methodology adopted to fabricate LSC/PLSC waveguides and diffuse reflectors are stated.

Chapter 4 focuses on fabricating nanocomposites designed specifically for plasmonic LSC application. Gold nanorods and gold core silver shell nanocuboids of various sizes were synthesized and a narrow size and shape distribution was achieved by purification via centrifugation. Synthesis of MNPs was carried out in aqueous solution to achieve better control over the size and shape of the MNPs, therefore, the focus is to transfer the synthesized MNPs into an organic solvent that is compatible with Silicone encapsulant polymer (host matrix) LSC/PLSC. The results on surface functionalization of anisotropic MNPs and their stability in organic solvent dichloromethane is discussed. Experimental results on quantification of gold nanospheres, nanorods and gold core silver shell nanocuboids are provided.

Chapter 5 The compatibility of fluorophores in Silicone polymer is tested. The fabrication process of LSC is discussed with a varying doping concentration of fluorophore (Red305 dye). It focuses on the optimization of Red305 dye doping con-

centration on LSC. Crystalline silicon solar cells have been used and the devices have been tested outside using a setup to test multiple devices relative power output simultaneously.

Chapter 6 Gold core silver shell nanocuboids have been used with Red305 dye to fabricate PLSCs. Through these characterizations, the effect of MNP doping concentration and spectral overlap between MNP and fluorophore is discussed on the enhancement of edge emission from the PLSC waveguide. PLSC device is compared to an LSC device and bare PV cell outdoors in different lighting conditions. The feasibility of a PLSC device is therefore tested as a viable option to overcome some of the losses incurred by an LSC device.

Chapter 7 comprises of the summary of all results with the contribution to knowledge. Recommendations for future work based on this Ph.D. work is discussed.

Chapter 2

Literature Review

LCSs have an advantage over conventional high concentrating photovoltaics but they face various energy loss mechanisms that inhibit their realization in large scale. This chapter focuses on the operating principle of an LSC and the various energy loss mechanisms in the device. Recent advances in the materials used in LSC and the device configurations are discussed. PLSCs are the upcoming advanced technology in LSCs which is the motivation for this work. The latter part of the chapter is a brief theory on surface plasmonic resonance in metal nanoparticles (MNPs). A brief review on fluorescence modulation in the presence of MNPs is discussed. The focus then shifts to the synthesis processes of gold (Au) and silver (Ag) MNPs and the factors that can influence the shape, size, and stability of the MNPs. The findings of the review pave the way for the fabrication of MNPs especially catered for application in luminescent devices and the fabrication and optimization of PLSC.

2.1 Operating parameters of a photovoltaic cell

A PV cell directly converts solar energy to electricity. There are three basic steps required: 1) Photon absorption for electron-hole pair generation, 2) charge carrier separation, 3) charge carrier collection. These operating steps can be quantified by the efficiency (η_{PV}) of the cell. It is defined as the ratio between the maximum

operating power and the total power.

$$\eta_{PV} = \frac{P_{max}}{P_{tot}} = \frac{V_{max} \times I_{max}}{P_{tot}} = \frac{V_{oc} \times I_{sc} \times FF}{P_{tot}} \quad (2.1)$$

where V_{oc} is the open circuit voltage, I_{sc} is the short circuit current and FF is the fill factor. Graphically, FF is a measure of the area of the largest rectangle that will fit in the IV curve as illustrated in Figure 2.1. A solar cell with a higher voltage has a larger possible FF since the "rounded" portion of the IV curve takes up less area. The main loss processes in a single junction solar cell are described in Figure

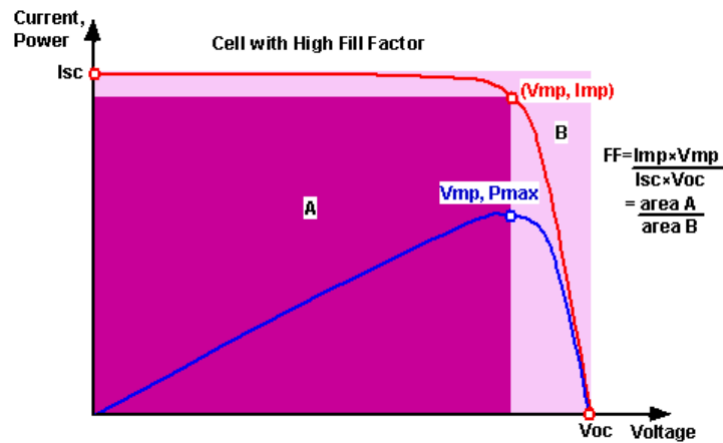


Figure 2.1: Graph of cell output current (red line) and power (blue line) as a function of voltage.

2.2. Photons excite the electrons from the valence band to the conduction band across the forbidden energy gap, which is known as bandgap. The excited electron-hole pair quickly loses the energy it has above the bandgap energy, this has been depicted as process 1 in Figure 2.2. This means that a low energy photon will have the same outcome as a high energy photon thus limiting the conversion efficiency of the cell to 44% (Green, 2001).

Loss due to the recombination of the excited electron-hole pairs has been depicted as process 2 in Figure 2.2. This loss can be limited by using semiconductor materials with a high lifetime of carriers which is directly determined by radiative recombination processes in the cell.

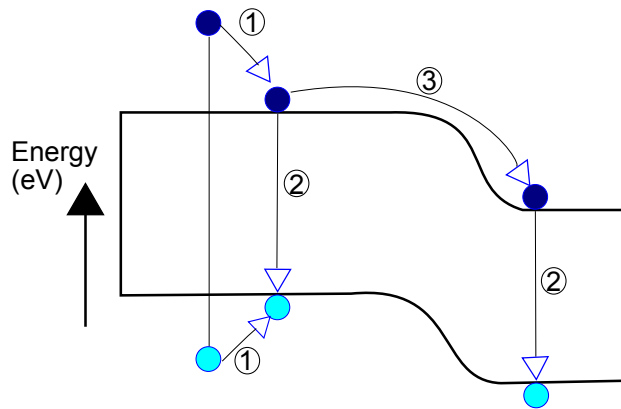


Figure 2.2: Loss processes in a standard solar cell: (1) thermalization losses, (2) recombination losses, (3) junction losses.

In 1960 Shockley and Queisser (Shockley and Queisser, 1961) used this symmetry between light absorption and light emission to derive the fundamental limit on solar cell performance.

A PV cell working under concentration will experience a higher short-circuit current and receive a higher total power. These two terms vary linearly with the concentration factor. Consequently, the gain in I_{sc} is not directly responsible for efficiency gain because it cancels out with the total power (Proise, 2014). The benefit of concentration on cell efficiency is mainly due to V_{oc} . PV cell output can be increased without improving the efficiency of cells by multiplying the solar radiation intensity on the solar cell junction using concentration photovoltaics.

2.2 Concentration Photovoltaics

CPV technologies comprise optical devices that focus light onto a smaller area of PV. There are two main ideas behind CPV: 1) reduces the material costs where expensive PV material is replaced by more affordable mirrors/lenses; 2) the open-circuit voltage varies logarithmically with the concentration factor (Proise, 2014), therefore, contributing in improvement of the efficiency (Luque and Hegedus, 2003). Even though the short circuit current is linearly dependent on the light intensity, this effect does not provide an increase in efficiency because the incident power also increases linearly with concentration. The optical concentration factor can be

written as:

$$C = C_{geo} \times \eta_{opt} \quad (2.2)$$

C_{geo} is the geometric concentration factor η_{opt} is the optical efficiency. Since the position of the sun is not the same in the sky and it is dependent on the time of the day and season. Therefore, the CPV is designed to consider this incidence angle variation to be efficient throughout the year. This is taken into consideration by defining an acceptance angle θ_{acc} , which is the maximum angle at which incident light can be concentrated by CPV. The maximum optical concentration achievable is (Smestad et al., 1990):

$$C_{max} = \frac{n^2}{\sin^2 \theta_{acc}} \quad (2.3)$$

where n is the refractive index of the medium in which the concentrator is placed.

The lower the acceptance angle, the higher the concentration factor. However, concentrating optics alignment is more challenging for such a configuration. Sunlight can be either direct or diffuse. Diffuse sunlight is scattered from the direct solar beam by molecules present in the atmosphere. Unfortunately, direct and diffuse radiation are not concentrated with the same efficiency in high CPV. Diffuse light has an acceptance angle of 90° , whereas direct radiation exhibits only one incidence angle depending on the sun position. If for a concentration system θ_{acc} is not 90° , then it cannot concentrate diffuse solar radiation. Waveguides used in this work are $4.5 \times 4.5 \times 0.3 \text{ cm}^3$ in size and the area of the PV cells used is $0.3 \times 5 \text{ cm}^2$. An LSC cannot exceed the theoretical SQ limit of the cell.

As seen in Figure 2.3 throughout a year, diffuse solar radiation reaches 65.0 % of the global irradiance in Dublin. In sunny places, more than 1/3 of light can be diffuse, whereas, in cloudy places, this proportion can exceed 50%. In places similar to Dublin, the use of concentration systems which are not able to concentrate diffuse light means to lose straight away more than half of the radiation. Concen-

tration systems with concentration factor below 10 belong to low CPV. They do not require sun tracking systems and heat dissipation systems, consequently making LCPV inexpensive. They are compatible with cheap and highly efficient wafer-based solar cells. Therefore, LCPV can be a way to increase the efficiency of the PV module with a soft extra cost. LSC fall under this category.

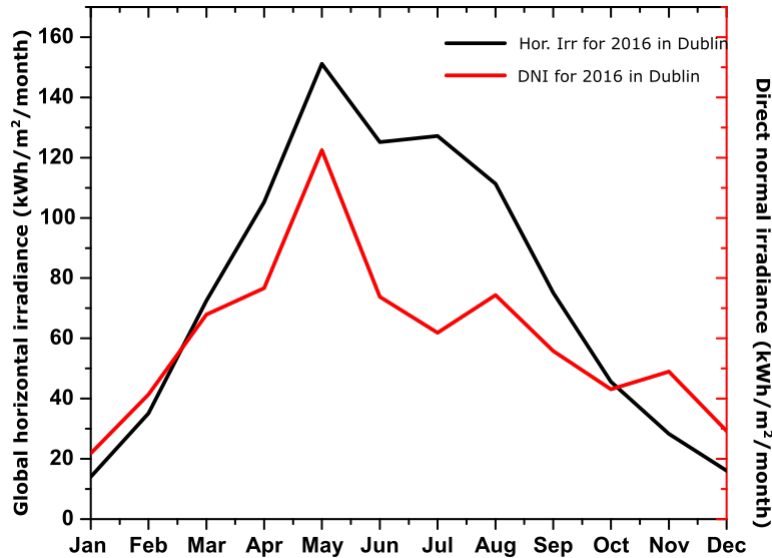


Figure 2.3: Direct normal irradiation and global horizontal irradiation for Dublin in 2016. Data available in (*SolarEuropa PVGIS*).

2.3 Overview of Luminescent Solar Concentrator

Weber et al. first proposed this idea in 1976 to reduce the amount of silicon used in photovoltaic modules and to lower the cost of harvesting solar radiation (Weber and Lambe, 1976).

As mentioned in the introduction chapter LSC aims to reduce the cost of solar electricity production by using an inexpensive collector without mechanical tracking (Weber and Lambe, 1976, Goetzberger and Greube, 1977, Reisfeld and Jørgensen, 1982). LSC is a conceptually simple structure illustrated in Figure 2.4. A typical LSC consists of a transparent plate with a refractive index larger than 1 in which highly fluorescent molecules such as (Quantum dots, organic dyes, and

rare earth complexes) are embedded.

Light is incident on the top surface of this inexpensive polymer or glass waveguide. The incident light is absorbed and re-emitted at a longer wavelength. Photons that are emitted at an angle below the critical angle are trapped in the waveguide via total internal reflection and are transported to the edge. PV cells are attached to the

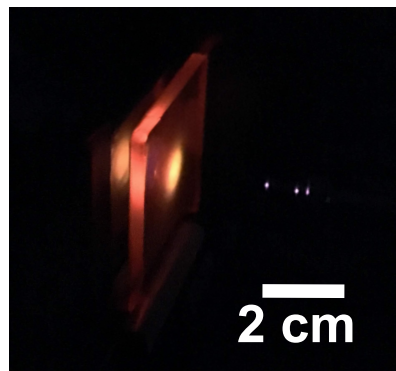


Figure 2.4: Red-dye LSC illuminated in the center by a light source.

edge of the waveguide to absorb the photons and convert them into electricity.

LSCs have the following advantages over conventional geometric concentrators:

- Isotropic absorption of dyes embedded in the waveguide ensures that LSC can concentrate both diffuse and direct sunlight. Consequently, LSC does not need to track the sun and this reduces the complexity and cost of the system.
- LSCs can be aesthetically pleasing, they can be employed in building integrated photovoltaics as windows because their transparency can be tuned and the PV cells can be embedded in the window frame. A possible application of LSC can be seen in Figure 2.5.
- The PV cells bandgap can be tuned to the emission of the fluorophore thus reducing energy dissipation as heat. Therefore, the PV cells do not require a cooling system as they operate at a lower temperature.
- The fabrication of LSC waveguide is compatible with low-cost manufacturing such as molding and casting. LSC does not require the use of scarce materials such as Indium or Gallium.
- LSCs can be placed next to each other without the risk of shadowing their neighbor from the sun.

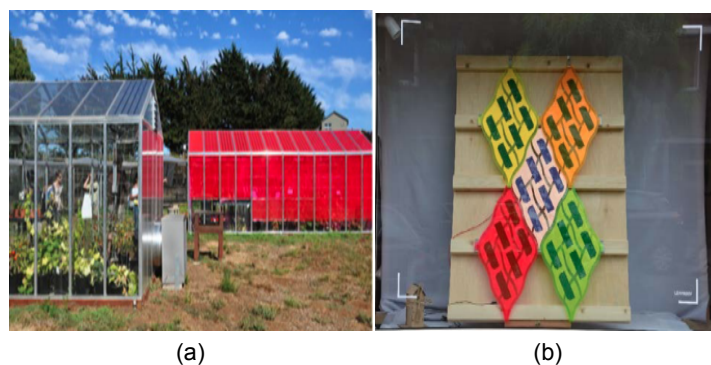


Figure 2.5: a) LSC based greenhouse (Corrado et al., 2016), b) LSC based roof tiles 'Leaf Roof' (Reinders et al., 2016).

2.3.1 Fluorophores

For LSC application an ideal fluorophore should have near-unity PLQY, a wide absorption band, high absorption coefficient, high Stokes' shift and low cost (Van Sark et al., 2008, Moraitis, Schropp, and Sark, 2018). A brief description of the three categories of fluorophores (organic dyes, quantum dots, and rare earth complex) employed in an LSC is given below:

Organic dyes: The Jablonski diagram of an organic dye can be seen in Figure 2.6a. An electron from the ground state (S_0) is excited to the first excited electronic state (S_1). It then decays non-radiatively by internal conversion to the lowest vibrational level of (S_1). From there, it decays to (S_0) by the emission of a fluorescence photon. Transitions between the different vibrational levels of the molecule give rise to peaks in the absorption and emission spectra as seen in Figure 2.6b. Organic dyes are the most commonly used fluorophore in LSC as they can be easily dissolved into polymers. Many visible emitting dyes have near-unity PLQY (Batchelder, Zewail, and Cole, 1981, Wilson and Richards, 2009). However, all organic dyes exhibit an overlap of absorption and emission spectra and therefore, result in re-absorption losses in an LSC device. As stated previously, a broad absorption range ideally all wavelengths below 950 nm is necessary to maximize LSC performance. Most organic dyes have an absorption bandwidth of less than 200 nm.

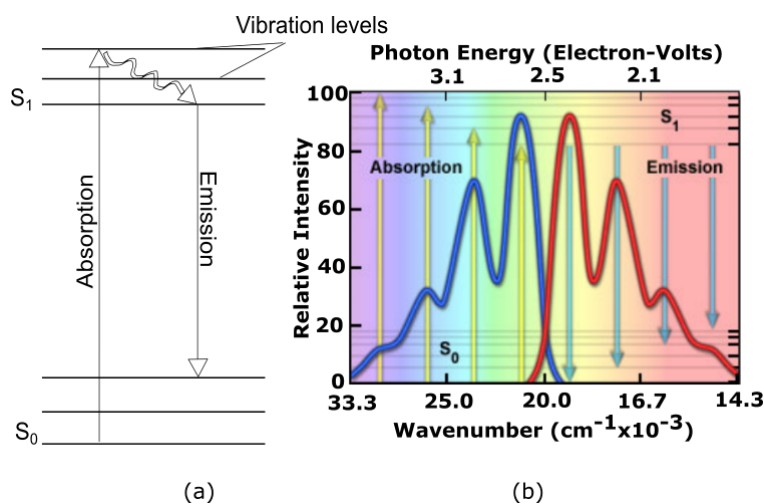


Figure 2.6: a) Jablonski energy level diagram of an organic dye, b) Hypothetical electronic absorption and emission bands showing transition from ground state to lowest excited energy state.

Quantum dots: Inorganic compounds such as PbS, PbSe have broad absorption spectra, high absorption coefficient and the emission peak can be tuned by changing the diameter (H. Sargent, 2005). High PLQY QDs have been synthesized in the laboratory (Coropceanu and Bawendi, 2014), but commercial QDs have PLQY less than 50% and are more expensive than organic dyes (Resch-Genger et al., 2008). Despite the broad absorption spectra, there is a significant overlap between the absorption and emission spectra of the QDs. In combination with the low PLQY, this overlap results in huge re-absorption losses in the LSC device. The overlap in the absorption and emission spectra is due to the distribution of different diameter of QDs in a sample (Micic et al., 1994). Therefore, improvements in QD production techniques can lead to narrow distribution and lower the re-absorption losses from QD samples (Sholin, Olson, and Carter, 2007). Core-shell QDs improve the surface passivation of the QD by having a shell of a wider bandgap semiconductor (Mello Donegá, 2011).

Rare earth complex: Lanthanide ions such as Nd^{3+} and Yb^{3+} have a large Stokes' shift, high PLQY and excellent photostability, making them highly suitable for use in LSCs (Reisfeld and Kalisky, 1981, Friedman, 1981). In a combination of

two ions, one ion is the sensitizer it absorbs light and transfers the energy to the second ion known as the activator that emits light in the near-infrared (NIR) region. For example a combination of Neodymium (Nd³⁺) with Ytterbium (Yb³⁺) where Nd³⁺ acts as the sensitizer and Yb³⁺ is the activator which emits at 970 nm (Reisfeld and Kalisky, 1981). However, even with high energy transfer efficiencies, the process is limited by low absorption efficiencies (Parent et al., 1986). Despite promising features of rare earth materials they have low thermal and photochemical stability.

2.4 Operating Parameters of LSC

LSC efficiency can be defined by parameters such as geometric gain, solar concentration ratio, and optical efficiency. It is important to understand each parameter independently to determine the operation of the LSC device. Geometric gain is the ratio of the top surface area $A_{surface}$ of the waveguide to the area of the edge A_{edge} where PV cell is attached. It is obtained by:

$$G_g = \frac{A_{surface}}{A_{edge}} \quad (2.4)$$

As the physics underlying LSCs differs from the conventional geometric concentrators it is important to estimate the maximum concentration achievable for an LSC. Yablonovitch imposed the second law of thermodynamics on an LSC consisting of a dye absorbing photons at energy ϵ_1 to emitting photons with energy ϵ_2 (Smestad et al., 1990, Yablonovitch, 1980):

$$C_{max,LSC} = \frac{\epsilon_2^3}{\epsilon_1^3} \exp \frac{\epsilon_1 - \epsilon_2}{kT} \quad (2.5)$$

According to equation 2.4, the maximum concentration factor is dependent on the Stokes' shift of the fluorophore used in the LSC. The optical efficiency of an LSC

can be theoretically given by (Goetzberger and Greube, 1977):

$$\eta_{opt} = (1 - R)P_{TIR} \cdot \eta_{abs} \cdot \eta_{PLQY} \cdot \eta_{Stokes} \cdot \eta_{host} \cdot \eta_{TIR} \cdot \eta_{self} \quad (2.6)$$

where R is the reflection of solar radiation from the waveguide surface, P_{TIR} is the total internal reflection efficiency, η_{abs} is the fraction of solar radiation that is absorbed by the dye, η_{PLQY} is the photoluminescent quantum yield of the used luminophore, η_{Stokes} is the energy lost due to the heat generation, η_{host} is the transport efficiency of the waveguided photons through the waveguide, η_{TIR} is the reflection efficiency of the waveguide, η_{self} is the transport efficiency of the wave guided photons related to re-absorption of the emitted photon. Unlike internal optical efficiency, the LSC optical efficiency is dependent on the wavelength, which is a function of the absorption cross-section of the luminophore. The optical efficiency is dependent on many factors as can be seen from the equation and these factors contribute to the energy losses in the LSC. It should be noted that equation 2.3 is an approximation and all the efficiencies are interdependent.

2.5 Energy loss mechanisms in an LSC

The main energy loss mechanisms are discussed below and the schematic of an LSC is shown in Figure 2.7.

External losses: These losses occur before the light enters the waveguide and are independent of other loss mechanisms. The refractive index of air is different from the refractive index of the host material, this gives rise to a reflection coefficient also called the Fresnel reflection coefficient. Fresnel reflection coefficient depends on the light polarization, refractive indices, and incidence angle. Solar radiation is not polarized and assuming the solar radiation is normal with respect to the surface, the reflectance simplifies to:

$$R = \left| \frac{n_{mat} - n}{n_{mat} + n} \right|^2 \quad (2.7)$$

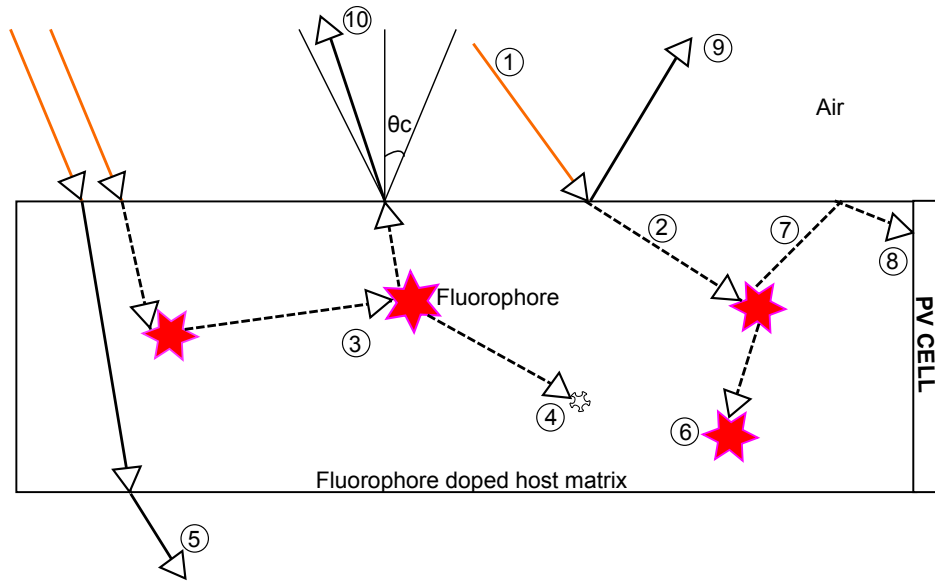


Figure 2.7: Cross-section of an LSC device with PV cell attached to one edge. Incident solar radiation (1), is absorbed by a fluorophore (2), is trapped in the host matrix via TIR (7). Energy loss mechanisms shown are re-absorption losses (3), host matrix absorption (4), un-absorbed solar radiation (5), non-radiative decay due to non-unity PLQY (6), losses due to optical coupling (8), reflection from top surface (9), escape cone losses (10).

For $n_{mat}=1.5$; $R=4\%$

Non-unity photoluminescent quantum yield: PLQY defines the ability to emit a photon after its absorption by a fluorophore, as shown in equation:

$$\eta_{PLQY} = \frac{\text{number of emitted photons}}{\text{number of excited molecules}} \times 100\% \quad (2.8)$$

The effects of non-unity PLQY is multiplied for multiple re-absorption events. If a fluorophore has 80% PLQY the probability of emission of the photon after five re-absorption events are $0.80^5 = 0.33$. Therefore, a high (near-unity) PLQY is a requirement for good LSC performance. The PLQY of different dyes with respect to their emission peak can be seen in Figure 2.8.

Escape cone losses: As mentioned earlier in the chapter, photons are trapped in LSC when light is incident in the internal surface at an angle greater than the critical angle of the LSC. The probability that emitted photon is trapped in the host

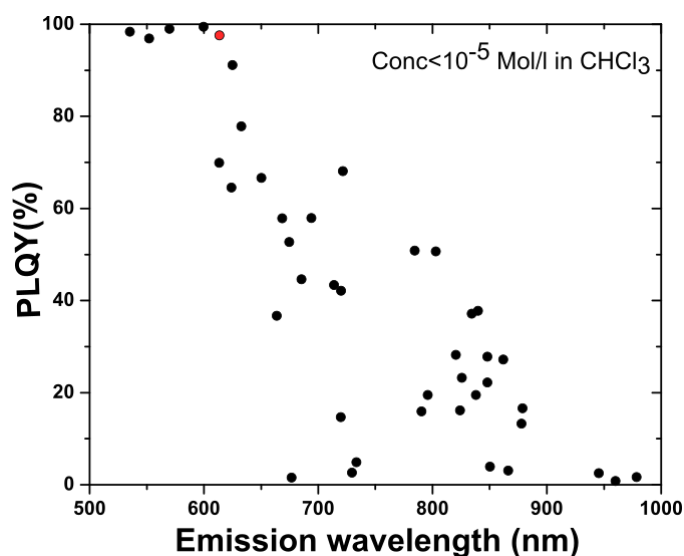


Figure 2.8: PLQY of different dyes vs their emission wavelength. The red data point corresponds to Lumogen Red305 dye. Adapted from (Zastrow, 1994).

matrix is given by:

$$P_{TIR} = \frac{\sqrt{n_{mat}^2 - 1}}{n_{mat}} \quad (2.9)$$

For a host matrix with a refractive index of 1.5, 25% of the re-emitted photons are lost through the front or rear escape cones. In the scenario of multiple re-absorption events, each subsequent re-emitted photon has the probability of 25% to escape from the host matrix (Goetzberger and Greube, 1977). There have been many attempts that have resulted in an increase in efficiency by tackling the escape cone losses as discussed in section 2.3.

Stokes' shift losses: Energy is lost due to the Stokes shift between the absorption and emission peak of the fluorophore ($\epsilon_1 - \epsilon_2$). Even if the fluorophore has 100% PLQY there will always be a net energy loss during fluorescence. A fraction of energy lost during Stokes shift can also be represented as $1 - \eta_{Stokes}$.

Narrow absorption range: Ideally, an LSC should absorb the maximum range of incident solar radiation wavelength with energies higher than the bandgap of the solar cells attached to the edge of the device. Only 26% of the AM 1.5G solar

spectrum falls below 550 nm (Goetzberger and Wittwer, 1981), even if an LSC absorbs all incident wavelength below 550 nm it has $\eta_{abs} = 0.26$. With Si solar cells, LSC should absorb all wavelength below 950 nm for optimum performance and increase η_{abs} .

Re-absorption losses: Re-absorption occurs due to the overlap between the absorption and the emission peak of the fluorophore in the LSC. Although there is subsequent emission after re-absorption it is subjected to the PLQY of the fluorophore and will have a probability to be lost via the escape cones. Photons in an LSC can have multiple re-absorption events and each increases the chance of the photons being lost (Olson, Loring, and Fayer, 1981, Sansregret et al., 1983). The fraction of fluorescent photons reaching the edge greatly depends on the concentration and PLQY of the fluorophore.

Host matrix absorption: Matrix absorption coefficients are wavelength dependent. Many polymers exhibit strong absorption in NIR region. PMMA, a commonly used host matrix in LSC has an absorption coefficient of 10^{-4} to 10^{-3} cm^{-1} . These losses can be neglected for small dimension LSC ($4.5 \times 4.5 \times 0.3 \text{ cm}^3$) as used in the work for this thesis. But, matrix absorption loss may scale with size due to an increase in photon mean free path.

Escape cone losses, re-absorption losses, losses due to narrow absorption range, Stokes' shift losses are the major losses contributing to the low efficiency of LSCs. These must be improved to obtain LSCs with higher efficiencies.

2.6 Recent advances in LSC

Current record efficiencies in LSC are given in Table 2.1. Recent advances to combat the major loss mechanisms mentioned in section 2.2 have been discussed in this section.

Organic dyes are most commonly used in LSC designs (Wilson and Richards, 2009, Reda, 2007, Mulder et al., 2009). Lumogen perylene based dyes have a broad absorption range high PLQY but a small Stokes shift. A new perylene dye with

| Author, year | LSC size (cm ³) | PV cell | η_{LSC} | Comments |
|--------------------------|-----------------------------|-----------|--------------|---|
| Slooff et al., 2008 | 5x5x0.5 | GaAs x 4 | 7.1 | Mixed-dye with backside diffuse reflector |
| Goldschmidt et al., 2009 | (2x2x0.3) x 2 | GaInP x 4 | 6.7 | Mixed dye two sheets |
| Li et al., 2015 | 2.2x2.2x0.3 | c-Si | 8.71 | Quantum dots |
| Zhao et al., 2016 | 7x1.5x0.3 | Si | 1.15 | Giant core-shell QD |
| Wu, Li, and Klimov, 2018 | 15.24x15.24 | GaAs | 3.1 | Tandem based using QDs |
| Mateen et al., 2019 | 2x2x0.3 | p-Si | 2.87 | QD and dye conjugate |

Table 2.1: State of the art LSC upto 2018 using different configurations and advanced fluorophores

high photochemical stability has been synthesized for the use in LSC. The Stokes shift reported for this dye was as high as 300 meV with PLQY of 70% (Sanguineti et al., 2013). Multiple dyes have been used to increase the absorption range of the LSCs (Van Sark et al., 2008, Bailey et al., 2007). In this scenario all the photons are emitted by the dye having the longest wavelength, therefore the overall LSC efficiency depends on the PLQY of this dye. NIR emitting dyes have a low PLQY (Rurack and Spieles, 2011) and can result in a significant decrease in LSC efficiency. Tandem or cascade LSCs (Currie et al., 2008, Debije et al., 2011, have been used to overcome this problem, dyes with lower PLQY are placed below the dyes with a higher PLQY separated by an air gap. Stacked sheets can also result in lower escape cone losses. However, the increase in the efficiency should be balanced by the extra energy and cost involved in fabricating multiple sheets (Ziegler et al., 2014).

Rare earth complexes have high stability, zero self absorption, high PLQY for application in LSC (Moudam et al., 2009, Man et al., 2007, Khan et al., 2010, Wang et al., 2011a, Wang et al., 2011b). However, they have narrow absorption ranges and are much more expensive than dyes. Quantum dots (QDs) were introduced as a competitor to overcome the disadvantages of organic dyes (Meinardi et al., 2017, Bronstein et al., 2015). Initially cadmium and lead based QDs were fabricated to improve the efficiency of the device (Barnham et al., 2000, Shcherbatyuk et al., 2010). Due to the toxic nature and environmental impact of these QDs focus was shifted to semiconductor based (Meinardi et al., 2015) as depicted in Figure 2.9, and Zinc based QDs (Bergren et al., 2018). By changing the size and material of

QDs they can have a broad absorption band (Shcherbatyuk et al., 2010). They have a high PLQY (Coropceanu and Bawendi, 2014, Chen et al., 2013) but improvements are needed to increase their long term photostability (Wu, Li, and Klimov, 2018). Carbon QDs have been synthesized recently (Xu et al., 2004 Wang et al., 2018), they exhibit high stability and find application in large scale LSC windows (Mateen et al., 2019). Giant QDs are specially designed core/shell QDs with relatively thick shell (1.5 nm up to tens of nm) have been engineered to achieve zero re-absorption losses (Zhao et al., 2016).

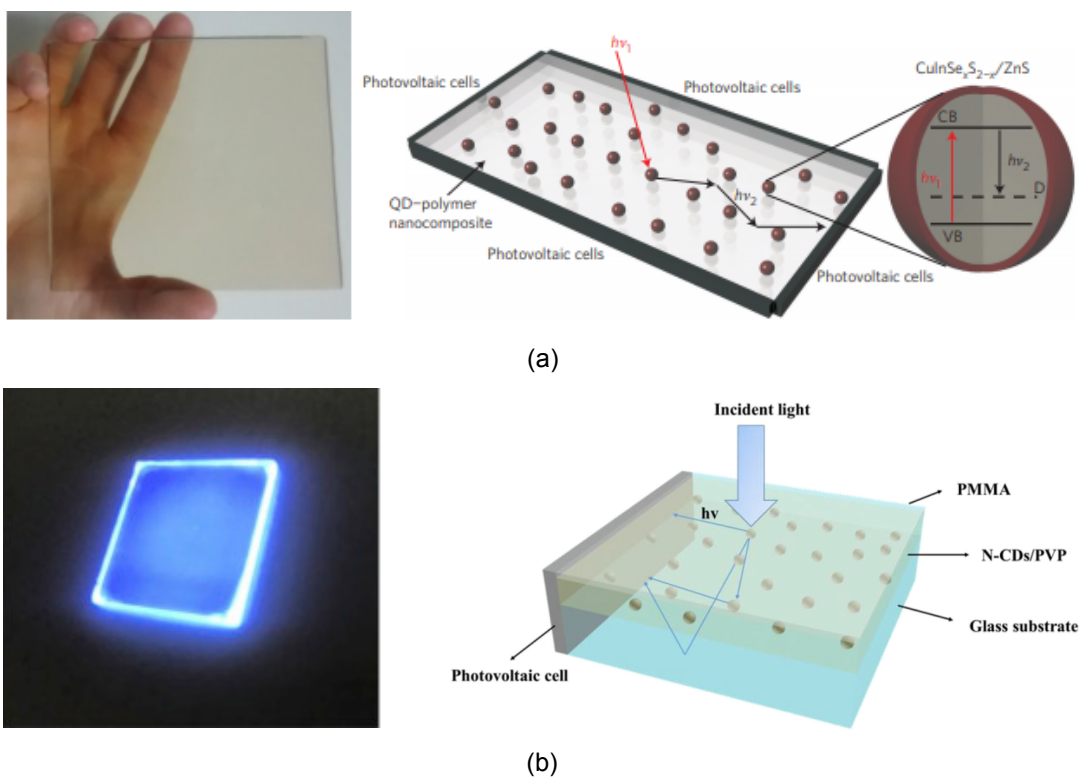


Figure 2.9: a) Photograph and schematic representation of a neutral-density LSC composed of a polymer matrix incorporating ZnS-coated CISES quantum dots (QDs), adapted from (Meinardi et al., 2017, b) Photograph and schematic illustration of the LSC consisting of PVP film and carbon dots (Wang et al., 2018).

The combination of escape cone losses and re-absorption losses can lead to a reduction in the number of photons trapped in an LSC. Escape cone losses can be reduced by using specular or diffuse reflectors. Diffuse reflectors have an added advantage that they can direct the photons directly to the edge of the LSC where

the PV cells are attached and it is the main reason for high efficiency in small LSC modules (Goldschmidt et al., 2009). Using mirrors on the backside can also limit the use of LSC in BIPV. Diffuse and specular reflectors cannot be placed on the top surface of the waveguide as they would block the incoming solar radiation. Photonic filters (Goldschmidt et al., 2009 as shown in Figure 2.10, Needell et al., 2018), polarization-independent filters (Boer et al., 2011) and wavelength selective filters (Bronstein et al., 2015, Song et al., 2017, Debije et al., 2009). These mirrors are transparent to short wavelengths and reflective at longer wavelengths where the fluorophore emits. Even though these mirrors, filters increase efficiency they can be difficult to manufacture in large scale. They can also increase the reflection in the absorption range of the dye as compared to the bare top surface (Peters et al., 2007). Dichroic dye molecules have been aligned in a liquid crystal host matrix so that their emission is directed towards the edge of the waveguide. The trapping efficiency was found to increase by 16% for vertically aligned dye molecules (Mulder et al., 2010). However aligning dye molecules can lead to a decrease in the absorption of incident solar radiation (Debije, Broer, and Bastiaansen, 2007).

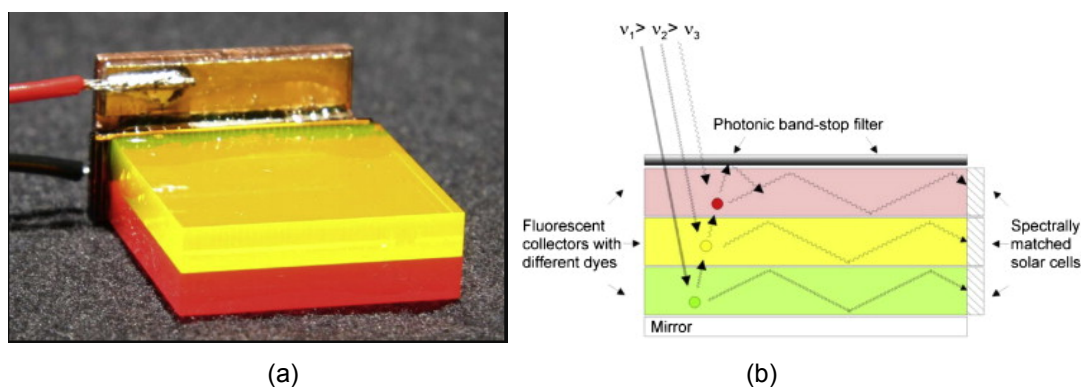


Figure 2.10: a) Photograph of a tandem LSC where solar spectrum is absorbed by multiple collectors with different fluorophores b) Schematic representation of the same structure with a photonic band stop filter on top to reduce escape cone losses. Adapted from (Goldschmidt et al., 2009).

High fluorophore doping concentration can increase the optical efficiency of LSC (Krumer et al., 2017). Depending on the configuration of LSC past a certain doping concentration the re-absorption losses increase, as the geometric gain in-

creases for large scale LSC so does the re-absorption and thermal losses. Thin-film LSCs were proposed instead of using bulk doped LSC (Viehmann and Frost, 1979). The main advantage of thin-film LSC is that they can reduce host absorption losses in the NIR region. This can be achieved by depositing the thin film on a substrate such as low iron, borosilicate glass unlike, PMMA they do not absorb in the NIR region. Thin-film also reduces the amount of polymer used in the device. If the substrate is made from glass this reduces the embodied energy of the device, (the embodied energy for glass is typically 10-25 MJ/kg whereas that for polymers is in the range 80-200 MJ/kg) (Hammond et al., 2008). However, for an identical optical density of bulk doped LSC and thin-film LSC, there is no change in the re-absorption losses (Bose et al., 2007). To achieve the same optical density thin film would require a higher concentration of fluorophore than a bulk doped LSC. Even though the path length for the trapped photons will be lower in a doped thin film the doping concentrations will be higher than a bulk doped LSC, therefore, the probability of re-absorption will remain the same. Only bulk doped LSCs have been considered in the work for this thesis mainly due to the ease of casting a bulk doped polymer waveguide as compared to spin coating polymer film on a substrate. Surface variations in thickness, cracking of polymer difficulty to remove the thin film are some of the problems that have been avoided by using a bulk doped LSC in this work.

Recently, an alternative technology of PLSC was proposed to overcome the losses in LSC and improve its optical performance (Chandra et al., 2012, El-Bashir, Barakat, and AlSalhi, 2013). MNPs are embedded in the polymer along with fluorophore. An increase in the power conversion efficiency of the PLSC relative to the LSC with no MNPs has been reported (El-Bashir, Barakat, and AlSalhi, 2014, Mateen et al., 2017) the different designs studied for PLSC till now in literature can be seen in Figure 2.11.

Buildings account for 40% of the energy consumed in Europe. By 2020, BIPV installation capacity is expected to exceed 11 GW (*BUILDING-INTEGRATED SO-*

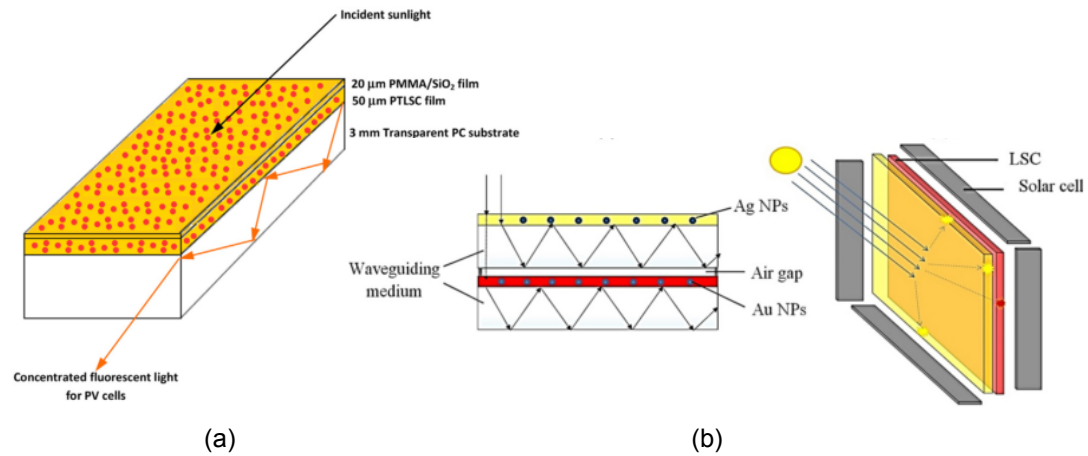


Figure 2.11: a) Schematic of a thin film PLSC layer with comarin dye and Au MNP, adapted from (El-Bashir, Barakat, and AlSalhi, 2014) b) Schematic representation of stacked plate PLSC layers with Au and Ag spherical MNPs with dye embedded in PMMA matrix (Mateen et al., 2017).

LAR). BIPV market is expected to grow to 26 billion dollars. LSCs are useful in BIPV applications such as windows, sound barriers, panels as shown in Figure 2.12. It is important to maximize the efficiency of the LSC devices, for their commercial integration into BIPV. PLSC offers an alternative to conventional LSC, PLSC can decrease the escape cone losses that occur in a conventional LSC.

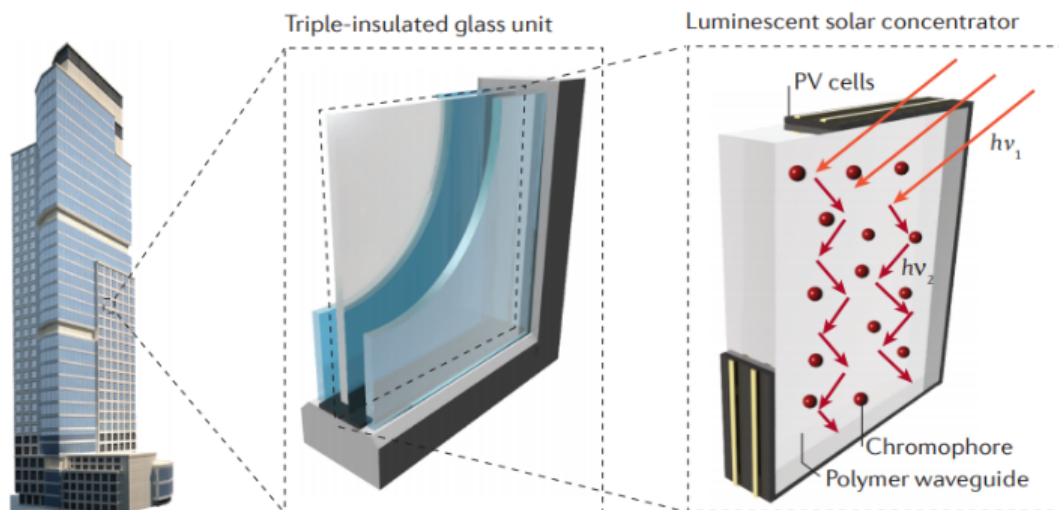


Figure 2.12: Schematic representation of a PV window consisting of triple insulated glass embedding LSC. (Meinardi, Bruni, and Brovelli, 2017)

Despite the remarkable performance of PLSC, there are many challenges in de-

vice optimization. Spacing between the MNP and the fluorophore, spectral overlap of MNP's extinction spectra with the absorption and emission spectra of the fluorophore can influence PLSC performance. In this thesis, the aim is to address these challenges and to optimize the MNPs in the host matrix for application in PLSC device. To utilize the interesting plasmonic properties of MNPs we need to understand the basics of surface plasmon resonance (SPR) and the interaction of MNPs with fluorophores.

2.7 Surface Plasmon Resonance-Revision

In the early 20th century, Gustav Mie published his pioneering work explaining the optical properties of MNP colloids (Mie, 1908). The Lycurgus cup (400AD) is the most famous example of surface plasmons in ancient times exhibiting different colors on illumination from inside and outside the cup (Barber and Freestone, 1990).

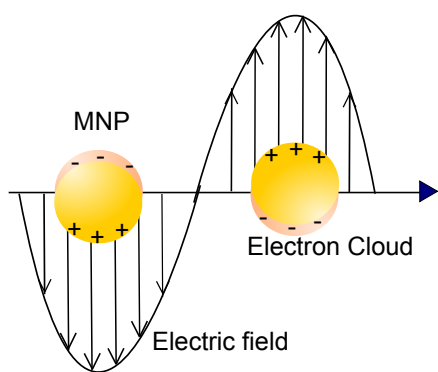


Figure 2.13: Schematic of light interaction with a spherical MNP.

Surface plasmons (SPs) correspond to the interactions between matter and the electromagnetic field of the light. A classical picture is more useful to understand the interaction of the electromagnetic field with a metal nanoparticle. A MNP can be described as a lattice with conduction electrons moving freely inside it (Fermi sea) (Zuloaga and Nordlander, 2011, Biagioni, Huang, and Hecht, 2012, Garcia, 2011). When light falls on the particle the

electromagnetic field of the light exerts a force on the conduction electrons to move to the surface of nanoparticle (NP) or displace the conduction band electrons with respect the nuclei which are positively charged as is represented in Figure 2.13. An electric dipole is created inside the NP, it creates an induced electric field inside the NP which is opposite to light and forces electrons back to the equilibrium

position. The situation is similar to a linear oscillator with a restoring force proportional to the displacement from the equilibrium position. After the electrons are displaced from the equilibrium position, if the field is now removed, the electrons will oscillate with a certain frequency called the resonant plasmonic frequency.

2.8 Surface plasmon resonance in MNPs

For Au, Ag and Cu, the resonant plasmon frequency falls in the visible range of light. Plasmons in NPs with a size much smaller than the wavelength of light are non-propagating excitations, called localized surface plasmons (LSPs), because the resulting plasmon oscillation is distributed over the whole particle volume. There is an increase in the electrostatic and kinetic energies associated with the electric field of the dipole. This increase in energy is countered by light extinction from the MNP. Larger electron oscillations correspond to larger light extinction which can be detected by the optical absorption spectrum. The absorption cross-section determines the absorbing efficiency of a particle. The extinction cross-section is the sum of the absorption and scattering cross-section and represents the efficiency of an MNP to remove photons from incident light (Kreibig and Vollmer, 1995, Maier, 2007). For noble MNPs the extinction cross-section can be ten times their geometrical cross-section (Garcia, 2011). Light absorption by an MNP has an exponential dependence on the MNP's extinction cross-section and is given by:

$$I(x) = I_0 \cdot e^{-c\sigma_{ext}x} \quad (2.10)$$

where I_0 being the initial intensity, c is the concentration of MNPs per unit volume, σ their extinction cross-section, x is the optical path length. A small increase in the small extinction cross-section can lead to large enhancement in light absorption.

Besides surface plasmons, other electronic excitations can take place in MNPs. In metals, the valence and conduction bands overlap, however some inner levels

might not split to form the continuous band and the system can then exhibit interband transitions (Dresselhaus and Dresselhaus, 1962). For bulk materials, these transitions are very unlikely however in NPs the energy bands are not so well-formed so the interband transitions are more prominent. The surface plasmon band is larger than the interband transition band and that can be explained by the same classical picture of surface plasmon.

2.9 Local electric field enhancement

The movement of conduction electrons results in charge accumulation on the surface of the MNP and consequently electric fields in a region larger than the MNP size as shown in Figure 2.14. There are wide regions around the MNP where the electric field has constructive (scattering) or destructive interference with the external field leading to a light extinction beyond NP volume (Maier, 2007).

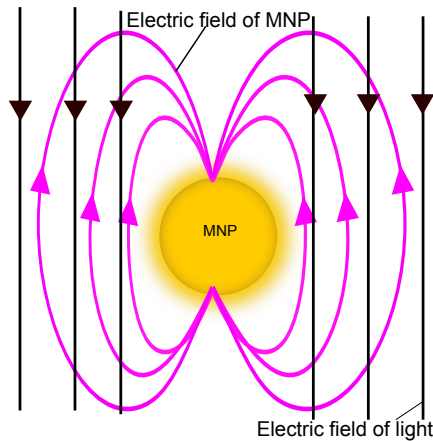


Figure 2.14: Illustration of electric field created by a MNP.

This mechanism can qualitatively explain the extinction cross section of MNPs when they are excited by light. The MNPs act as nanolenses i.e. they amplify the electromagnetic radiation in their surrounding, this behavior has been exploited in fluorescence modulation of fluorophores for application in PLSC. The local field enhancement factor (EF) is given by (Alonso-González et al., 2012, Maier, 2007):

$$EF(r) = \frac{E_{loc}(r)}{E_o} \quad (2.11)$$

where $E_{loc}(r)$ is the local electric field at point r and E_o is the incident electric field.

The points with the largest enhancement factor in NPs are called electromag-

netic "hot spots". The enhancement of the local electric field is limited to the near field zone. Large EFs are possible at the junction between dimers, trimers etc (Le Ru and Etchegoin, 2008). This is mainly due to the increase in the coupling of the particles while reducing their distance. But recent studies have shown that less than 1 nm, the EF decreases because of the appearance of quantum effects between the electronic densities of two NPs. The maximum estimated EFs for Au NPs is 10^2 - 10^3 (Toscano et al., 2012). Isolated nanorods have large enhancement of electric field on their edges also called the lightning rod effect (large enhancement of electrostatic field at sharp ends of a conductor) (Liao and Wokaun, 1982). The resonance condition is dependent on the shape, size and dielectric constants of both the metal and the surrounding material.

2.10 Factors influencing the surface plasmon resonance

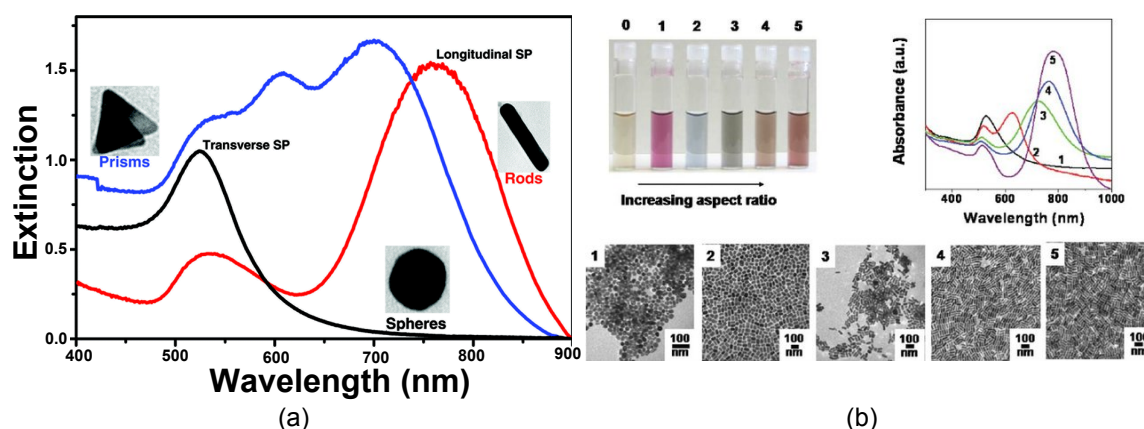


Figure 2.15: Extinction spectra of Au MNPs of different shapes, adapted from (Attia et al., 2015), b) The photograph shows aqueous solutions of 4 nm gold nanospheres (vial 0) and progressively higher aspect ratio gold nanorods (1 to 5). The optical spectra and TEM images for the particles in vials 1 to 5 are also shown. Scale bars in micrographs are all 100 nm. Adapted from (Murphy et al., 2008).

Shape: SPR peak wavelengths' width, position and number are determined by the shape of the NP (Xia and Halas, 2005) as shown in Figure 2.15. It was predicted that for small ellipsoids, the dipole approximation holds and the surface plasmon mode splits into two distinct modes (Gans, 1915). The reduction in MNP symme-

try is a good way to modify the position, intensity, and number of SPR. Nanorods mainly show two plasmon resonances one due to the transverse oscillation of the electrons and the other due to longitudinal oscillation along the major axis of the nanorod. The transverse band is slightly blue-shifted with respect to the SPR of an equivalent sphere, while the longitudinal band is red shifted and is more intense. Increasing the aspect ratio, the longitudinal band can be red-shifted from visible to NIR for Au. The transverse resonance does not strongly depend on the aspect ratio. This behavior is especially beneficial to tune the MNP optical properties to match the absorption and emission spectra of the fluorophores in a PLSC. The optical properties can vary even between ellipsoids and cylinders depending on their hemispherical or flat ends (Prescott and Mulvaney, 2006). Gold core silver shell nanocuboids were found to have four distinct plasmon bands corresponding to the longitudinal, transverse dipole mode and an octupolar mode (Kleinman et al., 2012). The extinction spectra of various shaped Au and Ag MNPs can be seen in Figure 2.15.

Effect of surface chemicals: In this work, MNPs have been transferred to different media by modifying their surface. Thiolation and physisorption of alkylamines or citrate change the SPR properties in three ways:

- By introducing new relaxation pathways for the electrons there will be an increase to the non-radiative relaxation rate (Link and El-Sayed, 2003). Density functional theory states that the electron density of states near the Fermi level of Au NPs changed with the introduction of these ligands. A higher change was observed for thiols than amines (Aruda et al., 2013). This effect is known as the chemical interface damping (Aruda et al., 2013).
- A shell of non-metallic form around Au while also changing the bond order and that leads to a reduction in the effective size of the NPs (Malola et al., 2013). In case of a thiolated monolayer on Au nanosphere Au₃₁₄(SH)₉₆, the SH ligand takes one electron from the sp band of Au leaving 218 number of effective valence electrons (Malola et al., 2013).

- The ligands cause a change in the dielectric environment of MNPs consequently changing the real part of the refractive index (Mayer et al., 2010).

The SPR redshifts with increasing dielectric constant and vice versa.

All the effects mentioned above are illustrated in Figure 2.16. The effect of the chemicals also depends on the MNP size, shape and the type of chemical.

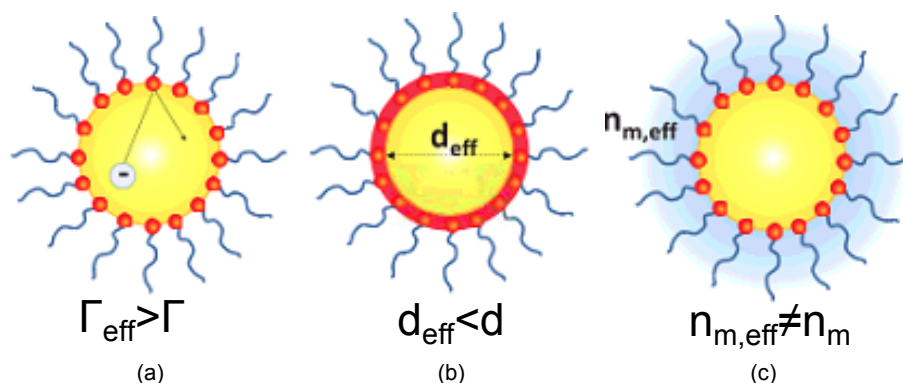


Figure 2.16: Effect of the surface chemical reactions a) increase in the non-radiative lifetime of the MNP, b) decrease in the effective size of the MNP, c) change in the non-absorbing dielectric medium around the MNP. Adapted from (Amendola et al., 2017).

Effect of the refractive index of the medium: A change in color of the nanorod solution is observed when they are dispersed in different refractive index solvents. In this work, anisotropic MNPs are dispersed in organic solvent/polymer with different refractive index than water, therefore it is important to understand the dependence of plasmonic resonance on the refractive index of the surrounding medium.

The light wavelength at the vicinity of the MNP is determined by the dielectric function of the surrounding medium. Charge accumulation during SP excitation creates an electric field near the MNP. Due to this field, the dielectric medium is polarized and results in charge accumulation at the interface between the dielectric and MNP, which partially compensates the charge accumulation due to the movement of electrons in the MNP. The larger dielectric function will mean larger polarization charge and larger effect on SP. A reduction in the net charge on the NP surface implies a reduction in the restoring force and thereby leading to a smaller

resonant frequency. This explains the redshift of the plasmon band observed for particles in medium with a higher dielectric constant as shown in Figure 2.17. For small aspect ratio nanorods, a small change in the medium refractive index resulted in a large variation of the contribution of optical scattering to the total extinction (Lee and El-Sayed, 2005). The increase in the resonant intensity with an increase in the dielectric function of the medium is expected for a damped oscillator.

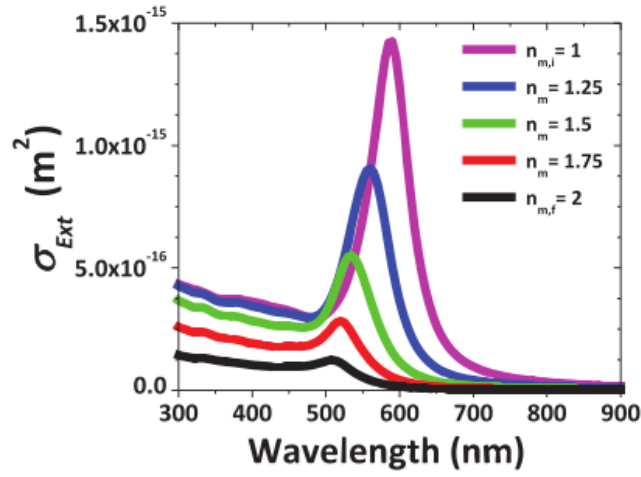


Figure 2.17: Mie model calculation of SPR of 20 nm Au MNPs in a non-absorbing dielectric medium with refractive index increasing from 1 to 2 with steps of 0.25. Adapted from (Blaber, Arnold, and Ford, 2010).

2.11 Metal enhanced fluorescence

A fluorophore is an oscillating dipole which oscillates at a high frequency and radiates short wavelengths. The excitation electric field experienced by a fluorophore is affected by: 1) interactions of the incident light with the nearby metal surface, 2) interaction of the fluorophore oscillating dipole with the metal surface. The brightness of a fluorophore functionalized MNP can be written as (Chen, Munechika, and Ginger, 2007):

$$Y_{app} = \gamma_{exc}(\omega_{exc})Q_{em}(\omega_{em})\eta_{coll}(\omega_{em})\sigma \quad (2.12)$$

where γ_{exc} is the near-field excitation rate at the excitation frequency ω_{exc} , Q_{em} is the quantum yield for far field emission at the emission frequency ω_{em} , η_{coll} is the collection efficiency of the far-field light in the experimental geometry and σ is a normalization factor accounting for attachment density and total area excited. Although straightforward, the σ and η_{coll} factors in equation 3.4 are often neglected (Chen, Munechika, and Ginger, 2007). The excitation rate of the fluorophore depends on both the absorption coefficient of the fluorophore and the enhanced local electric field intensity as is evident by (Bharadwaj and Novotny, 2007):

$$\gamma_{exc} = |p \cdot [E_o(r, \omega) + E_{NPs}(r, \omega)]|^2 \quad (2.13)$$

where E_o is the incident electric field, E_{NPs} is the electric field enhanced by the MNP, r is the position vector, p is the transition dipole moment and ω is the transition frequency. The near field enhancement is dependent on the frequency and is maximum, highest excitation rate should be achievable when the LSPR peak of the MNP directly overlaps the absorption spectrum of the fluorophore.

The fluorescence quantum yield Q_o of a fluorophore depends on the radiative relaxation rate and non-radiative relaxation rate and given as follows (Lakowicz, 2001):

$$Q_o = \frac{\Gamma}{\Gamma + k_{nr}} \quad (2.14)$$

where Γ is the radiative decay rate and k_{nr} is the non-radiative decay rate. When an MNP is in the proximity of the fluorophore there are additional terms that influence the quantum yield such as non-radiative and radiative relaxation rates due to the MNP. A simplified Jablonski diagram can be seen in Figure 2.18. The MNP increases the radiative rate of the molecule and decreases the lifetime of the fluorophore as shown in Figure 2.18, by stimulating photon emission due to the local electromagnetic field enhancement. On the other hand, electromagnetic energy

transfer may occur from the fluorophore to the metal due to the charges in the NP induced by the fluorophore dipole. In this case, the modified quantum yield of the fluorophore Q_m near the metal surface is given as:

$$Q_m = \frac{\Gamma + \Gamma_m}{\Gamma + k_{nr} + k_{nr}^m} \quad (2.15)$$

where Γ_m is the radiative decay rate due to metal and k_{nr}^m is the non-radiative decay rate due to the nearby MNP. For an efficient fluorophore in free space $\Gamma \gg k_{nr}$ and $Q_0 \approx 1$ the radiative term due to the MNP will have a limited role in quantum yield. In low quantum yield fluorophores, Γ_m can strongly increase quantum yield (Lakowicz, 2001, Lakowicz, 2004). This is possible only if the non-radiative relaxation due to the MNP is less than the radiative relaxation rate.

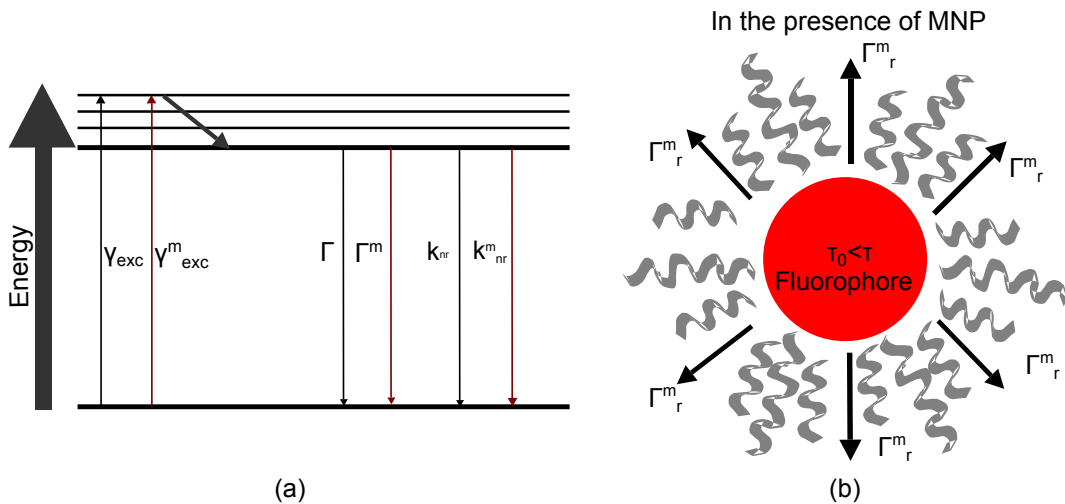


Figure 2.18: a) Simplified Jablonski diagram of fluorophore in the presence of MNP depicted with black and red arrows respectively, b) Illustration of high photon mode density in the presence of MNP around a fluorophore.

Fluorescence enhancement factor depends on the enhancement of the absorption cross-section and the enhancement/quenching due to the quantum yield. It can either be very high up to 1000 but also very low <1 . The magnitude of the quenching of fluorescence, local field enhancement and enhancement of radiative decay rate depends on the location of the fluorophore with respect to the MNP and orientation of its dipole with respect to the MNP. Quenching prevails

on the radiative enhancement for small NPs and at a short distance (less than 5-10 nm) (Novotny, 1996) and vice-versa (Lakowicz, 2001, Lakowicz, 2004, Jahn et al., 2016). An optimum distance of the dye at which fluorescence enhancing factor is maximized is normally assumed to be in between 5 and 20 nm (Jahn et al., 2016). Anisotropic MNPs may lead to larger fluorescence signals at certain MNP-fluorophore distance.

2.12 Silver a unique metal for plasmonics

In plasmonic interaction/coupling, it is important to choose a metal that can support strong surface plasmons at a desired resonance wavelength (Lal, Link, and Halas, 2007). For silver, this range is from 300 to 1200 nm. The ability of a metal to support SP is dependent on the dielectric function which includes real ϵ_r and an imaginary ϵ_i part. Both parts of the dielectric function vary with excitation wavelength. The Figure 2.19 shows the plot of the dielectric function as a function of wavelength. Large value of ϵ_i is similar to other non-metal materials, the value should be closer to zero to support a strong resonance and this condition is satisfied by Ag as can be seen in Figure 2.19. The SP strength is directly proportional to the quality factor Q which can be described as:

$$Q = \frac{w(d\epsilon_r/dw)}{2\epsilon_i^2} \quad (2.16)$$

In general, Q should be larger than 10 for most plasmonic applications. Ag has the largest Q factor across 300-1200 nm (Le Ru and Etchegoin, 2008). Inter-band transitions also play an important role in dampening the SP modes. For Ag, these transitions take place at a much higher frequency than the LSPR however, for Au these transitions limit the LSPR to wavelengths higher than 500 nm. Ag compared to other metals is unique in terms of plasmonic ability and material cost which is much lower than Au or Pt.

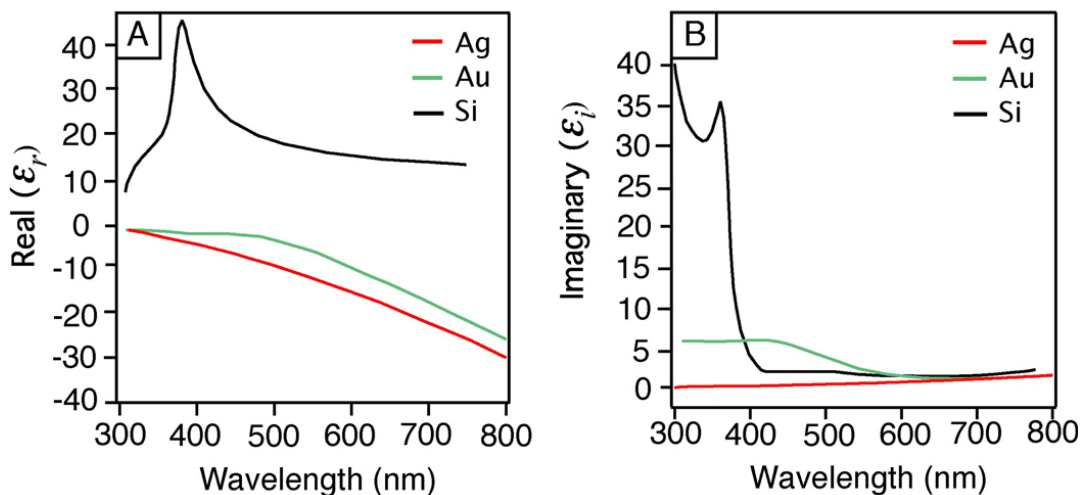


Figure 2.19: Plot of the imaginary and real part of the dielectric function as a function of wavelength.

2.13 Alignment of nanorods in external electric field

Aligning nanorods in the vicinity of a fluorophore such as a QD can polarize its emission. Emission polarization of anisotropic InGaAs QD by aligning Au nanorod (AuNR) in a hybrid system has been theoretically studied (Cheng, Liu, and Wang, 2008). The fluorophores fluorescence can also be modulated by aligning the dipole of the MNP.

Au and Ag MNPs have an induced dipole moment in an external electric field. Dielectrophoretic force is the force on conducting dielectric spheres immersed in a dielectric medium and subjected to a non-uniform electric field. The MNPs have a translational motion towards the high field region this is due to the dielectrophoretic force which drives the particles to regions of higher field strengths also known as positive dielectrophoresis. Negative dielectrophoresis occurs when the conductivity or the permittivity of the medium exceeds the particle (Ahmed et al., 2009). At frequencies, higher than 10 Hz negative dielectrophoresis occurs for gold particles in water (Gierhart et al., 2007). For nanorods, the shape of a prolate spheroid can be approximated for simplicity as seen in Figure 2.20.

The induced dipole moment can be written as:

$$p = a_0 E(t) \quad (2.17)$$

where a_0 is the polarizability tensor of the particle and E is the external electric field. The polarizability tensor for a nanorod can

be written in terms of the longitudinal and

transverse polarizability acting along or perpendicular to the symmetry axis respectively. An anisotropic particle in an electric field experiences torque that tends to align one of the major axes in the direction of the electric field.

The extinction spectra of the nanorods are strongly dependent on the degree of orientation of the rods and direction of the polarized light with respect to the applied electric field. In the absence of electric field, the gold nanorods are randomly oriented and show two plasmon bands longitudinal and transverse. In the presence of an electric field when the incident light is polarized parallel to the electric field, the transverse peak can disappear completely by aligning the rods. Conversely, for perpendicularly polarized light, the transverse peak remains present and the longitudinal peak is absent (Zande, Koper, and Lekkerkerker, 1999).

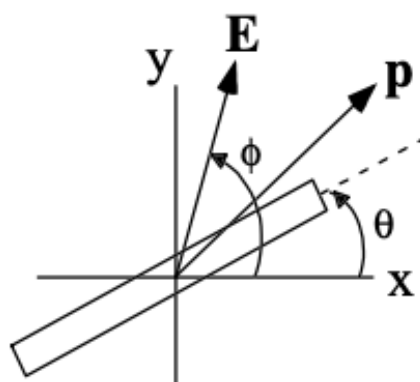


Figure 2.20: Sketch of the dipole moment on nanorod

2.14 Synthesis of Gold Nanorods

As discussed in section 2.10 plasmonic interaction between MNPs and fluorophores depends on various parameters one of them is the SPR frequency and spectral overlap of SPR peak with the absorption or emission peak of fluorophores. In this Ph.D. work synthesis of anisotropic MNPs was carried out with control over their size, shape and taking into account the position of their SPR peak relative to the fluorophore used in the PLSC device. Therefore it is important to review the synthetic

processes for the MNPs and the effect of various additives and factors such as pH and temperature on the yield, aspect ratio and monodispersity of the nanorods.

Gold nanorods can be synthesized mainly using three methods; 1) Template method 2) Electrochemical method 3) Seeded growth method. In this research the seeded growth method to synthesize gold nanorods has been used, the nanorods can be seen in Figure 2.21. In early 1990s, this method has been reported to make more monodisperse nanoparticles (Mulvaney, Giersig, and Henglein, 1993, Henglein and Giersig, 1994). Seed mediated approach was used to grow spherical particles by reduction of the gold precursor using hydroxylamine (a weak reducing agent). The growth of citrate capped spherical gold nanoparticles (12 nm) was studied and it was deduced that additional nucleation takes place even in the presence of seeds (Jana, Gearheart, and Murphy, 2001a). Controlling the rate of addition of the reducing agent and the chemical reduction potential of the reducing agent can inhibit this additional nucleation. Using this information 3.5 nm gold seeds was prepared using sodium borohydride as the reducing agent and citrate as capping agent (Jana, Gearheart, and Murphy, 2001c). It is important to inhibit secondary nucleation during the growth stage, which can be achieved using ascorbic acid as a weak reducing agent that cannot reduce gold salt without the presence of the seeds. Below are the main additives in the growth process:

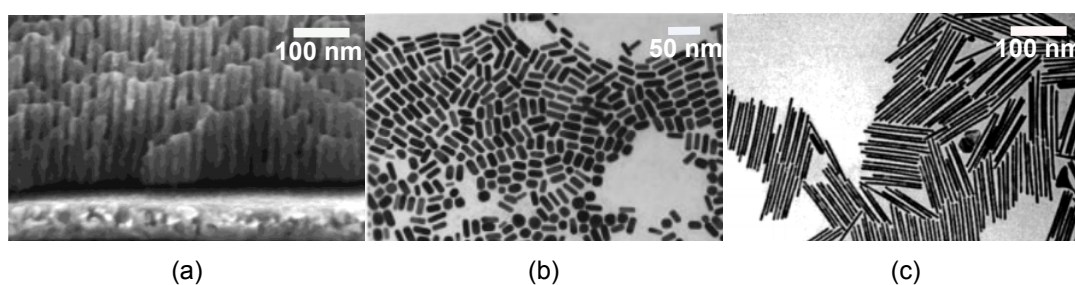


Figure 2.21: a) TEM image of Au nanorods obtained using template method (Zande et al., 2000), b) TEM image of Au nanorods obtained using electrochemical method with aspect ratio of 6.1 (Chang et al., 1999), c) TEM image of shape separated Au nanorods prepared by seed mediated synthesis (Jana, Gearheart, and Murphy, 2001d).

- **Surfactant:** CTAB is used for the formation of rod-shaped NPs in aqueous

media. It has been proposed that CTAB preferentially binds to the sides of the penta-twinned rods as compared to the tips thus promoting the growth of the nanorods (Johnson et al., 2002). It was found that the length of the surfactant tail is crucial to control the yield and the length of the nanorods (Gao, Bender, and Murphy, 2003).

- **Precursor:** Three different oxidation states of Au is involved, Au(III): precursor, Au(I): intermediate and Au(0): nanoparticles (Edgar, McDonagh, and Cortie, 2012). In the presence of CTAB $[\text{AuCl}^-_4]$ gets replaced by bromide ions to form $[\text{AuBr}^-_4]$ which is evident by a color change from yellow to orange. This ligand change influences the redox potential and therefore the growth kinetics.
- **Reducing agent:** The most widely used weak reducing agent is ascorbic acid. The reduction of Au(III) to Au(I) takes place on adding the ascorbic acid to the growth solution. Ascorbic acid has a pH and temperature-dependent reduction potential, which increases under more basic conditions (Gramlich, Zhang, and Nau, 2002).
- **Presence of AgNO_3 :** It has been found that the addition of silver nitrate to the growth solution increased the yield of the gold nanorods up to 50% (Jana, Gearheart, and Murphy, 2001b). Adjusting the amount of silver ions (while keeping the amount of seed solution constant), can tune the SPR and achieve certain aspect ratio of the rods. However, above a critical silver concentration, the aspect ratio of the nanorods decreases again (Nikoobakht and El-Sayed, 2003).
- **Au seeds:** The control of the aspect ratio, yield and monodispersity of the nanorods is dependent on the stability of the seeds, temperature, and concentration of the surfactant. A new variation of the seed-mediated approach was proposed by using CTAB capped rather than citrate capped seeds (Nikoobakht and El-Sayed, 2003). This major impact on the shape yield is due to the

formation of single-crystalline rods with CTAB capped seeds unlike pentatwinned and mono twinned population due to citrate capped seeds.

2.15 Synthesis of gold core silver shell nanocuboids

Pure silver nanorods and nanowires were synthesized by a wet seed-mediated chemical method (Jana, Gearheart, and Murphy, 2001e), and it marked an important step forward. However, they could not achieve good shape and size uniformity compared to their gold counterpart. The deposition of silver onto gold nanorods by reducing $AgCl_4$ using hydroxylamine was proposed (Ah, Hong, and Jang, 2001). They found that the thickness of the silver shell could be controlled and on increasing the concentration of the silver salt or reducing agent beyond a certain limit the particles assumed a dumbbell shape. This is due to the preferential absorption of silver on the end surfaces of the gold nanorods (Huang, Yang, and Chang, 2004). Au@Ag nanorods were synthesized by reducing $AgNO_3$ and stabilizing the colloids by either one of these chemicals: CTAB (Huang, Yang, and Chang, 2004), CTAC, BDAC (Tebbe et al., 2015), citrate or polyvinylpyrrolidone (PVP) (Liu and Guyot-Sionnest, 2004) as can be seen in Figure 2.22.

Single crystal nanorods have an octagonal cross-section with eight high index {520} lateral facets and a combination of {110} and {111} facets at the tips (Carbó-Argibay et al., 2010). Such nanorods were grown into Au@Ag cuboids with six well defined low index {100} facets due to preferential absorption of silver on {100} facets (Gomez-Grana et al., 2013).

- **Surfactant:** Benzylhexadecyldimethylammonium chloride (BDAC) and hexadecyltrimethylammonium chloride (CTAC) were used to study their impact on nanoparticle growth behavior (Tebbe et al., 2015). The authors observed that the overgrowth rate of BDAC was an order of magnitude lower than CTAC. In a CTAB solution silver shell formation frequently gave dumbbell (Huang, Yang, and Chang, 2004) and symmetric boat like silver shells (Tebbe et al., 2015).

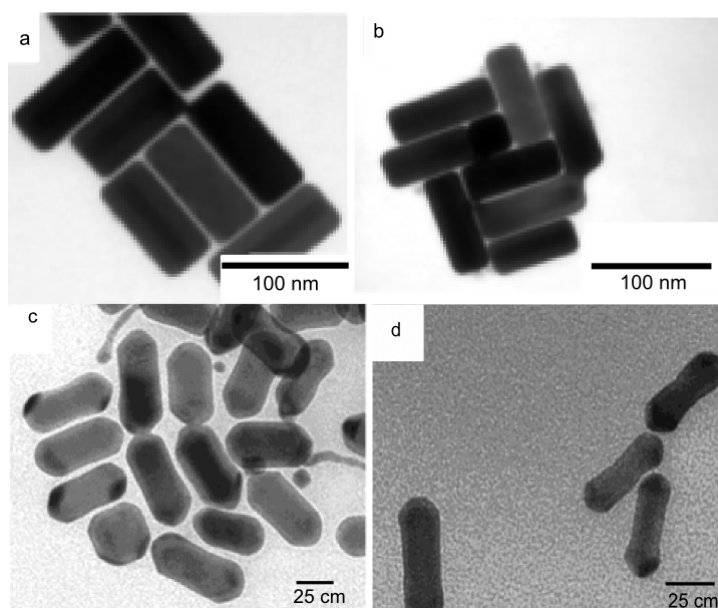


Figure 2.22: TEM images of Au@Ag nanocuboids capped with a) CTAC, b) BDAC, c) Citrate, d) PVP. Adapted from (Liu and Guyot-Sionnest, 2004, Tebbe et al., 2015).

- **Precursor:** Silver chloride has been used as the precursor for silver shell where four distinct peaks for the cuboids were observed (Okuno et al., 2010). The same group also synthesized Au@Ag nanocuboids using silver nitrate as the precursor (Okuno et al., 2008). With silver nitrate, the pH of the reaction needs to be controlled as at high pH values > 4.6 leads to formation of colloidal silver particles and not the formation of silver shell on gold nanorods (Okuno et al., 2010).
- **Reducing agent:** Ascorbic acid redox potential is not sufficient to reduce Ag^+ to Ag^0 at room temperature and acidic conditions. One way to accelerate silver ion reduction in acidic conditions using ascorbic acid is to increase the temperature of the growth solution. On increasing the temperature to 60–65°C ascorbic acid can reduce silver and the reduction is complete within 3 hours (Gomez-Grana et al., 2013).
- **Seeds:** Au NRs are used as seeds to synthesize Au@Ag nanocuboids. The overgrowth of the shell was divided into three steps; accelerated growth, con-

stant growth rate, and deceleration with edge sharpening (Tebbe et al., 2015).

2.16 Conclusions

In European countries like UK and Ireland, most of the radiation is diffuse and upcoming solar energy technologies need to work efficiently in diffuse and direct solar radiation. LSCs can concentrate both diffuse and direct solar radiation by having an acceptance angle of 90 degrees. The simple design of LSC, its low cost, static and passive nature makes it an ideal choice for BIPV. The optical efficiency of an LSC is dependent on various factors such as total internal reflection efficiency, the quantum yield of the fluorophore, the reflection of the light from the host matrix, etc. Escape cone losses, re-absorption losses due to the fluorophores, energy loss due to Stokes'-shift and narrow absorption band of the fluorophores inhibit the commercial application of the device. Recent research to fabricate near-unity PLQY and zero re-absorption fluorophores has led to interesting results. Studies have been done to increase the trapping efficiency and thereby reducing the escape cone losses in the device by aligning the fluorophores. However, further research is needed to realize LSCs with higher optical efficiencies by countering the loss mechanisms.

A novel approach to address the re-absorption and escape cone losses is by exploiting the plasmonic interaction of MNPs and fluorophores. The study done up till now regarding PLSCs has employed spherical Au, Ag MNPs along with fluorophores in a stacked plate and thin-film configuration. But, no study has been performed yet on how the spectral overlap with the absorption/emission spectrum of fluorophore can influence the overall performance of the device. In this work, anisotropic MNPs will be used with fluorophores in a homogeneous LSC device as the anisotropy of the MNPs can give better control of tuning the surface plasmon resonance to the absorption/emission bands of fluorophores.

The localized SPR in the MNPs has two important effects 1) they have an optical extinction maximum at the SPR frequency with the extinction cross-section much

larger than their geometrical size, 2) the electric field near the particle surface is greatly enhanced and rapidly falls off with distance. The SPR peak is greatly influenced by the shape, size of the MNP, the surrounding dielectric medium and the chemical interactions on the surface of the MNP. The SPR peak is also affected by modifying the MNP environment and surface. All these factors have been taken into consideration when embedding MNPs in the host matrix for PLSC. The radiative decay rate can be modified by the presence of MNP in the vicinity of the fluorophore and thus an MNP can change the quantum yield of the fluorophore. It is crucial to control the various parameters such as the spectral overlap of the SPR band of MNP with the absorption/emission spectra of the fluorophore, spacing between the MNP and the fluorophore, orientation of the MNP with respect to the fluorophore, position of the SPR peak with respect to the absorption/emission band of fluorophore to avoid quenching of emission from the fluorophore in the PLSC device. The dynamics of alignment of Au NRs in an electric field have been emphasized, the electro-optical response depends on the shape, size and the geometry of the experimental setup.

Seed mediated synthesis of gold nanorods is most commonly used and gives good control over the aspect ratio of the nanorods. Mainly the gold seeds for this synthesis are either coated with sodium citrate or CTAB, with the CTAB seeds mainly giving a higher yield of the nanorods. To exploit the unique plasmonic property of Ag gold core silver shell nanocuboids can be useful for application in PLSC device as monodisperse and stable Ag nanorods can be difficult to synthesize.

Chapter 3

Materials and methods

This chapter is mainly divided into three core sections: 1) the materials used in this study, 2) experimental techniques for characterizing MNPs and LSC/PLSC waveguides 3) fabrication methodology for LSC/PLSC waveguides and device characterization techniques. The first section lists all the materials used in the synthesis of MNPs and the fabrication of LSC/PLSC waveguides. The main experimental techniques used in this study for optical characterization, imaging and concentration analysis of MNPs are discussed. The results from these techniques help form an informed decision about the optical, structural properties and concentration of MNPs to be used in the PLSC devices. There is an overlap in the techniques used in the characterization of MNPs and the waveguides, such as the UV-VIS absorption spectrometry. The methodology of LSC and PLSC waveguides fabrication in Silicone encapsulant polymer (host matrix) is presented. Finally, the experimental setup for the electrical characterization of fabricated devices in indoor and outdoor conditions is discussed.

3.1 Materials

This work investigates the incorporation of anisotropic MNPs in an LSC device. The materials used for the fabrication, functionalization and phase transfer of anisotropic Au NRs and Au@Ag NCs are presented in Table 3.1. The information regarding the fluorophores and host matrix material used in the PLSC device

is provided.

| Materials | Properties | Applications |
|---|--|---|
| Gold (III) chloride trihydrate ($HAuCl_4 \cdot 3H_2O$) | Mw: 393.83 g/mol, High purity >99% | Precursor for synthesizing Au NRs |
| Silver nitrate ($AgNO_3$) | Mw: 169.87 g/mol, reacts with metal spatula | To increase yield of Au NRs and used as a precursor for silver shell of Au@Ag NCs |
| Sodium borohydride ($NaBH_4$) | Mw: 37.83 g/mol, Strong reducing agent, hygroscopic | Reducing agent in Au seeds solution |
| Hexadecyltrimethyl ammonium bromide (CTAB) | Cationic surfactant, toxic | Capping agent for Au seeds and Au NRs |
| Hexadecyltrimethyl ammonium chloride (CTAC) | Cationic surfactant, toxic | Surfactant exchange to synthesize Au@Ag NCs |
| Ascorbic acid ($C_6H_8O_6$) | Mild reducing agent, reduction dependent on pH and temperature | Used in growth solution of Au NRs |
| Dichloromethane (CH_2Cl_2) | Volatile and toxic, refractive index 1.42, boiling point 39.6°C | Organic solvent for stock solution of Au NRs and Au@Ag NCs |
| Methanol (CH_3OH) | Highly toxic and volatile | Phase transfer agent for Au NRs and Au@Ag NCs |
| Gold and silver standard solutions | 1000 mg/L in nitric acid | Standard solutions for ICP-MS measurements |
| Deionized water | pH neutral, refractive index 1.3 | Used as solvent for MNP synthesis process |
| Silicone encapsulant polymer (EI1184) | Two part polymer, specific gravity of 1.04, refractive index 1.42, pot life 24 minutes | Host matrix for LSC/PLSC fabrication |
| Titanium dioxide (TiO_2) spherical MNPs | Size 350 nm | Used to fabricate diffuse reflectors |
| Lumogen F Red305 | Absorption peak ~576 nm, emission peak ~613 nm, density 1.4 g/cm ³ , PLQY in dichloromethane >95% | Fluorophore used in LSC/PLSC |
| ZnCuInS/ZnS core shell QDs | Absorption peak ~570 nm, emission peak ~700 nm | Studied in the host matrix |
| PEG-SH O-[2-(3-Mercaptopropionylamino)ethyl]-O'-methylpolyethylene glycol | Mw: 5000 g/mol | Used for functionalization of Au NRs and Au@AgNCs |

Table 3.1: Summary of the chemicals, host matrix, fluorophores and their properties used in this study.

3.2 Centrifugation

A centrifuge was used in this work for purification and removal of by-products from as-synthesized MNPs. The theory of centrifuge is based on the principle of sedimentation, where the acceleration at centripetal force causes denser substances to separate along the radial direction at the bottom of the tube. The different forces acting on the particles are represented in Figure 3.1. They are as follows; the centrifugal force, $F_c = \omega^2 r m$, the buoyant force, $F_b = -\omega^2 r m_o$, the Brownian fluctuating force F_f and the viscous drag force, $F_d = -\zeta v$. Where ω is the angular speed, m is the mass of the particle, m_o is the mass displaced by the particle, r is the distance from the center to the location of the particle, v is the sedimentation velocity, ζ is the drag coefficient. At equilibrium this $F_{total} = F_c + F_b + F_f + F_d = 0$ gives the Svedberg coefficient which is a measure of the sedimentation rate (Sharma, Park, and Srinivasarao, 2009).

For rods, the Svedberg coefficient is directly proportional to the square of the diameter, therefore, the sedimentation is mainly controlled by the diameter of the nanorods relative to spheres (Sharma, Park, and Srinivasarao, 2009). Spheres are a common by-product of Au NR synthesis process. A centrifuge has three basic components: a rotor, a drive shaft, and a motor. The centrifuge used in this study is the

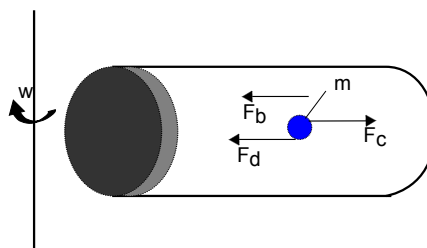


Figure 3.1: Schematic of a centrifuge tube with particles inside that need to be separated and the various forces acting on the particle

model 5804R (Eppendorf) shown in Figure 3.2. It has a fixed-angle rotor for high-speed applications in tubes from 0.2 mL to 85 mL. Centrifugation speed of up to 20,913 \times g (14,000 rpm) can be achieved. Depending on the size and shape of the MNPs the speed will need to be optimized to achieve shape separation. Temperature range from -9 $^{\circ}$ C to 40 $^{\circ}$ C and a function for fast pre-cooling is available. Continuous cooling to maintain a constant temperature after the run has been completed is provided by the instrument.

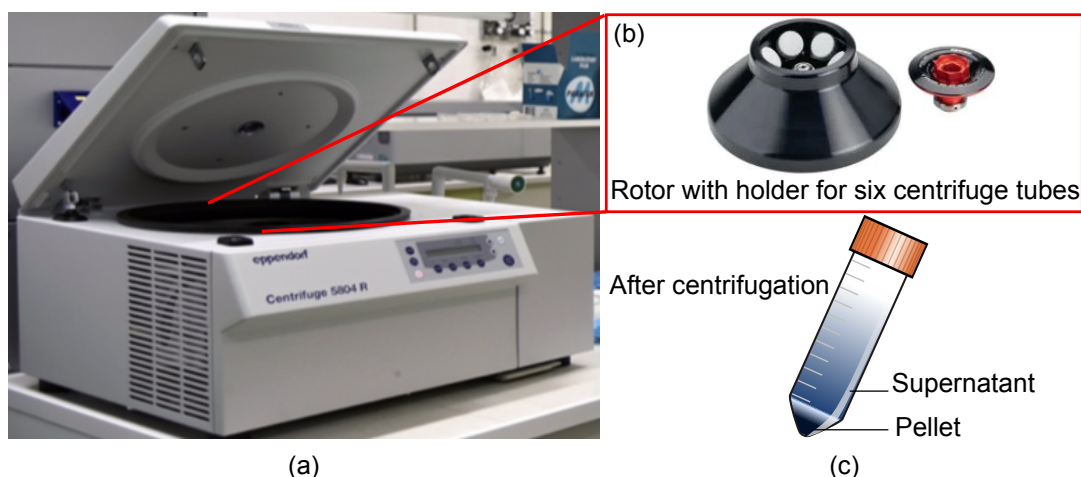


Figure 3.2: Photograph of a) centrifuge b) rotor used in this work, c) diagram of a centrifuge tube with pellet and supernatant after centrifugation.

3.3 UV-VIS spectrometry

The extinction spectra of the MNPs, the absorption spectra of the fluorophores and the LSC/PLSC waveguides was taken via a UV-VIS spectrometer. Optical spectroscopy is based on the Bohr-Einstein relationship described by:

$$\delta E = E_2 - E_1 = h\nu \quad (3.1)$$

where h is the Planck's constant and ν is the frequency of light. Equation 3.1 links the discrete atomic energy states with the frequency of the electromagnetic radiation. Absorbed or emitted radiation of frequency can be assigned to specific energy levels difference E_i . UV-VIS spectroscopy occupies only a narrow wavelength range from 200-800 nm. Nevertheless, this range is extremely important since the energy difference corresponds to the electronic states of the atoms. The mathematical-physics basis of the light absorption measurements is determined by the Bougert-Beer-Lambert law and is presented by:

$$\log_{10}\left(\frac{I_0}{I}\right) = \log_{10}\left(\frac{100}{T_r\%}\right) \equiv A = \epsilon \cdot c \cdot d \quad (3.2)$$

where $A = \log\left(\frac{I_0}{I}\right)$ is the absorbance and $T_r = \frac{I}{I_0} \cdot 100$ is the transmittance in %, ϵ is the molar extinction coefficient, I_0 is the intensity of light entering the sample, I is the intensity of light emerging from the sample, c is the concentration of the sample and d is the path length of the sample in cm.

The extinction comprises of both scattering and absorption. The UV-VIS spectroscopy can be applied for quantitative and qualitative analysis. The qualitative analysis can provide details of the shape and size of MNPs, and the quantitative analysis can optimize the number of MNPs and consequently the concentration, mainly undertaken for spherical particles (Haiss et al., 2007).

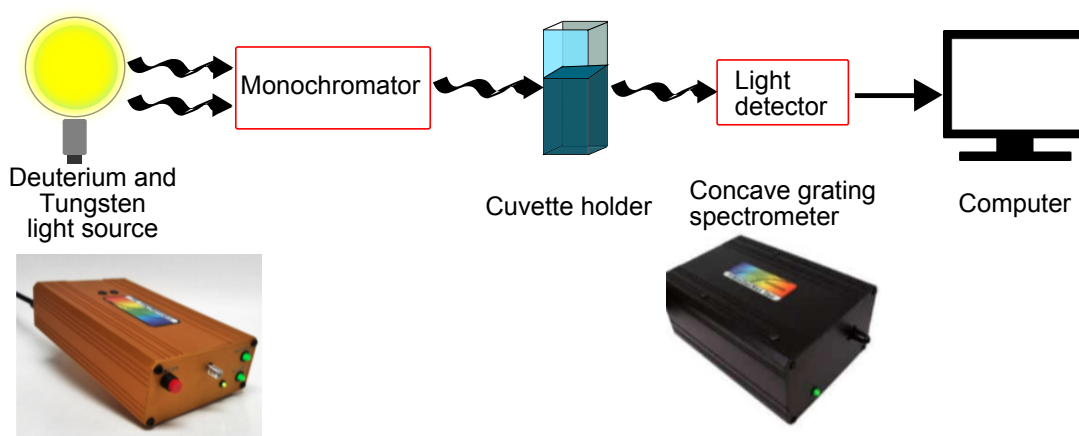


Figure 3.3: Simplified optics ray diagram of a single beam configuration, with the photographs of the light source and spectrophotometer used in this study.

A single beam spectrophotometer was used in this work as shown in Figure 3.3, all the light passes through the sample holder and the advantage of such configuration is that it is simple and economical. Two different UV-VIS spectrometers were used, one for the measurement of the liquid samples by using a cuvette to hold the solutions and the other employed an integrating sphere for the measurement of solid samples that is discussed in section 3.3.1. StellarNet UV-VIS light source was used for the measurements of liquid samples. It is a miniature deuterium and tungsten-halogen light source that covers the 190-1100 nm range. The lamp combines the deuterium spectrum and the tungsten halogen spectrum to form a single optical path. The spectrometer used was also by StellarNet, it used holo-

graphic concave gratings that are produced with grooves. Owing to the large optical numerical aperture and correction from aberrations, the concave gratings in the Steller Net spectrophotometer provides much better light collection efficiency and signal to noise ratio ~60%. Measurements are made by placing a reference in the sample holder, which is measured to standardize the instrument. The beam is then blocked to record the dark. The reference value is subtracted from subsequent sample measurements to remove the effects of the solvent and the cell.

3.3.1 Transmission measurement of solid samples

To measure the transmittance, total reflectance and diffuse reflectance of reflectors and LSC/PLSC waveguide an integrating sphere was used in combination with the UV-VIS setup. The optical design of the integrating sphere can be seen in Figure 3.4. The integrating sphere has three ports for entrance, sample, and detector. Baffles block the incident light from directly going into the detector and are critical to the sphere performance for characterizing diffuse samples. The function of the integrating sphere is to spatially integrate the radiant flux. The transmittance sample holder is placed at the entrance port of the integrating sphere and that is useful to measure samples that scatter light as all the light is collected by the integrating sphere. For reflectance measurements the sample is mounted in the rear end of the integrating sphere, diffuse reflectance is measured by placing a light trap at the specular reflectance angle.

3.4 Scanning electron microscopy

The size and shape dispersion of MNPs was analyzed using a Scanning Electron Microscope (SEM). SEM uses a beam of high energy electrons that are generated by an electron gun, focused by magnetic lenses onto a specimen. The layout of an SEM and the SEM model used in this work (Carl Zeiss Ultra plus) can be seen in Figure 3.5a, b respectively.

The beam is raster scanned across the specimen surface. The electrons in an

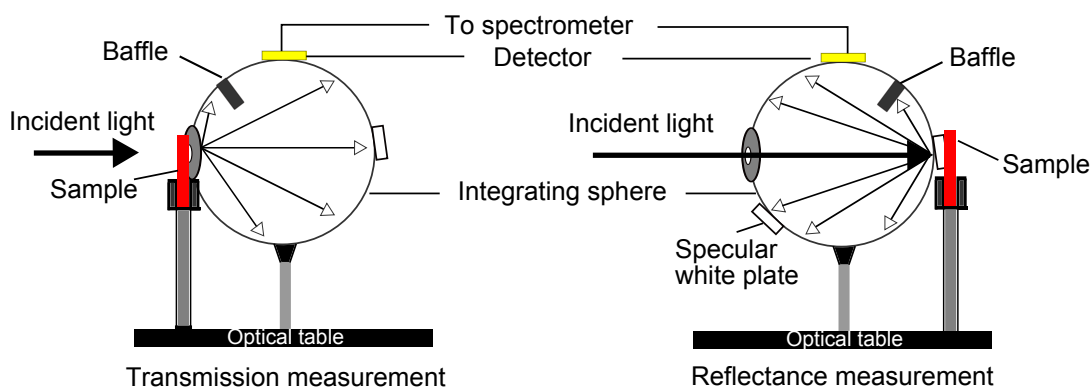


Figure 3.4: Schematic of an integrating sphere showing different sample placement for transmission and total reflectance measurement of solid samples.

SEM never form a real image of the sample unlike the optical microscope, they form an electronic image. It is due to the beam probe scanning the sample with the strength of the signal generated from each point, arising from the topographical or compositional difference in the sample. The SEM image is made of lines of image points, with each point being the size of the probe or the beam spot at the sample surface. A smaller spot size gives better detail of the sample but if it is too small in relation to the area being imaged, it spends very little time on each image point to form a good image. Metals with a high atomic number produce a high yield of electrons and achieve higher useful magnification than low atomic number samples.

Accelerating voltage is the difference in the voltage between the filament and the anode which accelerates the electron beam. For the SEM used the acceleration voltage range was from 0.1 kV to 30 kV. An increase in the acceleration voltage results in a higher signal in the image as greater is the power of penetration by the beam into the sample. This also has a disadvantage of increased heating and the possibility of specimen damage and a reduction in structural details of the sample surface. The MNPs studied in this work had dimensions lower than 50 nm, it was important to get a high-resolution topographical image without damaging the MNPs, a compromise was found by using an accelerating voltage of 3-5 kV to study the samples in this work.

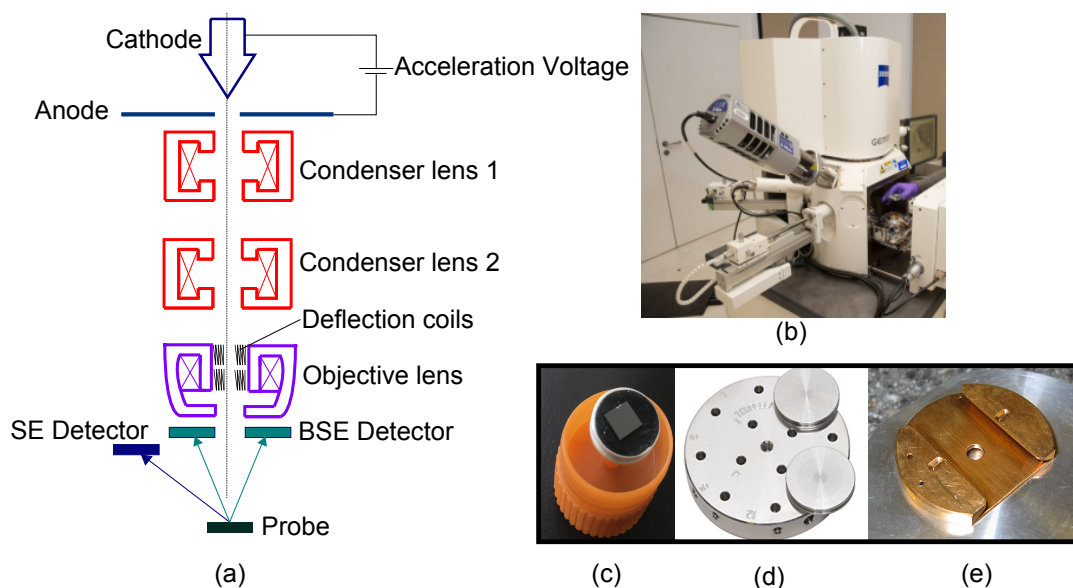


Figure 3.5: a) Simplified schematic of an SEM showing the main components: electron gun, condenser lens, objective lens, and scanning/deflection coils, b) Photograph of Carl Zeiss Ultra Plus with a Gemini column (CRANN, TCD) used in this work, c) 1 cm×1cm silicon wafer stuck to a 0.5 inch diameter aluminum stub via a carbon tab, d) Sample holder used in this work to place the aluminum stubs, e) A dovetail basic unit to hold the sample holder inside the sample chamber.

The SEM was equipped with an In lens detector. The In-lens also called the “Through the lens” TTL detector was mainly used because it gives a shadow-free image with ultra-high topographical resolution. This lens captures the secondary electrons that are produced due to the interactions of the electrons in the incident beam with the specimen atoms. These electrons are produced in close proximity to the incident beam and represent a high lateral resolution signal.

The steps followed for sample preparation are as follows: A silicon wafer was laser cut into 0.5 cm×0.5 cm size, each piece was cleaned in acetone and isopropanol. MNP solution was diluted by a 1:10 dilution factor to avoid MNP aggregation on the silicon wafer. 20µl of the diluted MNP solution was dropped onto the silicon wafer placed on top of the hot plate set at 60°C. After the solution dried up the silicon wafer was ready for imaging. The wafer was placed on an aluminum stub with the help of carbon tape, the stub then is placed on a sample holder designed for use in the SEM as shown in Figure 3.5c, d respectively.

3.4.1 Transmission electron microscopy

The shell thickness of Au@Ag NCs and high-resolution images of Au NRs were taken using JEOL 2100 LaB TEM as seen in Figure 3.6. The TEM images in this work were taken with the assistance of Dr. Eoin McCarthy from AML, CRANN. Both SEM and TEM share similar main components such as an electron source, electron apertures, and electromagnetic lenses. However, TEM uses the electrons that are passed through the sample, unlike SEM that detects scattered electrons from the sample surface. TEM can provide useful information about the inner structure of the sample, morphology. The acceleration voltage can be varied from 60-300 kV. In TEM the sample is placed in the middle of the column, the transmitted electrons pass through the sample through a series of lenses and the image is directly shown on a fluorescent screen. The most common generated TEM image is a bright-field image, it appears as a shadow of the sample. The objective aperture is used to select the unscattered electron beam, this aperture gives an enhanced contrast in the image. Lacey carbon films with 300 mesh grids on a copper TEM grid was used for imaging the samples in this work. The MNPs were dispersed onto the film without dilution. 6 μ l of MNP solution was added to the grid placed on a Whatman filter paper, the grid is shown in Figure 3.6.

3.5 Inductively coupled plasma-mass spectrometry

Inductively Coupled Plasma-Mass Spectrometry (ICP-MS) was used to measure the Au and Ag ion content in Au NRs and Au@Ag NCs. The working principle of ICP-MS is depicted in Figure 3.7a, samples are introduced into an argon plasma in the form of aerosol droplets. The plasma then dissociates the molecules and forms single charged ions by removing an electron. These single charge ions are directed to a mass spectrometer. Most commercial ICP-MS use a quadrupole mass spectrometer for rapid scanning of mass range. At a given time only one mass to charge ratio is allowed to pass through the mass spectrometer. After exiting the mass spec-

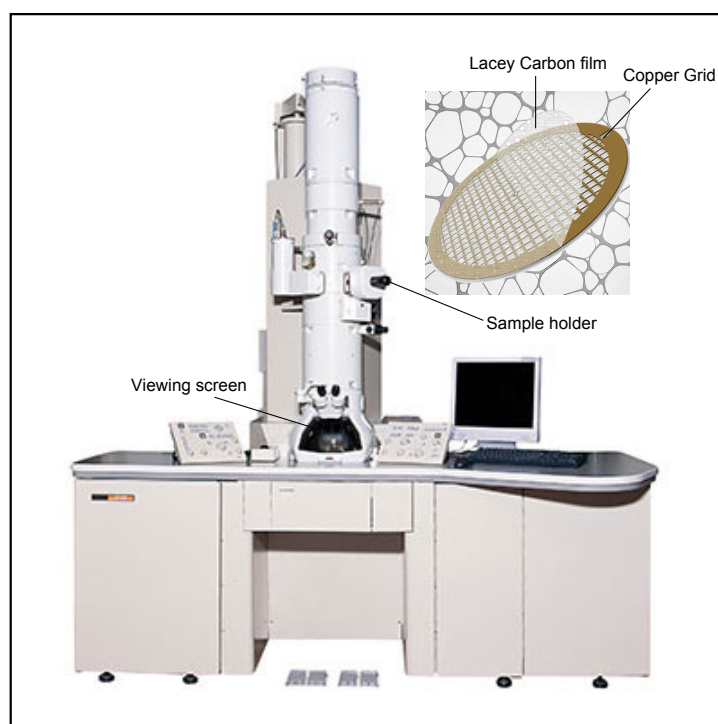


Figure 3.6: Photograph of JEOL 2100 LaB TEM used in this work, (inset) schematic of lacy carbon film on 300 mesh copper grid used for the imaging of MNPs.

trometer the ions strike the detector that counts the individual ions. The software compares the intensities of the measured pulses to the standard to determine the concentration of the element. For each element measured it is necessary to measure just one isotope. For $_{79}\text{Au}$ there is one stable isotope ^{197}Au , for naturally occurring $_{47}\text{Ag}$ there are two stable isotopes ^{107}Ag and ^{109}Ag , ^{107}Ag being the more abundant one.

The liquid samples are typically digested and are then constituted in an aqueous solution to stabilize the elements as an ionic solution. The MNPs in this work were diluted by a factor of 1000 and then digested using 2% nitric acid. A tuning solution is used before the analysis of the samples. The essence of a tuning solution is to make sure that the system gives the maximum signal possible for the analyte. The tuning solution was used before running the samples comprised of various analytes (In, Be, Co, Mn, Th, Ba, Ce, Pb) in a nitric acid matrix. Internal standards can improve the accuracy of the analytical data as it provides a reference

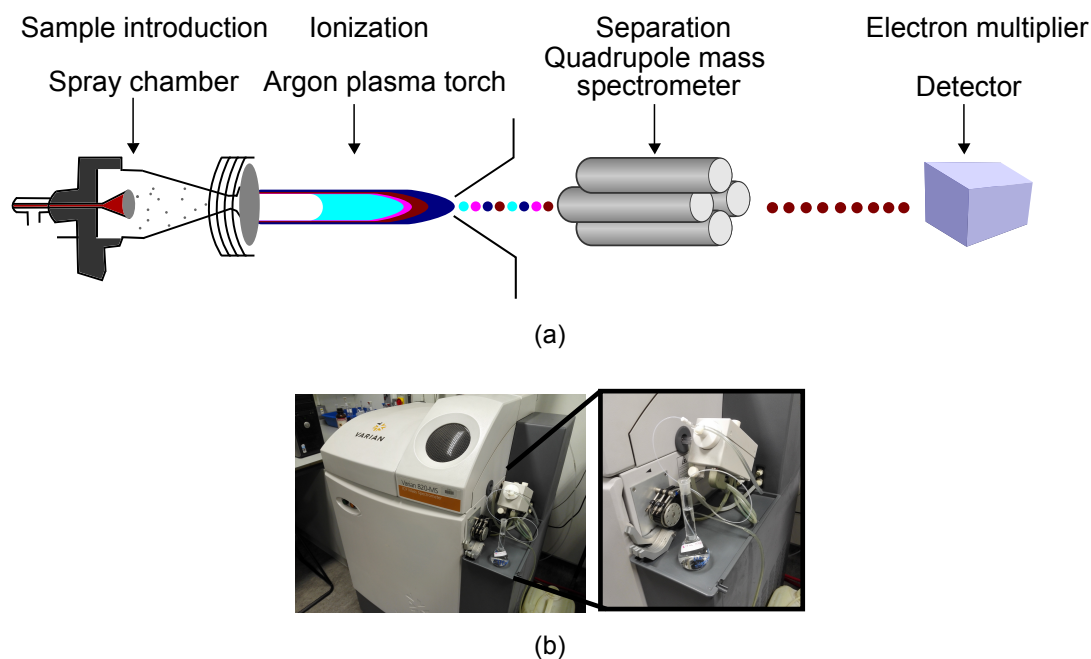


Figure 3.7: a) Simplified schematic of an ICP-MS to understand its working principle, the major components being spray chamber, plasma torch, quadrupole mass spectrometer and detector, b) Photograph of the Varian ICP-MS used in this work and the sample introduction into the chamber.

that can correct the variation between the calibration standard and the samples. Indium is not present in any of the samples that needed to be studied, it was added in equal concentration to all the analytical solutions (blank, calibration standards and samples). The ICP-MS used in this work was Varian 820 as seen in Figure 3.7b. The results from ICP-MS about the concentration of the metal ions could help in determining the concentration of the MNPs in a device.

3.6 Fluorescence spectroscopy

For QDs and dyes, the fluorescence lifetime is of the order 10^{-5} . The fluorescence spectra of fluorophores in solvent were measured using the Horiba Fluoromax4. The xenon lamp is used as the light source and the detector is a photomultiplier tube. The instrument has a wavelength range of 330-950 nm. The fluorescence was measured at 90° angle relative to the excitation light to avoid any interference between the excitation and emitted light as can be seen in Figure 3.8. The excitation

wavelength can be determined from the absorption spectra of the fluorophore and holding the excitation wavelength fixed the fluorescence spectra can be obtained.

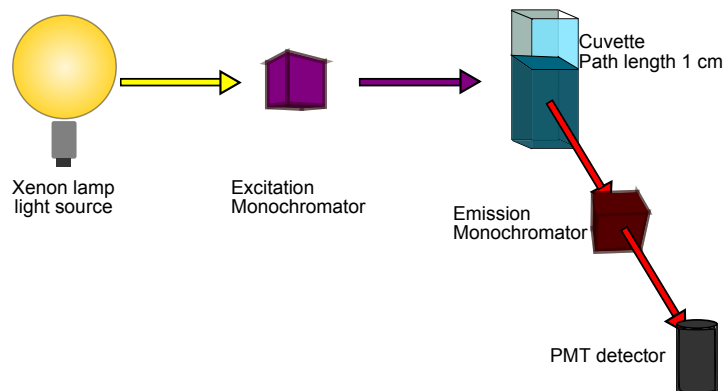


Figure 3.8: Schematic of the measurement of fluorescence in a right angle geometry

3.6.1 Photo luminescent quantum yield measurement of solid samples

Traditionally the PLQY of liquid samples was measured in comparison to a reference sample with known quantum yield. However, for a solid sample, the fluorescence is not emitted uniformly due to waveguiding or scattering. Absolute PLQY measurements are done for the solid-state samples to overcome these problems and avoid the use of a standard sample with known PLQY. The PLQY of Lumogen dyes is known for PMMA (Wilson and Richards, 2009) but the host matrix used in this work is silicone, therefore, it was important to measure the PLQY of the dyes and QDs in this polymer. PLQY was measured by using an integrating sphere along with the Fluoromax. The integrating sphere had a hollow sphere 10 cm in diameter made from solid diffuse reflecting material that has reflectivity more than 99% in the range of 350-1300 nm (*Optical-grade Spectralon material SRM-990 datasheet*). The entrance and exit ports of the integrating sphere are 20 mm in diameter. Solid-state samples of size 11 mm in diameter can be placed in the sample holder mounted at the center of the integrating sphere as shown in Figure 3.9b.

PLQY is the ratio of the number of photons emitted to the number of photons

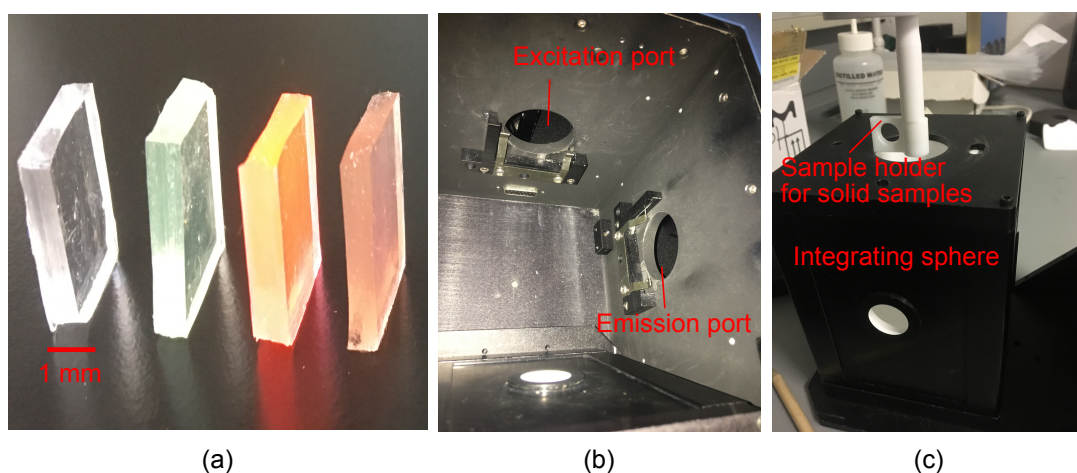


Figure 3.9: Photograph of a) blank, Lumogen dyes and QD samples for PLQY measurement, b) Fluoromax with holders for filters and the ports of excitation and emission monochromators, c) integrating sphere with the sample holder for $1 \times 1 \times 0.1 \text{ cm}^3$ samples.

absorbed. The number of photons absorbed is calculated by measuring the scattered excitation peak first with the blank reference in the sphere L_a and then with the sample containing the fluorophore (L_c). The number of emitted photons are directly calculated from the acquired emission spectrum (E_c). The PLQY can be calculated by the following equation:

$$PLQY = \frac{E_c - E_a}{L_a - L_c} \quad (3.3)$$

where, E_a is the fluorescence of the blank in the integrating sphere.

For fluorophores that have overlap in the absorption and emission spectrum such as the dyes used in this work the emitted light can be reabsorbed by the sample due to multiple reflections inside the sphere. The self-absorption can change the observed spectral shape and the PLQY from the correct values (Ahn et al., 2007). Two different kinds of self-absorption can occur:

- The emitted photons trapped in the integrating sphere can pass through the sample multiple times thus the probability of them being reabsorbed by another dye molecule increases. this process dominates for samples with a low

concentration of fluorophores.

- The photons emitted by a dye molecule are reabsorbed within the dye molecule before they have left the sample. This process dominates for highly concentrated samples.

Self-absorption was accounted for by following the procedure as given in (Ahn et al., 2007). The self-absorption parameter a was found out by taking the emission spectra of a dilute sample that is not affected by re-absorption.

$$a = 1 - \frac{\sum F_{obs}(\lambda)(d\lambda)}{\sum F'(\lambda)(d\lambda)} \quad (3.4)$$

where $F_{obs}(\lambda)$ is the observed emission spectrum and $F'(\lambda)$ is the scaled molecular emission spectrum.

The corrected $PLQY_{cor}$ can be found out by:

$$PLQY_{cor} = \frac{PLQY_{obs}}{1 - a + a \cdot PLQY_{obs}} \quad (3.5)$$

The samples fabricated for PLQY measurement were $1 \times 1 \times 0.1 \text{ cm}^3$ in size as shown in Figure 3.9a. They were cut from a bigger fabricated sample due to the ease in handling silicone.

3.7 Device fabrication

Silicone encapsulant polymer (EI 1184) was used in this work as the host matrix. This polymer will be referred to as Silicone in this work. Silicone belongs to a group of polymers known as PDMS and it is commonly used as an encapsulant layer for PV cells (Oliveira et al., 2019). The transmittance of the polymer in comparison to PMMA (Carl Roth, Germany) can be seen in Figure 3.10a. Silicone offers a higher transmittance in the UV region than PMMA. The elongation of silicone is 25% as compared to 2.5 % for PMMA. It is a two-part polymer that is mixed in a 1:1 ratio to give a viscous liquid. The specific gravity is 1.04 and has a cure time of 4 hours

at 25°C.

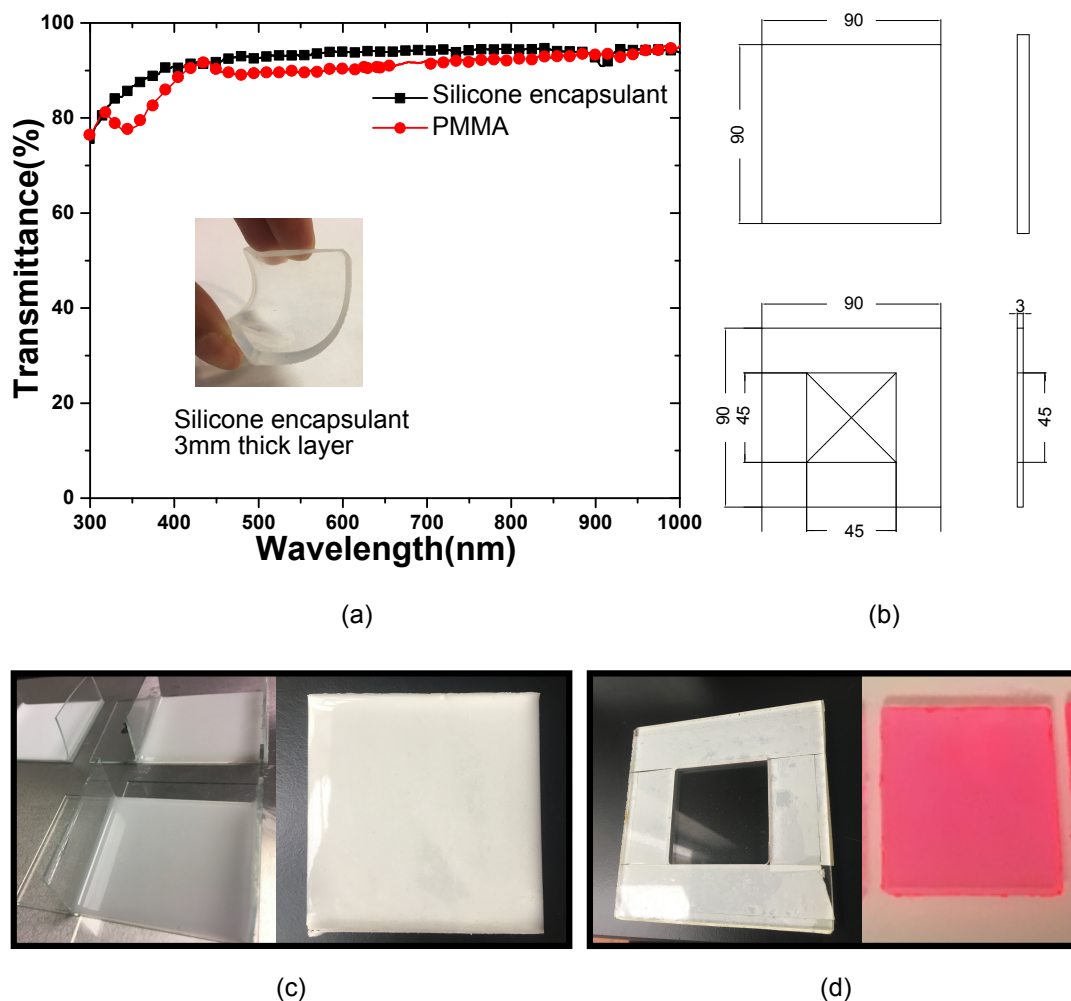


Figure 3.10: a) Transmission spectra of silicone and PMMA (inset) 3 mm thick silicone layer, b) Drawing of the design of the mold used in the fabrication of waveguides, c) Photograph of the diffuse reflector fabricated by drop-casting on a glass plate, d) Photograph of the mold used for waveguide casting and a Red305 dye LSC waveguide.

The LSC/PLSC waveguides were cured in a mold, designed using 3 mm thick perspex sheets, the design can be seen in Figure 3.10b. If fluorophores needed to be incorporated into the final product, the required concentration of fluorophore solution was dissolved in part A of the silicone polymer. The lower viscosity helped the fluorophore to dissolve easily by stirring the mixture on a hot plate at 40°C. The part B of the polymer is added only after all the solvent had evaporated from part A. The mixture was then cast into the mold, for the removal of air bubbles the mold

was put in an oven (Thermo Scientific) at room temperature and was degassed at 15 in.-Hg. After removing the air bubbles the oven is set to 50°C and the polymer was cured for 2-8 hours depending on the thickness of the layer, for example, reflectors fabricated were 1 mm in thickness and needed to be cured only for 2-3 hours.

For diffuse reflectors TiO₂ nanoparticles were embedded into Silicone. The method to fabricate the reflectors was similar to the concentrator waveguides, but instead of casting them in a mold they were drop cast onto a glass slide. Reflectors of 1 mm thickness were fabricated as can be seen in Figure 3.10c along with the fabricated LSC waveguide. 50 x 3 mm c-Si solar cells were attached to one edge of the waveguide by using a conductive adhesive with acrylic resin base and connecting wires were soldered to the PV cell to have the device ready for testing.

3.8 LSC/PLSC characterization

Optical characterization of the LSC/PLSC waveguides was carried out by measuring the emission from the edge of the waveguide and also by measuring the total emission by placing the waveguide inside an integrating sphere. Crystalline silicon solar cells were sourced from SolarCapture (UK) and these cells were attached to one edge of the waveguide to measure the power output from the cell. The electrical characterization was carried out indoors and outdoors in real weather conditions to test the feasibility of the device in temperate weather.

3.8.1 Optical characterization

The setup used to measure the edge emission output from the LSC/PLSC waveguides with and without reflectors can be seen in Figure 3.11. The setup included a standard light source from Ocean Optics equipped with Deuterium and Halogen lamps. A 0.39 numerical aperture optic fiber cable was attached to this light source. A direct beam spot was illuminated at the center of the waveguide, the positioning of the beam was undertaken using an XY stage as it offered a precise control. The size of the beam spot could be changed with the help of the transition

stage. A two-inch integrating sphere (StellarNet) was used to collect the edge emission from the waveguide. The spectrophotometer (StellarNet) used had a detection range from 250-1070 nm and was connected to the output of the integrating sphere by an optic fiber cable. A broad range of integration time 150 ms to 8 s allowed the detection of small signals.

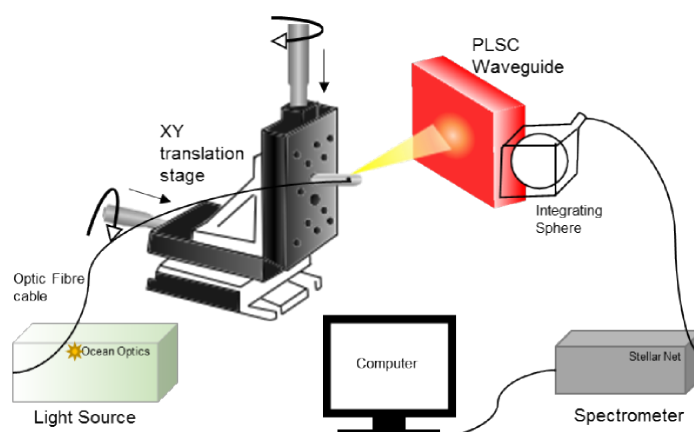


Figure 3.11: Schematic of the edge emission setup used to characterize LSC/PLSC waveguides, main components include the light source, integrating sphere, XY translation stage and a spectrometer.

Measurements that involved the irradiation of the waveguide at a particular excitation wavelength a different light source was used along with a filter as shown in Figure 3.12. The filters were used depending on the particular fluorophore absorption spectrum, however, the basic principle of the setup still remains. To measure the total emission (emission from all the surfaces) of the waveguide the sample was placed in an integrating sphere (Labsphere). The light source used was a halide discharge lamp.

3.8.2 Indoor electrical characterization

Sun 2000 class 'A' solar simulator from Abet technologies was used as a light source to characterize the devices. An approximation of one AM 1.5G sun ($1000\text{W}/\text{m}^2$) is achieved by using a 550 W xenon arc lamp over a $16 \times 16 \text{ cm}^2$ field at a working distance of 20 cm. Access to this solar simulator was provided by Focas, DIT as

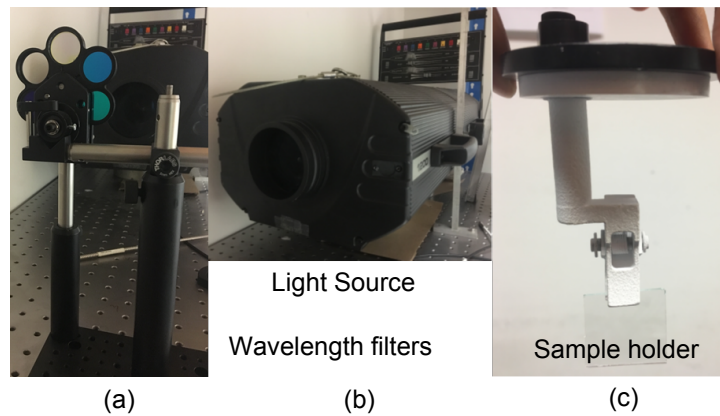


Figure 3.12: Photograph of a) wavelength selective filters, b) halogen light source, c) sample holder for characterizing solid samples.

seen in Figure 3.13. A source measurement unit (SMU) was used to obtain the IV characteristics of the PV cell attached to the LSC/PLSC waveguides. The basic idea of an SMU is that it sources the voltage and measures the current that flows. In that respect, it is like a power supply except that it is programmable and can sweep the voltage in a defined range. The SMU used in this work is Keysight B2900A. Fill factor, short circuit current, open-circuit voltage, maximum power point are automatically calculated by the SMU. The PV cell used in this work had an efficiency of 19% under standard test conditions meant maximum power output of 28.5 mW under AM 1.5G 1000 W/m².

3.8.3 Outdoor electrical characterization

An electrical setup was designed to conduct simultaneous measurement of multiple devices in outdoor conditions. The circuit diagram can be seen in Figure 3.14. A resistor value was selected based on the maximum power output from the device in indoor testing. In order to avoid a high current a shunt with a conversion factor of 20 A-200 mV was connected in series to the device. The current was measured through the shunt and the voltage was measured across the device.

A K type thermocouple was used to measure the temperature of PV cells and LSC/PLSC waveguides as seen in Figure 3.15. A thermocouple is made of two met-

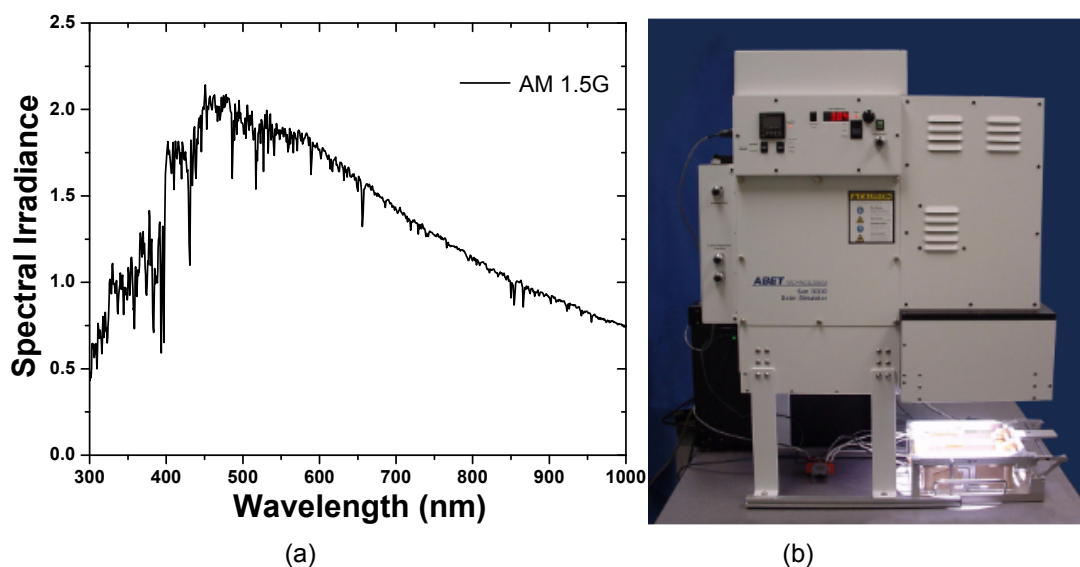


Figure 3.13: a) AM1.5 G spectrum from the Abet solar simulator, b) Photograph of the solar simulator used in this work.

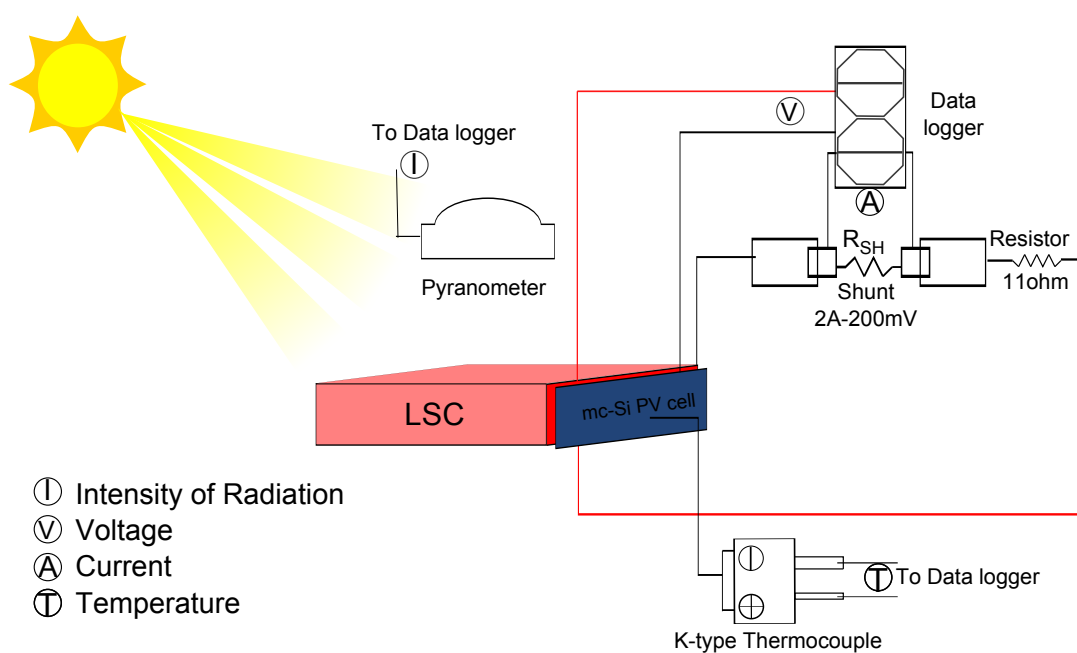


Figure 3.14: Circuit diagram of the outdoor setup to measure the current, voltage and temperature from different devices.

als and when they are fused they create a junction. A change in temperature experienced by the junction creates a very small voltage (millivolts) that corresponds to a temperature reading. The two metals used for K type thermocouple are chromel

(+) and alumel (-). It is the most commonly used general-purpose thermocouple. It had a very wide temperature range from -200°C to $+250^{\circ}\text{C}$ and had good linearity in the range of 0°C to 100°C (*Thermocouple Selection Guide 2019*). The accuracy of the thermocouple used was $\pm 2^{\circ}\text{C}$.

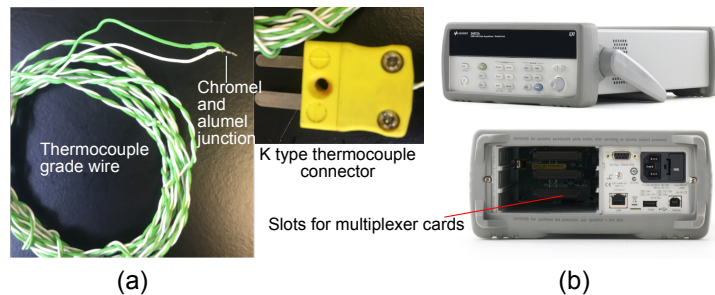


Figure 3.15: Photograph of the K type thermocouple grade wire used in this work, a connector was used to check that the thermocouple was reading the accurate temperature, b) Photograph of the data logger used in this work showing the slots where the multiplexer cards are inserted.

The irradiance was measured using a Kipp and Zonen CMP6 pyranometer as seen in Figure 3.16. The working principle of a pyranometer is based on thermoelectric detection. The incoming radiation is absorbed by a blackened receiver surface over a wide wavelength range. The resultant increase in the temperature is measured by the thermocouples that are connected in series or series-parallel to form a thermopile. The black detector coating is protected from the external environment by a hemispherical dome made of optical quality glass. Depending on the glass the transmission can be from 300 nm to 3000 nm. The pyranometer used in this study had a spectral range of 285 nm to 2800 nm and a response time of 18 s. It was placed horizontally on the roof similar to the setup. The data from the PV cells, shunts, thermocouples were acquired by a data logger (Agilent 3472A LXI) shown in Figure 3.15. Three Agilent 34901A 20 channel multiplexer cards were used for scanning the data. The setup was mounted on the roof of the engineering department in Trinity College as seen in Figure 3.16.

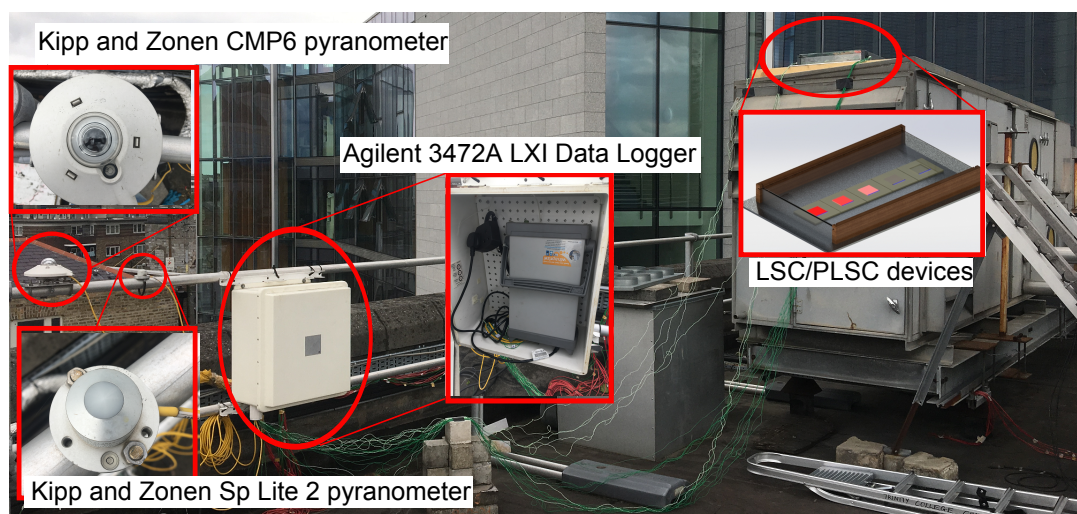


Figure 3.16: Photograph of the roof with focus on the main components and their relative position such as pyranometers, data logger and the device box.

3.9 Conclusions

All the materials used in the fabrication of MNPs and devices are listed in this chapter. The optical properties and size, the shape of the MNPs were characterized with the help of UV-VIS spectrometry and SEM/TEM respectively. ICP-MS helped determine the number of a certain MNP in aqueous solution. The results of these measurements are presented in chapter 4. Once the stock solution of the MNPs was prepared and was stable in the host matrix the waveguides were constructed.

Silicone polymer is a relatively new choice as a host matrix for application in LSC and it can be highly appropriate because it can be cast into sheet or bulk form. The fluorophores used in this work emit in the visible range and the high transparency of silicone in the visible range makes it most suitable for these fluorophores. The absolute PLQY of the fluorophores in silicone was measured by using the integrating sphere. $4.5 \times 4.5 \times 0.3 \text{ mm}^3$ size LSC/PLSC waveguides were fabricated by using a perspex mold, and the polymerization was carried out in an oven after removing all the air bubbles from the polymer. c-Si PV cells were attached to one edge of the waveguides by an adhesive and connections were made by soldering connecting wires to the PV cell to test the IV characteristics of the de-

vice. The fabricated waveguides incorporating either fluorophores or fluorophores and MNPs are characterized and the results are presented in chapter 5.

The design and assembly of the setup to measure the edge emission from the waveguides have been presented. The total emission (emission from all the surfaces) from the waveguide was measured using an integrating sphere. The relative power output and device efficiency were measured indoor using a solar simulator. it is important to test the devices in diffuse light therefore, a setup was designed on the roof of Trinity College to simultaneously test the relative power output from the devices. The results from the outdoor characterization are presented in chapter 5 and 6.

Chapter 4

Fabrication of metal nanoparticle-host matrix nanocomposite

This chapter is divided into three core parts, the first part focuses on the synthesis and purification of gold nanorods (Au NRs) and gold core silver shell nanocuboids (Au@Ag NCs). The optical and structural properties of the synthesized MNPs is studied. The correlation between the optical spectra of the MNPs and the removal of by-products from the as-synthesized solution is established. The importance and optimization of the purification process of synthesized MNPs are presented. The second part of the chapters deals with the quantification of MNPs in a solvent. The surface functionalization of the purified anisotropic MNPs was carried out. An optimized, reproducible recipe was achieved for an efficient phase transfer from aqueous solution to dichloromethane (DCM). The key parameters to achieve a reproducible recipe to prepare the stock solution of MNPs is presented. The final part focuses on the fabrication and characterization of MNPs in the host matrix. The stability of the MNPs in the polymer is analyzed.

4.1 Synthesis of anisotropic MNPs

As mentioned in section 2.7, MNPs play a key role in plasmonic interactions. More specifically their shape and size control the plasmonic interactions with fluorophores. The SPR wavelength in spherical MNPs spans a very small range (tens of nanometres) on changing the sphere diameter, whereas, anisotropy in shape of the MNP adds another degree of freedom. This addition in degree of freedom allows controlling the SPR wavelength from near UV to mid IR range by simply varying the aspect ratio (length/width) of the MNP. The key requirements from the synthesis process are a high shape and size yield of the desired MNPs in solution, the ability to easily tune the shape and therefore, the optical properties of the MNP. There are a few disadvantages in procuring anisotropic MNPs commercially: a) they are expensive, Au@Ag NCs are not available commercially, b) Au NRs are usually dissolved in a solvent that might not be compatible with the host matrix used in LSC devices, c) synthesizing the MNPs enables a precise control over the SPR peak that can be tuned to the fluorophores absorption and emission spectra, only specific SPR wavelengths are widely available for Au NRs. To utilize the plasmonic properties of Ag, Ag NRs were synthesized, but due to many challenges (see Appendix A) the focus was shifted to Au NRs and higher aspect ratio Au NRs were further utilized to synthesize Au@Ag NCs to exploit the plasmonic properties of Au and Ag, respectively. Recipes from the literature were used to synthesize the MNPs but they needed to be attuned for the lab to achieve repeatable results.

4.1.1 Synthesis of gold nanorods

The seed-mediated approach was used to synthesize Au NRs, as it is a well-established technique, a few changes were made to the recipe to optimize it according to our lab environment. Au seeds were prepared by reduction of gold precursor and using CTAB as the capping agent (Scarabelli et al., 2015).

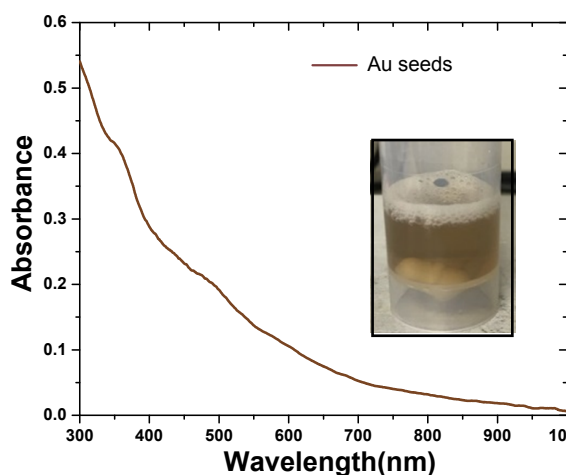


Figure 4.1: UV-VIS spectra of CTAB capped Au seeds.

The synthesis was performed at 30°C. For seeds, 25 µl of 50 mM HAuCl₄ solution was added to 4.7 ml of 0.1 M CTAB. The solution was stirred at a slow speed (300 rpm) until the gold salt was completely dissolved in CTAB. 600 µl of 10 mM ice-cold NaBH₄ solution was added into the solution instantaneously while stirring the solution at a high speed of 1300 rpm, resulting in Au seeds Figure

4.1. It was found that if the reducing agent NaBH₄ was not added to the seed solution instantaneously the resultant solution comprised of gold nanospheres instead of gold seeds.

For the growth solution, the Au NRs were prepared using CTAB capped Au seeds (Nikoobakht and El-Sayed, 2003). 100 µl of 50 mM HAuCl₄ was added to 10 ml of 0.1 M CTAB. The solution was shaken and kept in the water bath set at 30°C for 20 minutes, shaking the solution at intervals. After that, 75 µl of 0.1 M ascorbic acid was added to the solution and gently shaken. AgNO₃ was added to the growth solution. Finally, 120 µl of the seed solution was added to initiate the reduction of the gold salt. The solution was kept undisturbed in the water bath for half an hour to complete the NR formation. The optical extinction spectra of the as-synthesized Au NRs can be seen in Figure 4.2a.

The optical spectra indicate that the MNPs have a rod shape as is evident by the two peaks. The transverse peak is at ~510 nm. The longitudinal peak red-shifts on increasing the amount of AgNO₃ in the growth solution. This is due to the increase in the aspect ratio (length/width) of the nanorods. The longitudinal plasmon band peak shifted from ~704 nm for Au NR sample 1 to ~800 nm for Au NR sample 2. Increase in the ratio of silver to gold ion in the growth solution increased the aspect

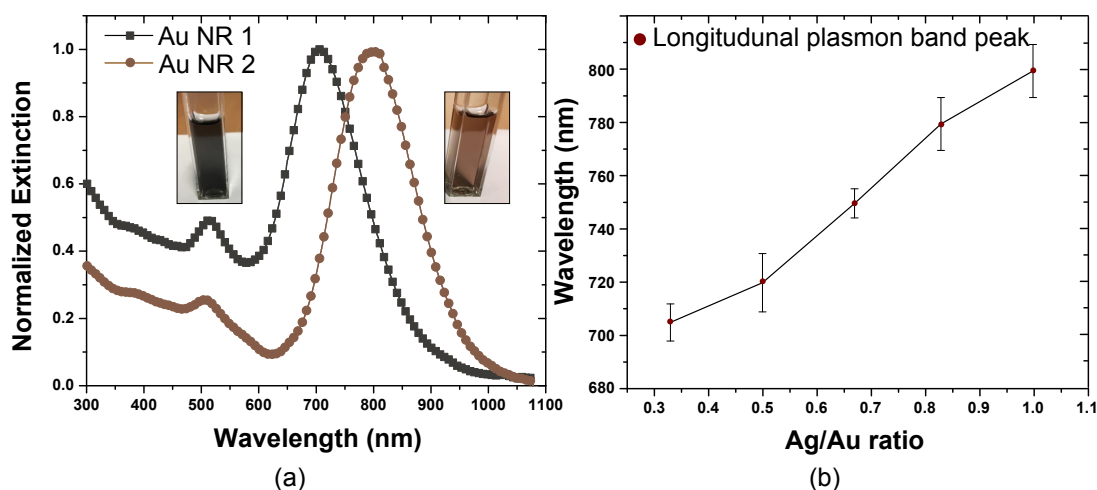


Figure 4.2: a) UV-VIS spectra of two CTAB capped Au NR samples with different aspect ratios, b) Position of the longitudinal plasmon band peak with change in silver to gold ratio in the growth solution.

ratio of the NRs as is evident by Figure 4.2b. The synthesis for the different aspect ratio Au NRs was carried out three times to obtain the error bar that represents the change in the longitudinal peak position.

Full width half maximum (FWHM) and the shape of the longitudinal band can give information about the size dispersion of the nanorods. A narrow FWHM and symmetry of the longitudinal band show that the size dispersion in the sample is reduced and it can be confirmed by electron microscopy imaging. In Au NR sample 1 the longitudinal band is not as symmetric as for Au NR sample 2. The high intensity ratio between the transverse and longitudinal band peak and the absence of a shoulder in the transverse peak is an indication of fewer by-products in the solutions.

4.1.2 Synthesis of gold core silver shell nanocuboids

Au NR sample 2 was used to synthesize the Au@Ag NCs. The first centrifugation step of the Au NRs sample 2 was carried out at 12,000g centrifugal force for 30 minutes to remove excess CTAB and subsequently the pellet was re-dispersed in a 0.08 M CTAC solution at the same volume. The second centrifugation step at a lower centrifugal force (4,000g) had two main purposes; i) to remove by-products

formed during synthesis, (ii) to ensure a good surfactant exchange from CTAB to CTAC. The recipe used to synthesize Au@Ag NCs is a slight modification of previously published work (Jiang et al., 2012b). Five bottles each of 2 ml Au NR sample 2's supernatant solution were prepared and 0.04, 0.12, 0.24, 0.4, 0.56 ml of 0.01 M AgNO_3 solution was subsequently added to each bottle. Lastly, 0.1 M AA solution was added to each solution. The volume of the AA solution was half the volume of the AgNO_3 solution. The resultant solutions were kept in an oven set at 60°C for 4.5 hours. An immediate change in color was observed after half an hour. The vivid color change after 4.5 hours can be seen in Figure 4.3b.

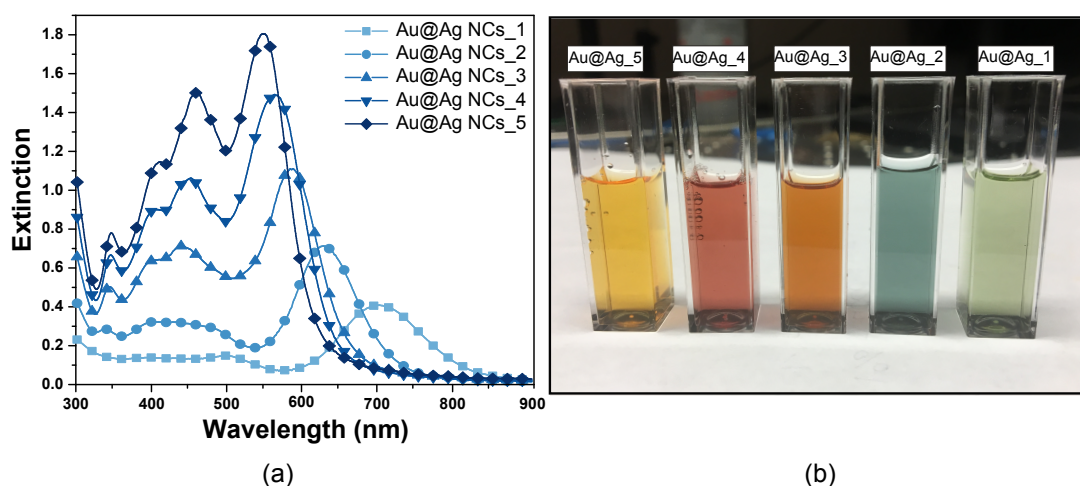


Figure 4.3: a) UV-VIS spectra of five CTAC capped Au@Ag NC samples with different silver shell thickness, b) Photograph of as-synthesized Au@Ag NC samples.

Optical extinction spectra of as-prepared Au@Ag NRs obtained by UV-VIS spectrophotometer as shown in Figure 4.3a. The extinction spectra of Au@Ag NRs have four plasmon bands, the peaks can be labeled as 1-4 from high to low wavelengths respectively. These plasmon bands become stronger with an increase in the amount of Ag in the growth solution. The dilution caused by the AA and AgNO_3 solution has been corrected for the optical spectra of the Au@Ag NCs. Peak 1 which is the longitudinal plasmon band of the Au@Ag NCs blue-shifted from ~ 707 nm for sample 1 to ~ 552 nm for sample 5. This blue shift is not only due to the decrease in the aspect ratio of the nanorods but also because of the increasing effect of Ag in the

optical properties. The plasmon resonance wavelength due to Ag is shorter than Au because the interband transition of Au is at a longer wavelength. Peak 2 at ~503 nm initially blue shifts then redshifts to ~461 nm when the AgNO₃ volume is 0.24 ml. Further increase in the AgNO₃ volume increases the intensity of the transverse peak such that the longitudinal and transverse are of comparable intensities. Peak 3 and 4 become prominent when AgNO₃ volume reaches 0.24 ml in the solution. The appearance of these peaks indicates that the plasmonic properties of the silver shell screen the effect of gold on the plasmon bands (Jiang et al., 2012b). The peak 1 has a higher extinction intensity, therefore, it is possible that the formation of by-products (cubes) is lesser. The wavelength range from 350 nm to 600 nm can be utilized by changing the precursor concentration in the final solution, thus, making Au@Ag NCs attractive MNPs for PLSCs.

4.1.3 Reproducibility of Au NRs and Au@Ag NCs synthesis

Reproducibility of the synthesis is important because good control over the aspect ratio of the NRs/NCs enables better spectral matching of the fluorophore and the MNP for PLSC. To ensure reproducibility of the MNPs with minimum deviation from the desired aspect ratio and shape yield, it was of importance to follow certain steps listed below:

- The glassware used for the synthesis should ideally be thoroughly cleaned with Aqua Regia to avoid the presence of trace impurities that can affect the synthesis. For this purpose, the glassware was first rinsed with acetone because acetone being a polar solvent dissolves almost all organic compounds (CTAB, CTAC) and then isopropanol to remove the acetone. In the end, the glassware was thoroughly rinsed a couple of times with deionized (DI) water.
- Silver precursor should be measured using a non-metallic spatula, as these salts react readily with metals.
- Impurities present in CTAB such as iodine can inhibit the growth of nanorods

(Smith, Miller, and Korgel, 2009). The CTAB purchased from Sigma Aldrich was devoid of high impurity levels thus enabling the formation of nanorods.

- CTAB crystallizes below 20°C and needs a higher temperature to completely dissolve in water. CTAB solution was ultrasonicated for three minutes and kept in the water bath for an hour to completely dissolve it.
- NaBH₄ was freshly prepared for every synthesis. An ice bath was used to keep the NaBH₄ solution ice-cold, using room temperature NaBH₄ did not result in the formation of seeds.
- The addition of the NaBH₄ to the seed solution should be instantaneous while the seed solution is being stirred at a high speed of 1300 rpm. This step ensures the simultaneous production of all nuclei in the solution volume. The resultant seed solution should be used within two hours of synthesis.
- The growth solution should be at 30°C and kept in the water bath after the addition of all the additives, to facilitate the completion of the reaction.
- For Au@Ag NCs it was observed that the output is highly dependent on the monodispersity of Au NRs used as seeds. A change in the longitudinal plasmon band wavelength of the Au NRs results in a shift of up to ~20 nm in the absorbance peaks of the Au@Ag NCs, with some samples of the NCs having a higher number of by-products. Thus, extra precaution steps were taken when synthesizing the NCs as a mistake in one step lead to a change in the shape and size yield of the NCs.
- It was found that Au@Ag NCs stabilized and stopped growing after 24 hours of removing the as-synthesized solution from the oven as is evident from Figure 4.4. Similarly, Au NRs were stable after 24 hours of synthesis, showing a slight blue shift (~2 nm) of the longitudinal peak Figure 4.4.

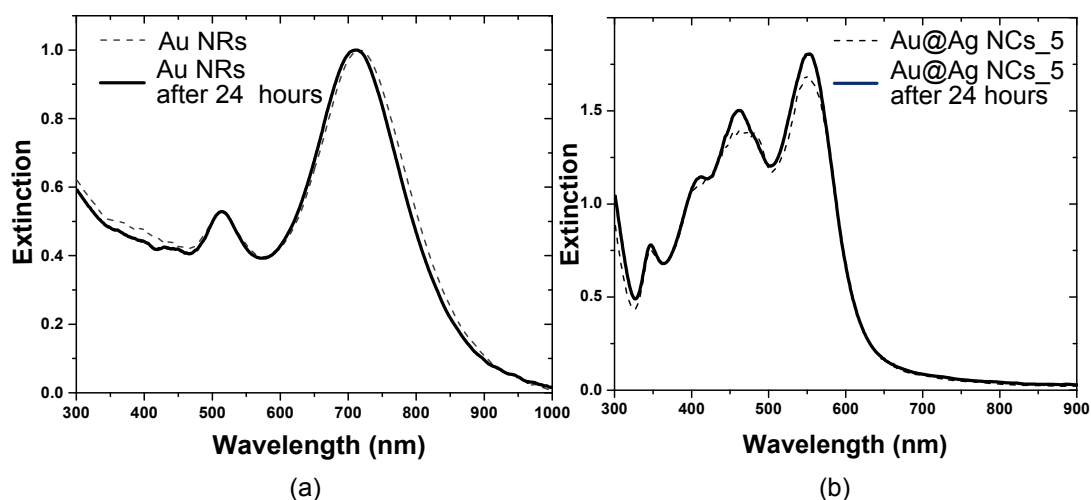


Figure 4.4: UV-VIS spectra of a) Au NRs sample 1 after synthesis and after 24 hours, b) Au@Ag NCs sample 5 immediately after taking out of oven and after 24 hours.

4.2 Purification of anisotropic MNPs

Shape/size yield in the seeded growth mechanism is usually meager and insufficient for the targeted application. By-products can account for 10-90% of as-synthesized solution (Nikoobakht and El-Sayed, 2003, Yu et al., 1997). Spherical and cube nanoparticles are inevitable side-products in the synthesis of Au NRs and Au@Ag NCs, respectively. Post-synthesis purification of as-synthesized colloidal solution can maximize the yield in samples. Partial shape or size separation can lead to the by-products influencing the plasmonic properties of the dispersed MNPs in the host matrix nanocomposite. Centrifugation is commonly used to separate colloidal nanoparticles of different sizes (Akbulut et al., 2012, Sharma, Park, and Srinivasarao, 2009), but the separation of by-products based on shape is advantageous to achieve monodisperse nanoparticles in the host matrix nanocomposites. In the purification process, the main purpose of the first centrifugation step is to remove extra additives such as CTAB/CTAC from the as-synthesized solution. The second centrifugation step is primarily for shape separation.

4.2.1 Purification of gold nanorods

The as-synthesized Au NR solution was centrifuged at high centrifugal force (12,000g) for 30 minutes. It is important to set the temperature of the centrifuge above 25°C to avoid crystallization of CTAB in the centrifuge tube. The pellet from the first centrifugation step was re-dispersed in DI water and centrifuged at a lower force (3,500g for Au NR sample 1) and (2,500g for Au NR sample 2). For Au NR samples, the UV-VIS spectra of the supernatant and pellet solutions after the second round of centrifugation can be seen in Figure 4.5. For both the samples, a red-shift of (5-10 nm) is observed in the longitudinal plasmon band peak of the supernatant solutions with respect to the parent solution. This red-shift indicates the presence of a higher aspect ratio nanorods in the supernatant solution.

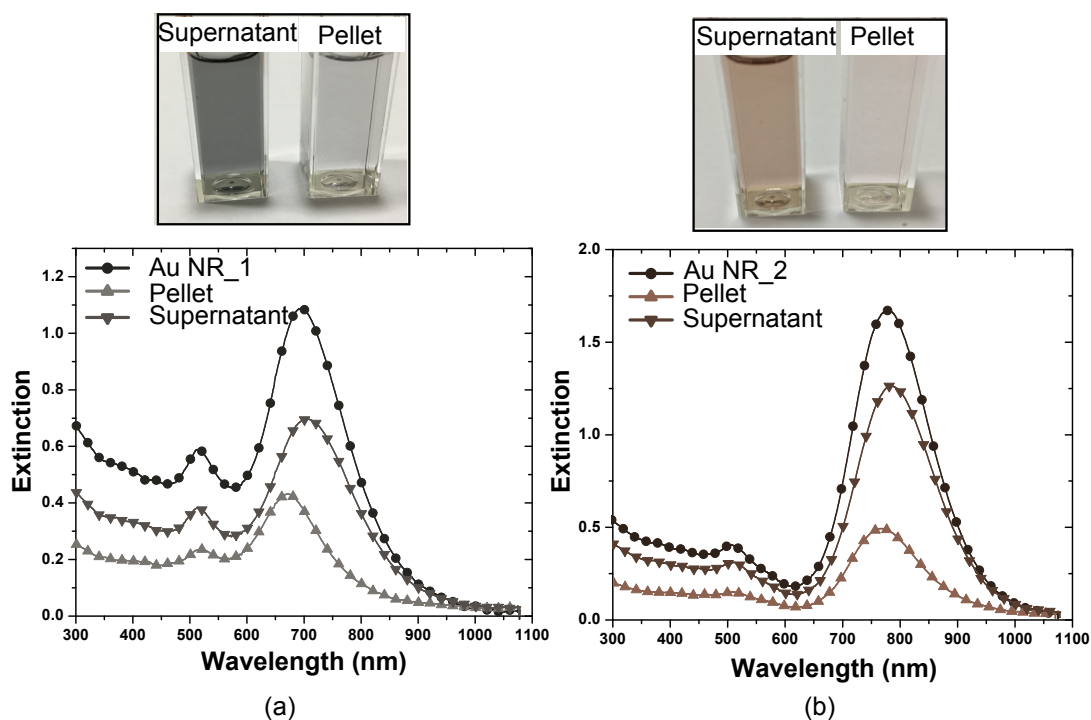


Figure 4.5: UV-VIS spectra of a) Au NRs sample 1, b) Au NRs sample 2 before and after centrifugation

The FWHM of the supernatant longitudinal plasmon band was found to be ~10% smaller than the FWHM of the parent solution. Further confirmation of shape separation is given by taking the UV-VIS spectra of the pellet solutions, Fig-

ure 4.5. An intense blue shift is observed in the longitudinal plasmon band peak of the pellet solutions as compared to the supernatant solution. The blue shift is ~ 36 nm and ~ 20 nm for Au NR samples 1 and 2 respectively.

Thus, the pellet solutions mainly

comprise of smaller aspect ratio nanorods as compared to supernatant solution.

Using the optimized recipe it was also possible to separate the spherical by-products from the parent solution as seen in Figure 4.6. The peak at ~ 510 nm is higher than the longitudinal plasmon band for the pellet solution, Au nanospheres exhibit a plasmon band at ~ 510 nm, this leads to the conclusion

that the pellet solution contains the spherical particles.

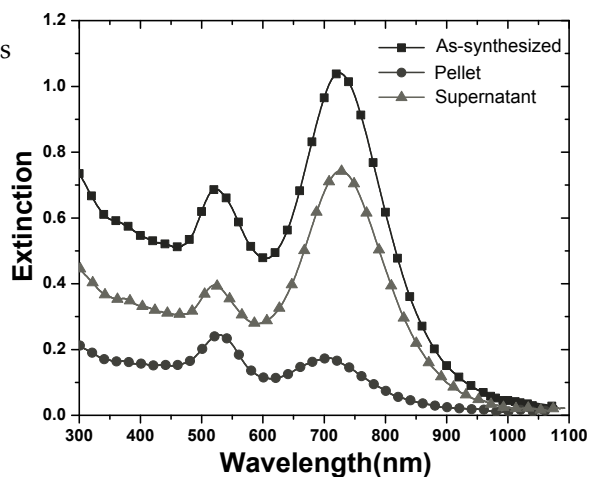


Figure 4.6: UV-VIS spectra of centrifuged Au NRs, indicating the presence of nanospheres in the pellet solution.

4.2.2 Purification of gold core silver shell nanocuboids

Similar to Au NRs, the Au@Ag NCs were centrifuged first at a high centrifugal force of 12,000g for 30 minutes to remove extra CTAC and additives. The pellet was re-dispersed in DI water to make the same volume before centrifugation. Samples 1 and 2 were centrifuged at 4,000g for 15 minutes, whereas samples 3, 4 and 5 were centrifuged at 5,000g for 15 minutes. The UV-VIS spectra of the Au@Ag NC samples before and after centrifugation can be seen in Figure 4.7.

The peak at ~ 347 nm is absent in the spectrum of the supernatant solution for all the samples. The absence of this peak indicates a lack of a thick Ag shell on the Au NRs as silver has a plasmon peak at ~ 365 nm. NCs have a higher aspect ratio due to the absence of the silver shell and are present in the supernatant solution after centrifugation. The ratio of the longitudinal surface plasmon peak to the transverse peak is smaller for the supernatant solution as compared to the

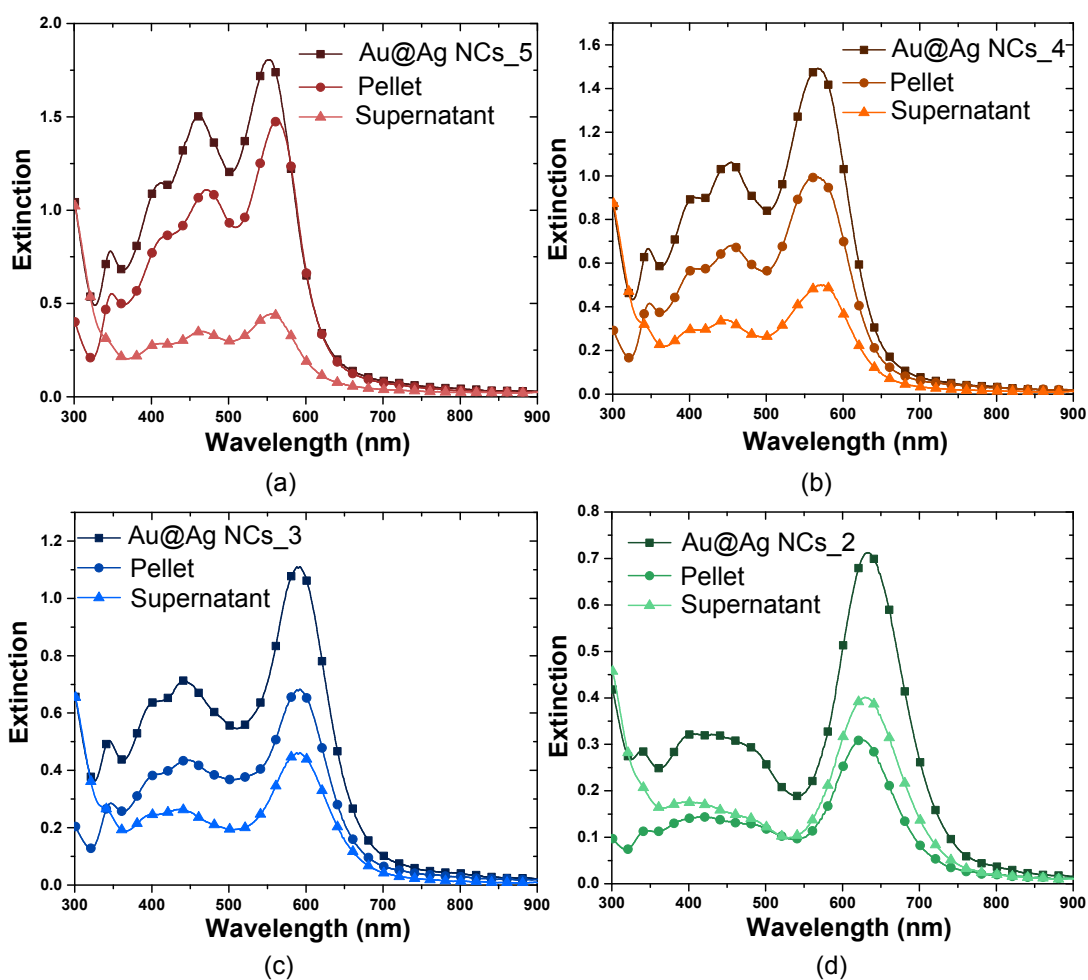


Figure 4.7: UV-VIS spectra of Au@Ag NC samples 5(a), 4(b), 3(c), 2(d) before and after centrifugation.

as-synthesized solution indicating the presence of cube-like structures in the supernatant solution. For sample 2, the volume of AgNO_3 is 0.12 ml, there is a larger ratio of MNPs in the supernatant solution thus indicating MNPs with a higher aspect ratio due to the absence of an Ag shell. This further proves that the plasmonic properties of silver overtake that of gold only after a certain volume (0.12 ml in this case) of AgNO_3 in the growth solution.

4.3 Morphology analysis of anisotropic MNPs

The morphology and size distribution of the supernatant and pellet solution Au NR samples was characterized by using an SEM and TEM. The sample preparation for SEM and TEM has been discussed in section 3.4. The SEM images were taken using the TTL detector to get a better topographical image and the contrast between the Au, Ag and the Si wafer is very good to observe the MNPs. Ideally, the resolution of SEM, in this case, should be 1 nm but vibrations and disturbances (due to another equipment running) in the room where SEM is placed can affect this resolution limit. With the help of TEM higher resolution images could be achieved and could give more insight on the MNPs especially the Au@Ag NCs.

4.3.1 Morphology analysis of gold nanorods

Au NRs sample 1 and 2 were analyzed using an SEM and TEM. The SEM image of both the samples after synthesis can be seen in Figure 4.8a, b respectively. The size distribution of NRs from both the samples can be seen in Figure 4.8e, f. For sample 1 majority of the NRs are ~ 27 nm long giving an aspect ratio of $\sim 2.7 \pm 0.2$. As for Au NR sample 2 majority of NRs are ~ 36 nm in length and have an aspect ratio of 3.6 ± 0.4 . Figure 4.8c,d shows the TEM images of the Au NR 1 and Au NR 2 samples after purification. The NRs have a capsule shape and can be approximated to a cylinder capped with hemispherical ends.

4.3.2 Morphology analysis of gold core silver shell nanocuboids

The morphology of the Au@Ag NC sample 5 was studied using SEM, TEM as previously undertaken for Au NRs. The SEM image of Au@Ag as-prepared sample 5 is shown in Figure 4.9a with cuboid shape. Around 100 NCs were measured to estimate the size yield, majority of the NCs have length between 54-57 nm with an aspect ratio of 1.8 ± 0.2 as can be seen in Figure 4.9c. There are cubes and triangles as by-products of the synthesis. The aspect ratio distribution gives an idea of the shape distribution, as well as AR of 1.2 ± 0.2 indicates the presence of cubes. It is

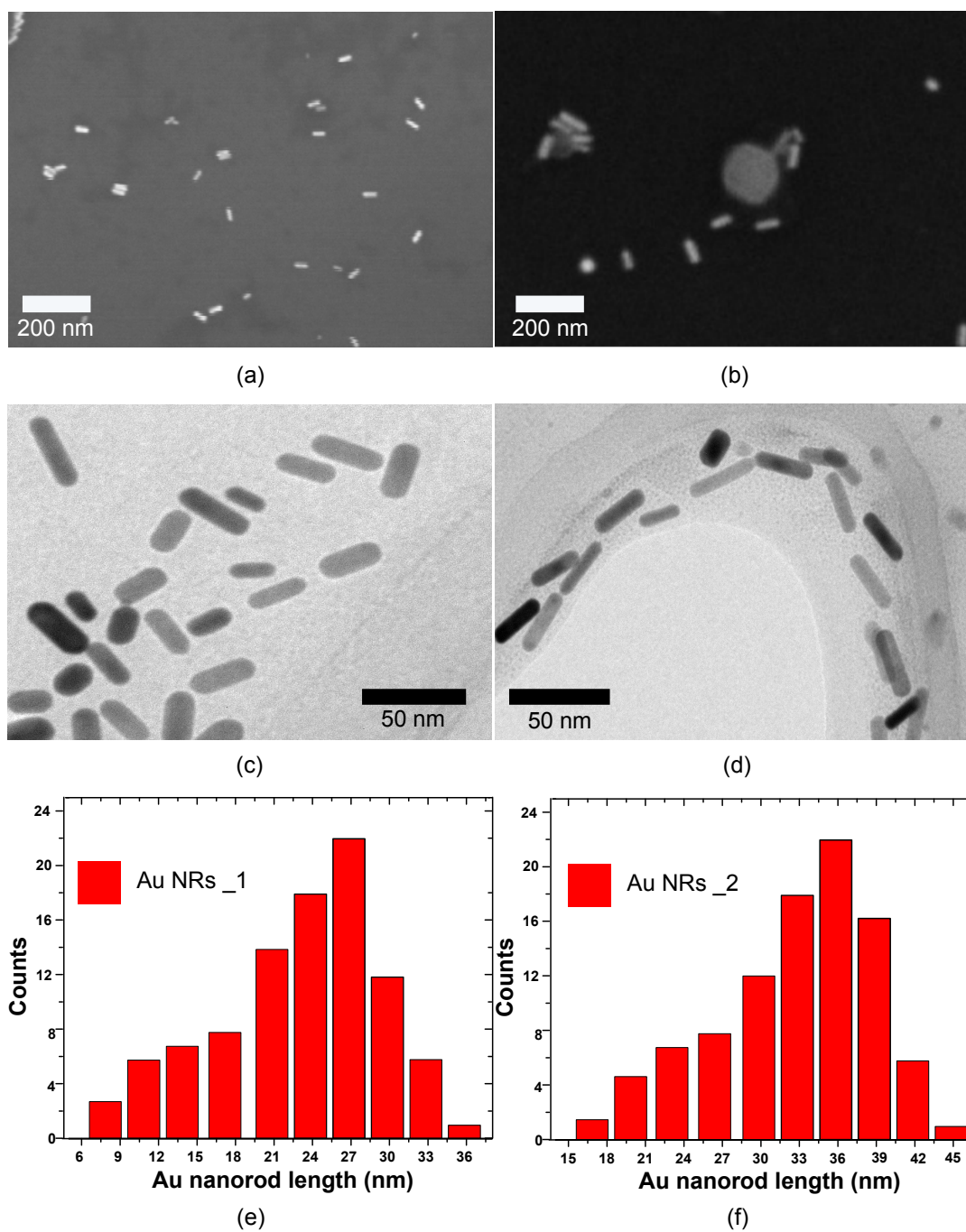


Figure 4.8: a),b) SEM images of Au NRs sample 1 and 2 respectively, c),d) TEM images of Au NR samples 1 and 2 respectively giving an insight about the shape of the NRs, e),f) Size distribution of Au NR samples 1 and 2 respectively.

important to note that there are triangles present in the solution with an average size of ~ 50 nm. Since their size is similar to the cuboid length it is difficult to remove them via centrifugation, but the yield of these nanotriangles is very low

when compared to the cuboids, contrary to the synthesis of Ag NRs (appendix 1 for further details). Therefore, it is important to take electron microscopy images of the sample to assess the shape yield, before the surface functionalization of the MNPs.

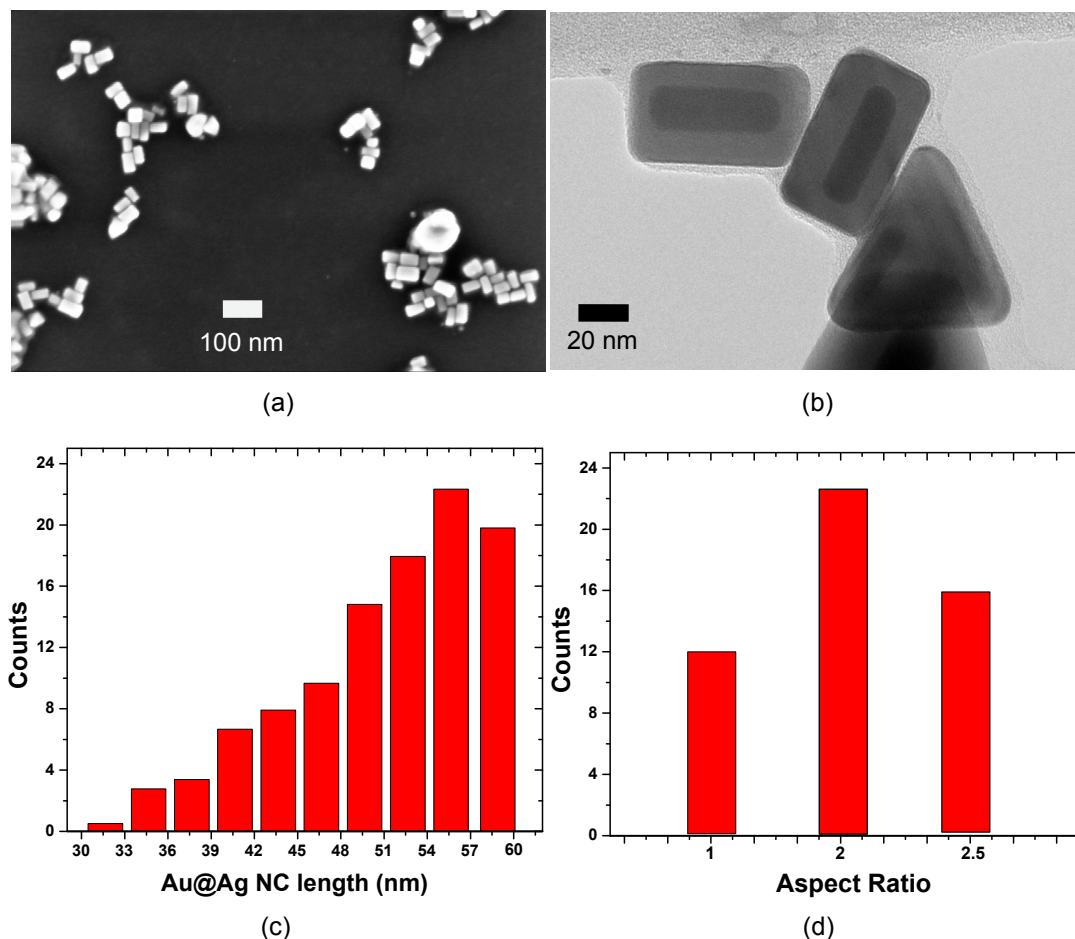


Figure 4.9: a) SEM image of as-synthesized Au@Ag NCs, b) TEM image of purified Au@Ag NCs showing the Ag shell thickness, c) Size distribution of Au@Ag NCs, d) Shape analysis by aspect ratio distribution of Au@Ag NCs.

To get an insight about the Ag shell, TEM images of the pellet solution of the Au@Ag NCs sample 5 after centrifugation were studied as shown in Figure 4.9. The shell thickness was measured at the sides and end, it was thicker in the sides as compared to the ends and that is the reason for the lower aspect ratio of the NCs. The shell was 6 nm and 9 nm on the ends and sides respectively. The Ag shell thickness more than ~5 nm completely screens the plasmonic effect of Au (Jiang

et al., 2012b).

4.4 Concentration of MNPs

The assumption of 100% reduction of the gold or silver precursor is not valid in the synthesis of anisotropic MNPs such as Au NRs and Au@Ag NCs (Gou and Murphy, 2005). It is crucial to determine the quantity of gold/silver that makes up the NRs/NCs to know their concentration in the solution and that can help estimate their number of MNPs in the host matrix. The extinction coefficient found from the UV-VIS spectra of the MNPs can help resolve their concentration (Haiss et al., 2007). However, finding the correct extinction coefficient of anisotropic MNPs can prove challenging due to the low yield of the NRs/NCs in the solution and presence of by-products in the solution. The concentration of the Au and Ag ion in the sample solutions of Au NRs and Au@Ag NCs was found using ICP-MS as described in section 3.5.

With the help of the dimensions of the MNPs, the MNP concentration in sample solution could be calculated by using the following equation:

$$c_{MNP} = \frac{N_{metal}}{(N_{metalperMNP} \cdot V_{sample} \cdot N_A)} \quad (4.1)$$

where N_{metal} is the number of Au or Ag atoms in the total solution, $N_{metalperMNP}$ is the number of Au or Ag atoms per MNP, V_{sample} is the volume of the sample solution, N_A is the Avogadro's constant. It should be noted that for the calculation of the Au NR concentration in the sample solution, a cylindrical form capped with hemisphere on both ends is assumed, whereas for Au@Ag NC a cuboid form is assumed comprising of Au NR 2 as the core of the NC as shown in Figure 4.10.

The volume of a single Au NR and Au@Ag NC is then given by:

$$V_{nanorod} = (\pi \cdot r_{NR}^2 \cdot l_{NR}) + \left(\frac{4}{3} \cdot \pi \cdot r_{NR}^3\right) \quad (4.2)$$

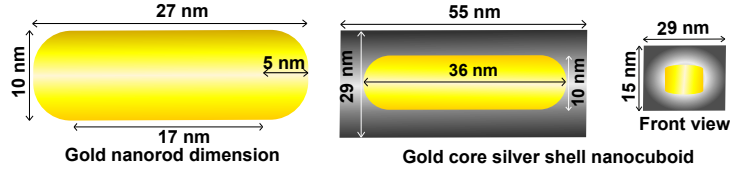


Figure 4.10: Average dimensions of Au NR and Au@Ag NCs based on electron microscopy, used to determine the concentration and surface area of the MNPs.

$$V_{nanocuboid} = V_{shell} + V_{core} = [(l_{NC} \times w_{NC} \times h_{NC}) - \{(\pi \cdot r_{NR}^2 \cdot l_{NR}) + (\frac{4}{3} \cdot \pi \cdot r_{NR}^3)\}] + (\pi \cdot r_{NR}^2 \cdot l_{NR}) + (\frac{4}{3} \cdot \pi \cdot r_{NR}^3) \quad (4.3)$$

where r_{NR} , l_{NR} is the radius and length of the nanorod respectively. l_{NC} , w_{NC} , h_{NC} is the length, width and the height of the nanocuboid respectively. Au and Ag exists as a face centered cubic (fcc) lattice structure, the lattice parameter is 407.88 pm. In a fcc structure one unit cell contains 4 atoms, the volume of the unit cell is $6.78 \times 10^{-29} \text{ m}^3$. This can help calculate the number of Au/Ag atoms in a NR/NC. With the help of ICP-MS the Au and Ag ion concentration c_{ICP} was determined in g/l. The amount of metal (Au, Ag) atoms in the total volume can be calculated with the help of the Avogadro's number N_A and the molar mass of metal M_{MNP} by the following equation:

$$N_{MNP} = \frac{c_{icp} \times V_{tot} \times N_A}{M_{MNP}} \quad (4.4)$$

For Au@Ag NCs sample 5 the main contribution in the SPR is due to the Ag shell, therefore, only the volume of silver shell is considered when calculating the number of Au@Ag NCs in the pellet solution. Table 4.1 shows the values obtained for various parameters to calculate the number of Au NRs or Au Ag NCs per litre. This number can be easily converted to ppm by dividing it by the weight of each MNP. The quantification methodology can also be extended to spherical MNPs (see Appendix B). The results obtained from the experiments were also corroborated by a Finite-difference time-domain (FDTD) model (SETHI et al., 2019).

| MNP | ICP concentration ($\mu\text{g}/\text{l}$) | Volume of MNP (m^3) | Number of metal atoms in one MNP | Number of metal atoms in total volume | Concentration of sample (N/L) |
|-----------------------|--|-------------------------|----------------------------------|---------------------------------------|-------------------------------|
| Au NR sample 1 | 89 | 2.644E-24 | 155998.4553 | 2.72E+16 | 1.74433E+15 |
| Au@Ag NC silver shell | 37 | 2.110E-23 | 1244837.758 | 2.08E+16 | 1.67463E+14 |

Table 4.1: Number of Au NRs and Au@Ag NCs in a given volume.

4.4.1 Assumptions made to calculate MNP concentration

- The volume of the MNPs were calculated by assuming certain geometrical shape. The shape of Au NRs was assumed to be a cylinder capped with two hemispheres. For Au@Ag NCs sample 5 the contribution to the extinction spectra is solely due to Ag, therefore the volume of the Ag shell was calculated and it was assumed that the gold core is a cylinder with hemispherical ends.
- For both type of MNPs the contribution of CTAB/CTAC capping to the size and weight of an MNP is disregarded. The size of CTAB on a Au NR is of the order of a few tens of angstrom (GÃşmez-GraÃşa et al., 2012).
- It is assumed that all the extra additives have been removed by the multiple rounds of centrifugation and the MNPs are homogeneously dispersed in solvent and nanocomposite.

4.5 Surface functionalization of anisotropic MNPs

The Au NRs and Au@Ag NCs were prepared in aqueous solution. Aqueous based synthesis of the MNPs is more widely used because it allows precise shape and size control, and achieves the desired concentration. However, for embedding the synthesized MNPs into the host matrix Silicone it is required to disperse the MNPs in different solvent media that are compatible with Silicone. Rather than developing new routes of synthesis of MNPs in the desired solvent it is better to phase transfer

it to the solvent of interest. To perform a phase transfer it is important to functionalize the MNPs with the proper organic or inorganic material to grant stability under the necessary conditions as well as to provide added functionality.

The desired optical properties of the MNPs can change due to aggregation during functionalization. Moreover, the surface functionalization of NRs/NCs surface is usually more challenging than functionalization of spherical nanoparticles, as the latter can be coated directly with thiol during synthesis (Brust et al., 1994). The Au NRs and Au@Ag NCs were synthesized in the presence of a strong capping agent CTAB and CTAC respectively. CTAB/CTAC capping agent presents a different surface to that of 'bare' NRs capped with citrate or similar ligands; therefore, specific methods are required to functionalize CTAB/CTAC capped NRs/NCs.

To understand a way to functionalize the NRs it is important to know the general structure and coating of CTAB/CTAC on the NR surface. CTAB molecules form a partially-interdigitated bilayer on the surface of Au NRs (Nikoobakht and El-Sayed, 2001). The Au/Ag surface has a negative charge due to the adsorbed bromide or chloride ions.

The ammonium head-group of CTAB has a positive charge and binds to the Au surface through electrostatic interaction forming the inner layer. The carbon tail is hydrophobic in nature, another layer of CTAB molecules is formed with the hydrophobic tail pointing inside interacting with the inner layer and the ammonium head-

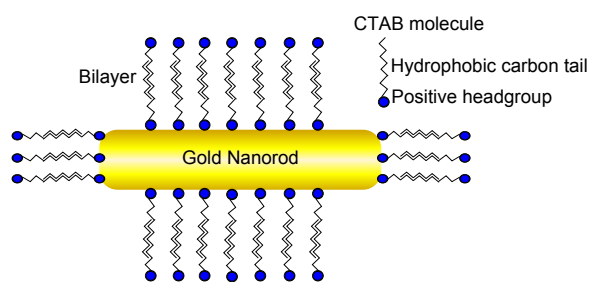


Figure 4.11: Drawing of a Au NR capped by CTAB, CTAB forms a bilayer on the nanorod and consists of a positive bromide headgroup and hydrophobic carbon tail.

group pointing outside. The binding of CTAB molecule to the surface of Au NR can be better understood by the drawing shown in Figure 4.11. The presence of this bilayer makes the Au NRs positively charged and stable in water. The bilayer can be disrupted by lowering the CTAB concentration below the critical micelle

concentration, addition of organic solvents and high salt concentration in the solution (Huang et al., 2009).

The strong bond energy of thiol-gold (253.6 ± 14.6 kJ/mol⁻¹) and thiol-silver (216.7 ± 14.6 kJ/mol⁻¹) can be utilized to functionalize the NRs/NCs. However, merely adding the thiol group may not lead to the complete exchange with the surfactant. Mercaptoundecanoic acid (MUA), a commonly used thiol group can lead to aggregation of the nanoparticles or a partial exchange (Thierry et al., 2009). Dodecanethiol (DDT) has also been used to directly functionalize CTAB capped Au NRs and transfer them into organic media with the help of acetone as the common solvent (Thierry et al., 2009). The Au NRs synthesized for this work could not be transferred efficiently to DDT, moreover, the addition of acetone led to agglomeration of the nanorods as it removed CTAB capping from the Au NRs. Thiol-terminated PEG molecules have been used to impart high stability to gold nanorods (Rostro-Kohanloo et al., 2009) by simply adding them to the aqueous solution of centrifuged nanorods (Liao and Hafner, 2005). In this study PEG-SH was used to functionalize both the Au NRs and Au@Ag NCs.

In our case, a normal exchange of surfactant with the functional group was possible under aqueous conditions for an appropriate ligand structure with molecular weight of 5,000 g/mol. The NRs/NCs obtained after the second centrifugation step were used for functionalization with PEG-SH. A stock solution of 0.5 mM PEG-SH in DI water was prepared by simply stirring the polymer in water for 5 minutes. PEG-SH was added to 5 ml of Au NR and Au@Ag NC solution, the resultant solution was stirred for 18 hours at room temperature. Instead of stirring the solution for 18 hours, it can be kept at 4°C for 24 hours and the obtained results were similar in both cases. 0.1 M of NaCl was added to PEGylated MNPs and CTAB coated MNPs, the latter aggregated immediately after addition of the salt (Rahme et al., 2013). The extinction spectra of the PEGylated NRs/NCs can be seen in Figure 4.12.

The longitudinal plasmon bands retained their shape and width implying

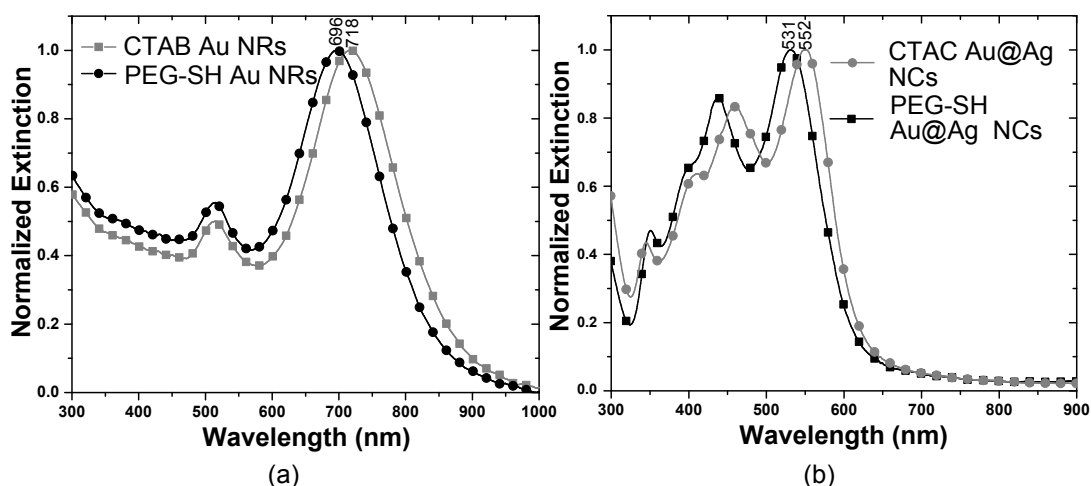


Figure 4.12: UV-VIS spectra of a) Au NRs and b) Au@Ag NCs before and after PEGylation depicting the blue shift in the PEGylated MNPs.

that the MNPs are well dispersed in solution and no aggregation has occurred. A blue shift of ~ 20 nm is observed in the surface plasmon bands of both Au NRs and Au@Ag NCs. As pointed out in section 2.9, the presence of a non-metallic shell such as a thiol layer can decrease the effective size of the MNPs thus, it is a possibility that the blue shift in the plasmon bands of the NRs/NCs is due to decrease in their effective size. After the MNPs were functionalized they were transferred to DCM.

4.6 Phase transfer of anisotropic MNPs

The first approach to transfer MNPs from aqueous to organic phase is ligand exchange with hydrophobic molecules. This process resulted in precipitation of the NPs, and that makes the re-suspension of the NPs without aggregation into organic medium difficult. The second approach that is used in this research study is phase transfer catalysis across the liquid-liquid interface. The NPs can be transferred to DCM or chloroform by using a common solvent such as acetone, ethanol or methanol. Using a common solvent is important because the NPs do not transfer to the organic solvent simply by adding and mixing the PEGylated NPs in organic solvent. Addition of ethanol and methanol resulted in the phase transfer of the

nanoparticles into the organic solvent. Methanol resulted in the concentration of the NPs into the organic solvent as compared to ethanol which failed to concentrate the NPs. Methanol increases the solubility of DCM in water thus decreasing the final volume of DCM that contains the MNPs, hence concentrating the nanorods in DCM. This is in agreement with previously published work (BaniáYaseen, 2014).

To ensure an efficient phase transfer; 2 ml of PEGylated NRs/NCs were added to 2 ml of DCM. Two immiscible layers were formed as is shown in Figure 4.13 for Au NRs. The top layer is of water containing the MNPs, the bottom layer is of denser DCM. Only after addition of 3 ml of methanol the phase transfer is induced with the NRs/NCs being transferred to DCM layer at the bottom. The volume of methanol is crucial as the addition of excess methanol resulted in the formation of a monophasic solution. The addition of a common solvent is crucial as it reduces the interfacial tension at the liquid-liquid interface and the spontaneous assembly of PEG-SH molecules favour the DCM phase more than the water base ensure efficient transfer of Au MNPs. After 15-20 minutes the top layer becomes clear Figure 4.13 thus implying phase transfer of the MNPs.

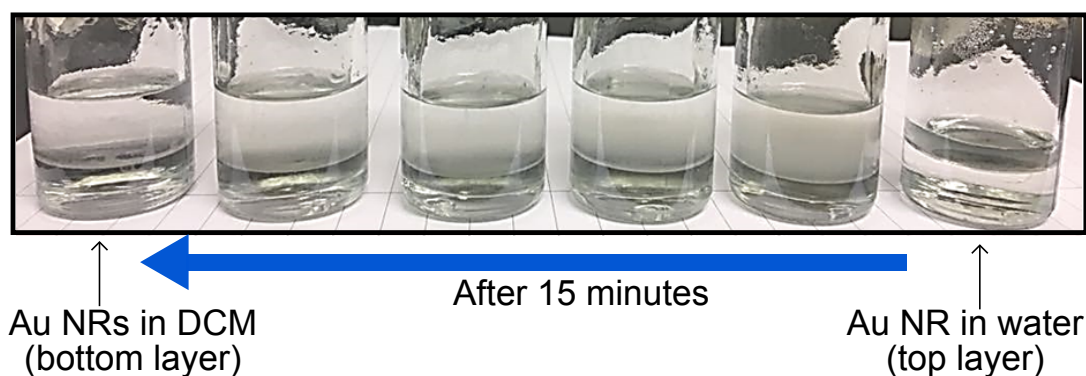


Figure 4.13: Phase transfer of the Au NRs after addition of 3 ml of methanol, the transfer process from right to left.

The MNPs in DCM were centrifuged at 12,000 g for 15 minutes and the pellet was re-dispersed in DCM. The UV-VIS spectra of the MNPs before and after the phase transfer is shown in Figure 4.14. A red shift is observed in the plasmon band for both the MNPs, this red-shift is due to change in refractive index, DCM has a

refractive index of 1.4 that is higher than the refractive index of water. The longitudinal plasmon band of Au@Ag NCs shifted from ~531 nm to ~552 nm, the ratio between the longitudinal and transverse plasmon band is similar for both cases. The FWHM of the longitudinal plasmon band is the same, therefore, indicating no change in the shape of the NCs on phase transfer. Similarly, for Au NRs the longitudinal plasmon band red-shift from ~696 nm to ~715 nm. The amount of red-shift is similar for both the MNPs.

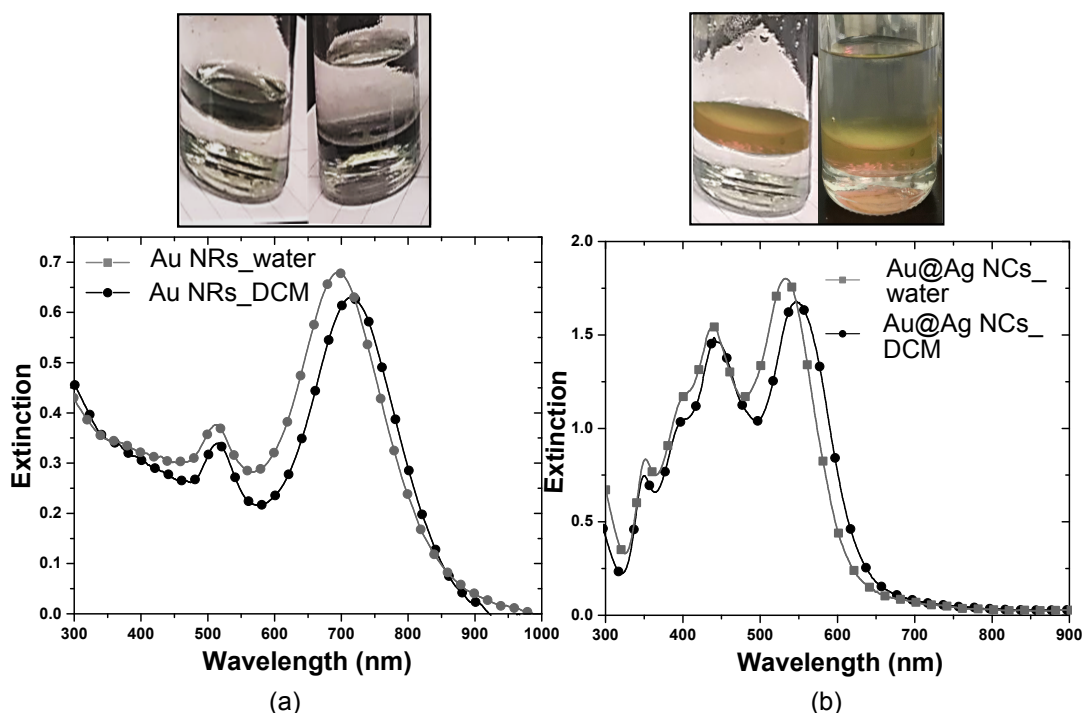


Figure 4.14: Photograph and UV-VIS spectra of a) Au NRs sample 1 and Au@Ag NCs sample 5 before and after phase transfer

Even though majority of MNPs are transferred to DCM the top layer containing water and methanol is not completely transparent, the phase transfer efficiency can be calculated by the extinction intensity of the MNPs before and after phase transfer:

$$Efficiency = \left(1 - \frac{E_{after}}{E_{before}}\right) \times 100 \quad (4.5)$$

where E_{before} is the peak extinction intensity of PEGylated MNPs before phase

transfer in aqueous solution, E_{after} is the peak extinction of the aqueous upper layer after phase transfer. With the help of the UV-VIS spectra shown in Figure 4.15 it was possible to calculate the phase transfer efficiency of Au NRs and similarly for Au@Ag NCs. The phase transfer efficiency was 84% and 75% for Au NRs and Au@Ag NCs respectively.

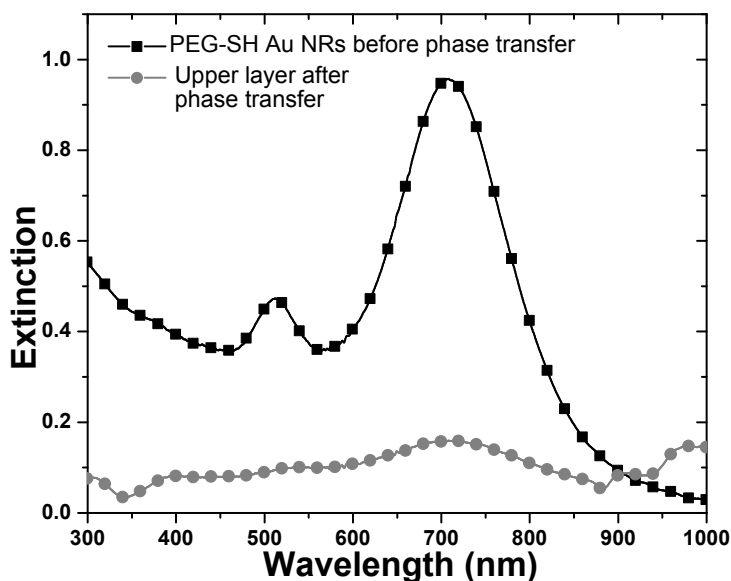


Figure 4.15: UV-VIS spectra of Au NRs coated with PEG in water and Au NRs in the aqueous upper layer after phase transfer.

To achieve a high phase transfer efficiency, it is important to:

- Remove the excess surfactant to ensure that it does not hinder in the functionalization of the MNPs.
- Always take the UV-VIS spectra before PEGylation to observe any shift in the longitudinal plasmon band.
- Use less than 3 ml of the MNPs solution as the phase transfer becomes inefficient if more than 3 ml is used.
- Allow at the least 20 minutes for the phase transfer to be complete this can be confirmed by the transparent aqueous upper layer.
- Centrifuge the samples, after phase transfer, at 12,000 g for 15 minutes and

re-disperse them in DCM. This step is crucial to remove the excess methanol in the organic solvent and ensure long-term stability of the nanorods.

4.7 MNPs in Silicone polymer

The Au@Ag nanocomposite was fabricated in a cuvette that had similar path length (1 cm) to the cuvettes used in the UV-VIS absorption measurements and the Au NR nanocomposite was a layer of $2.5 \times 2.5 \times 0.1 \text{ cm}^3$. The concentration of the Au NRs in the nanocomposite is calculated to be 20 ppm after accounting for the loss of NRs in the phase transfer process. The extinction spectra for both the Au NRs and Au@Ag NCs nanocomposite samples is shown in Figure 4.16. The optical properties of Au NRs and Au@Ag NCs depend on the alignment and spacing of nanoparticles. The refractive index of DCM and the polymer is similar (1.42) at room temperature so the blue-shift and change in the shape of the plasmon band of Au NRs can be due to the side to side alignment of the NRs in the polymer (Jiang et al., 2012a). For Au@Ag NCs a slight red-shift is observed for the longitudinal plasmon band and the peak 405 nm is barely discernible. The difference in the assembly of the Au@Ag NCs in the polymer as compared to the Au NRs could be because of the difference in the shape, aspect ratio of the MNP (Surve, Pryamitsyn, and Ganesan, 2007).

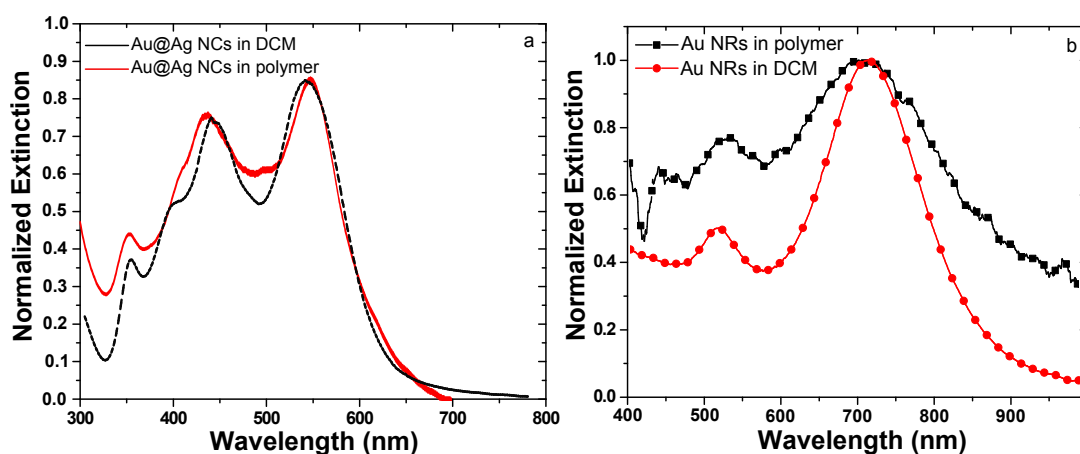


Figure 4.16: UV-VIS spectra of Au NRs and Au@Ag NCs in DCM and Silicone polymer.

Au NRs nanocomposite was found to be stable for one year; Au@Ag NCs nanocomposite, on the other hand, were found to be stable for six months as can be seen in Figure 4.17. For Au NRs, the shape and height of the longitudinal plasmon band is the same after a year. However, for Au@Ag NCs there is no peak observed at 410 nm after six months, it is possible that the the NCs got aggregated as can be seen by the spectra of the NCs taken after one year. This can be due to the oxidization of the Ag shell on the NCs. Further analysis is needed to study the long term stability of MNPs in a polymer.

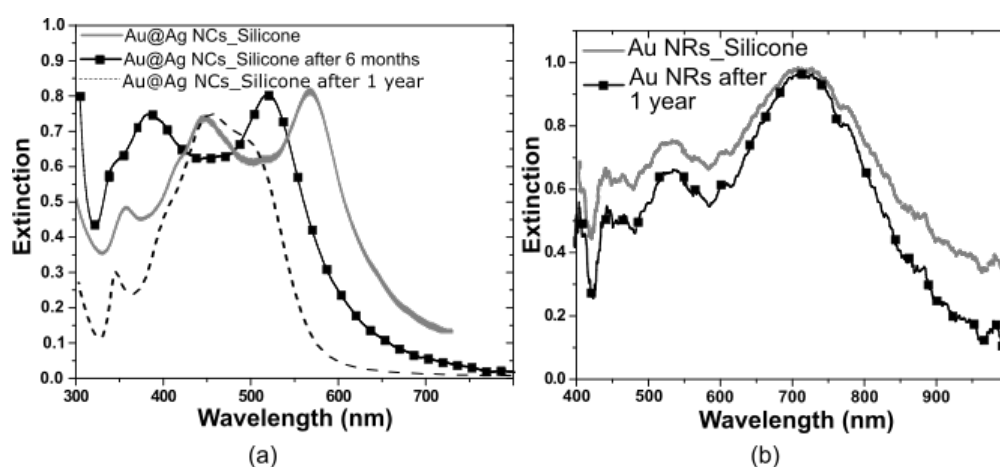


Figure 4.17: Extinction spectra of a) Au@Ag NCs taken after six months, b) Au NRs after one year of dispersion in polymer.

4.8 Conclusions

CTAB stabilized Au NRs were synthesized by chemical reduction of gold precursor in aqueous solution. Two distinct plasmon bands were observed, with a high intensity ratio between the longitudinal and transverse peak. A red-shift in the longitudinal plasmon is observed on increasing Ag to Au ratio in the growth solution. To utilize the broad plasmonic range of Ag, CTAC capped Au@Ag NCs were synthesized by using Au NRs as seeds. Four plasmon bands are observed and a distinct peak at 345 nm indicated the presence of Ag shell.

By-products were inevitable in wet seed-mediated synthesis. Two-step centrifu-

gation was carried out to remove the by-products and extra additives. The UV-VIS spectra of the pellet and supernatant solutions after the second centrifugation step gives insight about the shape of the MNPs in those solutions. For Au NRs, lower aspect ratio NRs and spheres are present in the pellet solution. For optimized sample of Au@Ag NC smaller aspect ratio NCs are found in the pellet solution. The absence of peak at ~ 365 nm is due to the absence of Ag shell on the MNPs present in the supernatant solution.

SEM and TEM images of the MNPs gave a good idea about the morphology of the NRs and NCs. For Au NRs sample 1 majority of the NRs are ~ 27 nm long giving an aspect ratio of $\sim 2.7 \pm 0.2$. As for Au NR sample 2 majority of NRs are ~ 36 nm in length and have an aspect ratio of 3.6 ± 0.4 . For optimized Au@Ag NCs majority of NCs have length between 54-57 nm with an aspect ratio of 1.8 ± 0.2 . With the help of TEM imaging Ag shell was found to be 6 nm and 9 nm on the ends and sides respectively.

The quantification of Au NRs and Au@Ag NCs in a given volume was carried out with the help of size analysis and ICP-MS. Volume of a MNP was calculated with the help of the size analysis and then the number of metal atoms per MNP could be calculated. All samples are assumed to be monodispersed, and for Au@Ag NCs the volume of the Ag shell was calculated, these factors can add some discrepancy in the calculated concentration values of MNPs. The experimental results were also validated by a FDTD based model.

PEG (Mw: 5000) was found to functionalize both Au NRs and Au@Ag NCs efficiently. The functionalized NRs/NCs were transferred into DCM without aggregation and with an efficiency of 84% and 75% respectively. The MNPs in DCM were found to be compatible with the host matrix Silicone. The stability of the MNPs was tested by change in their shape or agglomeration that caused a change in the optical properties of the nanocomposite. Au NRs and Au @Ag NCs nanocomposites were found to be stable for one year and six months respectively.

Chapter 5

Luminescent Solar Concentrator Characterization

This chapter can be divided into three core parts. The first part deals with the quantum yield results of Lumogen Red305 dye and ZnCuInS/ZnS core shell QD in Silicone host matrix. The second part focuses on the doping concentration optimization of Red305 dye in a $4.5 \times 4.5 \times 0.3 \text{ cm}^3$ size waveguide. The doping concentration is optimized by optical characterization. For optical characterization, two types of emission measurements are carried out. The first type involves the measurement of emission from all the surfaces of the waveguide by placing the waveguide inside an integrating sphere. The second type involved the measurement of emission from the edges of the waveguide by placing the waveguide at the opening port of an integrating sphere. Different doping concentration of Red305 dye LSC devices are fabricated and different devices are simultaneously tested in outdoor conditions. The final part of the chapter focuses on the fabrication and characterization of titanium dioxide (TiO_2) NPs based back diffuse reflectors. Optimum concentration of TiO_2 is found for $5 \times 5 \times 0.1 \text{ cm}^3$ in comparison to an aluminum specular reflector. Finally, the LSC waveguides are tested with the back reflectors.

5.1 Fluorophore characterization in silicone polymer

As discussed in section 2.3.1 organic dyes are the most commonly used fluorophores in LSC devices. Lumogen dyes have good solubility in a wide range of organic solvents. The dyes have high photoluminescent quantum yield (PLQY) in solution and PMMA (Wilson and Richards, 2009). This is a good indication to investigate the compatibility of the dyes in Silicone polymer. Initially, two visible emitting fluorescent organic dyes (Red305 dye, Yellow083 dye) from the Lumogen F range by BASF were studied. Yellow dye was found to be incompatible with the Silicone polymer (see Appendix C for details), therefore, the focus was shifted to only Red305 dye. ZnCuInS/ZnS core shell QDs were also characterized in the Silicone polymer. The core shell QD was characterized in the polymer due to the high Stokes' shift as compared to the organic dyes.

Samples of Silicone with known concentration of fluorophores were made by drop casting. The samples had optically flat surface and four measurements were taken at each corner and the results were averaged. The stock solution of the fluorophores was made in DCM, and two different concentrations for each fluorophore were fabricated to measure the PLQY. As discussed in section 3.6.1, for PLQY measurement, samples with weak concentration of fluorophores were used to minimize re-absorption effects. The absorption and emission spectra of the fluorophores can be seen in Figure 5.1. Red305 dye has well-defined spectral peaks in Silicone. The absorption range is from 300-600 nm with three absorption peaks at 421 nm, 542 nm and 564 nm, respectively. The maximum absorption and emission peak for Red305 is at ~564 nm and ~600 nm, respectively, with a Stokes' shift of around 36 nm. As for the QDs, there is no distinct absorption peak, a bump at ~575 nm is observed and the emission peak is at ~700 nm. The Stokes' shift for the QDs is around 120 nm.

PMMA is an established host material for Lumogen dyes (Wilson, 2010). Red305 in PMMA exhibits a maximum absorption peak at ~574 nm for varying Red305 doping concentration 25-70 ppm (Wilson and Richards, 2009). In Silicone a blue-

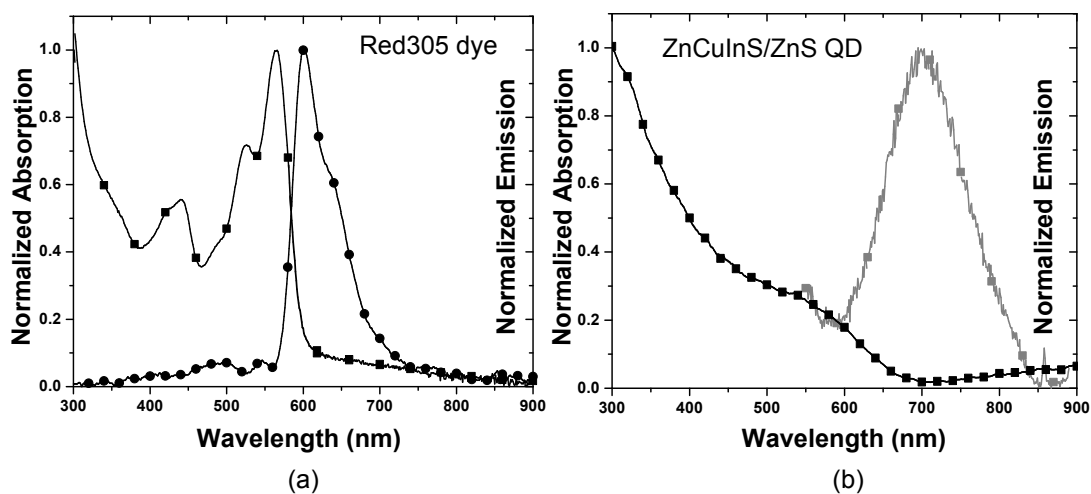


Figure 5.1: Normalized absorption and emission spectra of a) Red dye and b) QD used in this work.

shift to ~ 564 nm is observed in the maximum absorption peak for the same dye. This is in agreement with BASF data that shows peak absorbance values differ according to the host material (*Lumogen F Collector Dyes: Technical Information*). To understand if Red305 was functioning well in Silicone, the peak absorbance values and concentrations of the dye in Silicone was calculated as shown in Table 5.1. The Beer-Lambert law discussed in section 3.3 was used to calculate the concentration of Red305 in Silicone. If Silicone was a poor host material for the dye, then less dye molecules will fully dissolve in the polymer and the rest will form agglomerates (Edelenbosch et al., 2013). If dye agglomerates absorb more light than dye molecules, it will lead to high concentration values using the Beer Lambert law. The measured concentrations for low concentration samples are approximately equal to the calculated concentrations of the dye, therefore, implying the suitability of Silicone as host for Red305. For 150 ppm sample, the measured concentration is lower than the concentration used to make the sample. This might be due to the dye not completely dissolved in DCM before mixing it with Silicone Part A. For high dye concentration samples, a larger volume of DCM was used to ensure complete dissolution of the dye.

| Conc. of dye used to make samples (ppm) | Absorbance peak | Sample thickness (cm) | Conc. calculated using Beer-Lamberts law |
|---|-----------------|-----------------------|--|
| 10 | 0.14 | 0.31 | 10 |
| 30 | 0.38 | 0.3 | 28 |
| 50 | 0.63 | 0.29 | 57 |
| 70 | 0.85 | 0.3 | 76 |
| 150 | 1.35 | 0.29 | 122 |

Table 5.1: Measured Red305 dye concentrations for Silicone samples.

For the PLQY measurement, excitation and emission spectra were recorded both with the sample in the integrating sphere and with the blank to correct for the absorption of the Silicone polymer. The difference in the areas of the excitation and emission spectra with and without the sample gives the PLQY as mentioned in section 3.6.1. The samples in the integrating sphere were placed at an angle of 15 degrees for all the measurements. A neutral density filter (0.5 % transmission) is inserted at the emission port after the integrating sphere to prevent the damaging of the photomultiplier tube. Then the excitation spectrum is detected for both the sample and the blank. Another neutral density filter of the same or higher transmission is inserted in the excitation path before the integrating sphere. The detector signal is then measured both with and without the emission filter in place. The background spectra is subtracted and the ratio of signal with the emission filter in or out gives the correction factor that is applied to the excitation spectra. The different concentrations used to take the absorption, emission spectra and measured PLQY of the fluorophores is given in Table 5.2. To test the repeatability of this method, each sample was measured three times and an error of not more than 2% was found in the measured values.

| Fluorophore | Conc. for absorption | Conc. for emission | Excitation wavelength (nm) | Measured PLQY (%) |
|-----------------|----------------------|--------------------|----------------------------|-------------------|
| Red305 sample1 | 10 ppm | 2.7 ppm | 530 | 98±2 |
| Red305 sample 2 | 10 ppm | 3.0 ppm | 530 | 97±2 |
| QD sample 1 | 0.05 wt% | 0.01 wt% | 450 | 20.34±0.5 |
| QD sample 2 | 0.05 wt% | 0.02 wt% | 450 | 19±0.4 |

Table 5.2: Different samples concentrations, their excitation wavelengths and measured PLQY.

5.2 Red305 luminescent solar concentrator

Seven LSC waveguides (1-7) of $4.5 \times 4.5 \times 0.3 \text{ cm}^3$ size with varying doping concentration (10-160 ppm) of Red305 were fabricated as discussed in section 3.7. The sample thickness was measured at all the four corners and the centre and a deviation of not more than $\pm 0.1 \text{ mm}$ in thickness was observed. The absorption and emission measurements were carried out for all these samples to understand the role of the doping concentration on the edge emission profile of the LSC. This further helped in optimizing the Red305 doping concentration for the particular LSC size.

5.2.1 Absorption profile of Red305 LSC

The absorption spectra of the Red305 LSC waveguides can be seen in Figure 5.2a. As expected increasing the concentration of Red305 in the polymer increases the absorption intensity of the waveguide. The integrated absorbance taken between 350 nm to 650 nm linearly follows the Red305 doping concentration as seen in Figure 5.2b. It is observed that for 0 ppm doping concentration the integrated absorbance is not zero, which is contrary to the expected zero absorption for blank sample. This might be due to an experimental error.

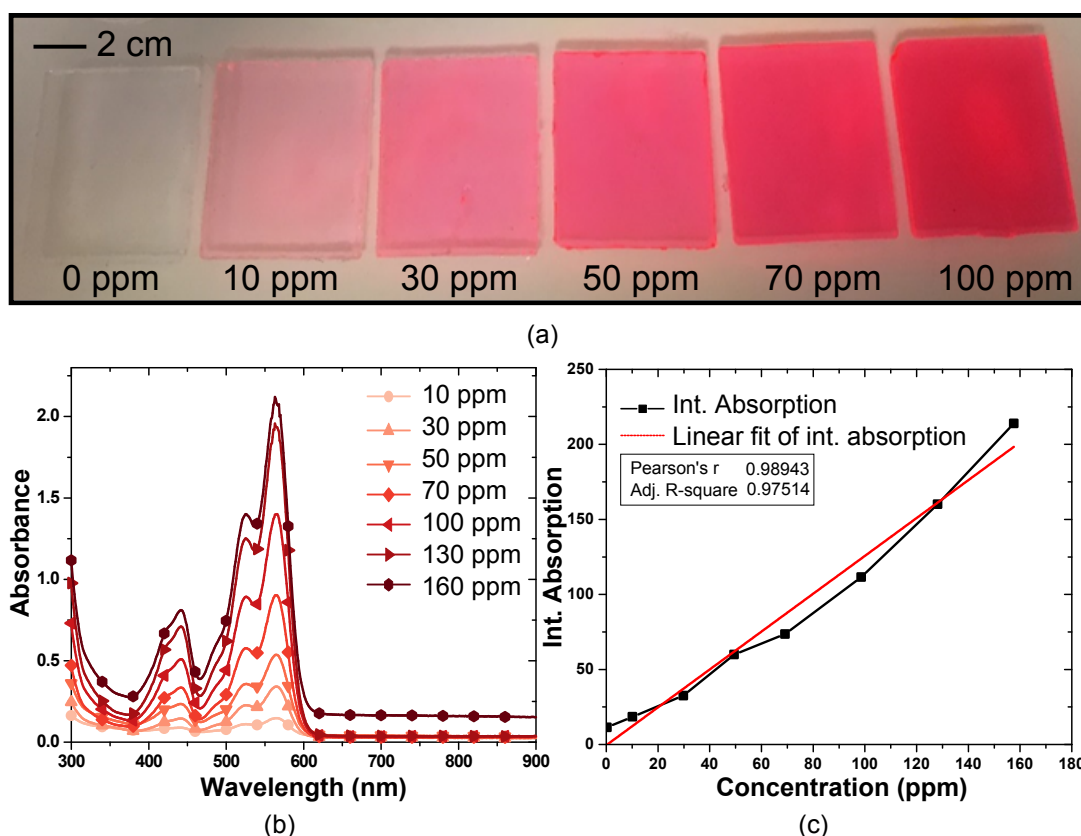


Figure 5.2: a) Photograph of a blank Silicone polymer and LSC waveguides with 10-100 ppm Red305 doping concentration, b) Absorption spectra of Red305 (10-160 ppm) concentration in Silicone, c) Analysis of integrated absorbance with doping concentration in the waveguide.

5.2.2 Total emission profile of Red305 LSC

The total emission from the waveguide was measured by placing the waveguide inside the integrating sphere, the setup is described in section 3.8.1. The emission spectrum of the Red305 begins at 550 nm, therefore, the excitation wavelength needed to be lower than 550 nm. This was achieved by using a wavelength filter (460 nm) in front of the light source. The integration time was set at 6000 ms.

The emission spectra of all the samples can be seen in Figure 5.3a. The shape of the emission spectra changes on increasing the dye concentration in the waveguide. For low concentration 10 ppm, two peaks are observed in the emission spectrum; the prominent one at ~602 nm and a small peak at ~640 nm. Both the peaks are characteristic of the molecular emission spectrum of Red305 dye. However, as the

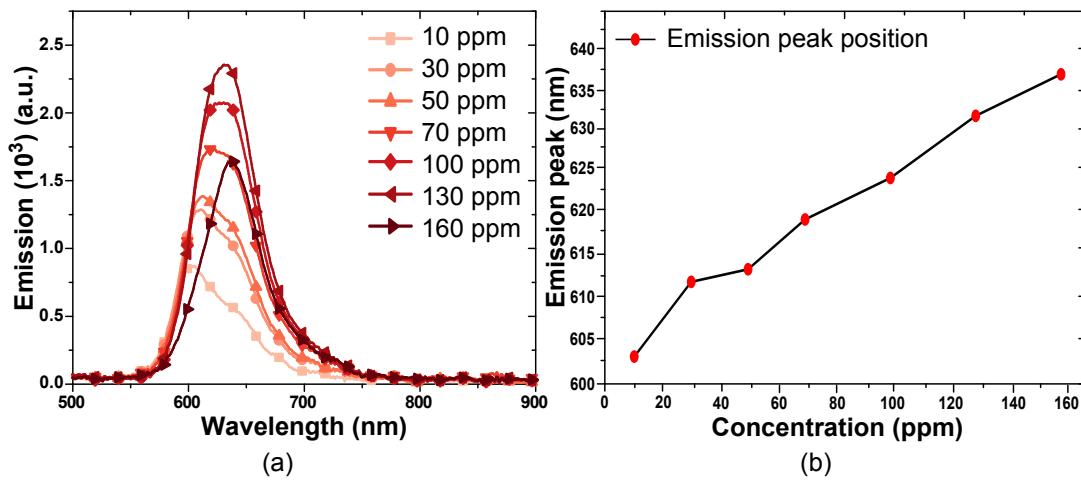


Figure 5.3: a) Total emission spectra of LSC waveguides measured using an integrating sphere, b) Position of the emission peak on varying the doping concentration.

concentration is increased from 10-50 ppm a red-shift is observed in the prominent emission peak from 602-613 nm, respectively and the second peak completely disappears as the Red305 doping concentration reaches 70 ppm. For higher (above 50 ppm) dye concentrations a broad emission peak is observed, the peak drastically red-shifts to ~ 636 nm for 160 ppm sample. The red-shift of the emission peak position by varying the doping concentration of Red305 can be seen in Figure 5.3b. There is a spectral overlap of ~ 36 nm in the absorption and emission spectrum of Red305 dye. This means that the photons emitted by one dye molecule can be re-absorbed by another dye molecule before exiting the waveguide. As the concentration of dye molecules in the waveguide increase the probability of re-absorption also increases. The re-emitted photons have a lower energy and that accounts for the red-shift observed in Figure 5.3b.

As noted in section 5.2.1, the integrated absorption linearly increases with increase in the Red305 doping concentration. One would expect a similar trend for total integrated emission as a function of Red305 doping concentration in the waveguide. However, as seen in Figure 5.4 the total emission deviates from linear-

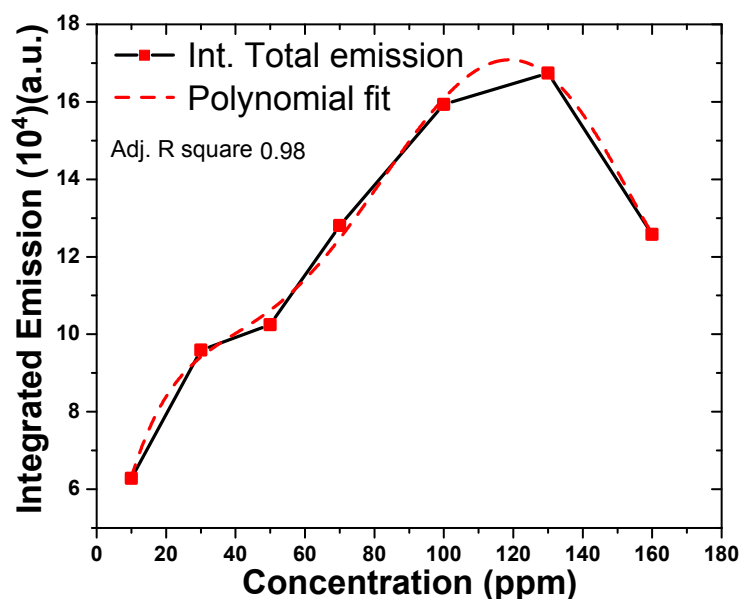


Figure 5.4: Variation of total integrated emission from LSC waveguides with Red305 doping concentration, the polynomial fit is by a five degree polynomial equation.

ity at high doping concentration. The efficiency of the waveguide does not linearly increase on increasing the doping concentration and is a non-linear function of the doping concentration. This non-linearity in total emission from LSC waveguide can be attributed to re-absorption losses. Re-absorption losses are a function of the doping concentration and the optical path length. When the sample is placed in the integrating sphere the fluorescence emission is from all the surfaces, making it difficult to correctly estimate the optical path length. To further investigate the optimum Red305 doping concentration the edge emission was measured of the LSC waveguides.

5.2.3 Edge emission profile of Red305 LSC

The edge emission from the waveguides was measured by using the setup described in section 3.8.1. The position and spot size of the light beam was kept constant for all the waveguide samples. The excitation wavelength was chosen to match the absorption of the Red305 dye in the waveguide. It is not essential to excite the dye at exactly its peak absorption, the wavelength was chosen so as not to interfere

with the emission spectrum and give a high signal strength. The integration time was set at 6500 ms.

The emission spectra from the edge of the waveguides can be seen in Figure 5.5a. The edge emission increased on increasing the doping concentration from 10-100 ppm, this is due to the increase in the absorption coefficient of the waveguide. A decrease in edge emission intensity is observed for 130 ppm and 160 ppm sample. The decrease in the intensity of edge emission can be attributed to re-absorption losses, combination of re-absorption loss along with the escape cone loss can result in the photon being lost before reaching the edge of the LSC waveguide. It is to be noted that the emission intensity of 100 ppm sample is slightly higher than the intensity of 130 ppm sample, contrary to the total emission experimental results. Therefore, emission from all the four edges was taken twice to find out the error arising due to the defects on the edges of the waveguides. A maximum error of $\pm 10\%$ was found for the 130 ppm sample. Similar to the total emission from the waveguides, the edge emission peak red-shifted from ~ 600 nm for 10 ppm sample to ~ 637 nm for 160 ppm Red305 doping concentration as seen in Figure 5.5b. The red-shift of the emission peak follows a linear trend with the doping concentration. Therefore, it can be concluded that re-absorption losses cause the red-shift in the emission peak from the LSC waveguide.

The integrated edge emission variation with the doping concentration can be seen in Figure 5.6. Similar to the integrated total emission the edge emission output varies non linearly with increase in the Red305 doping concentration.

The overall efficiency is a non-linear polynomial function of the doping concentration with good fitting parameter of Adj. R square 0.98. Value of the error bars are used as weighting coefficients to obtain the polynomial fit. For $4.5 \times 4.5 \times 0.3$ cm³ size LSC waveguide, Red305 dye doping concentration above 100 ppm results in a decrease in the edge output of the waveguide. 70 ppm was chosen as the Red305 dye doping concentration for the LSC waveguide of size $4.5 \times 4.5 \times 0.3$ cm³.

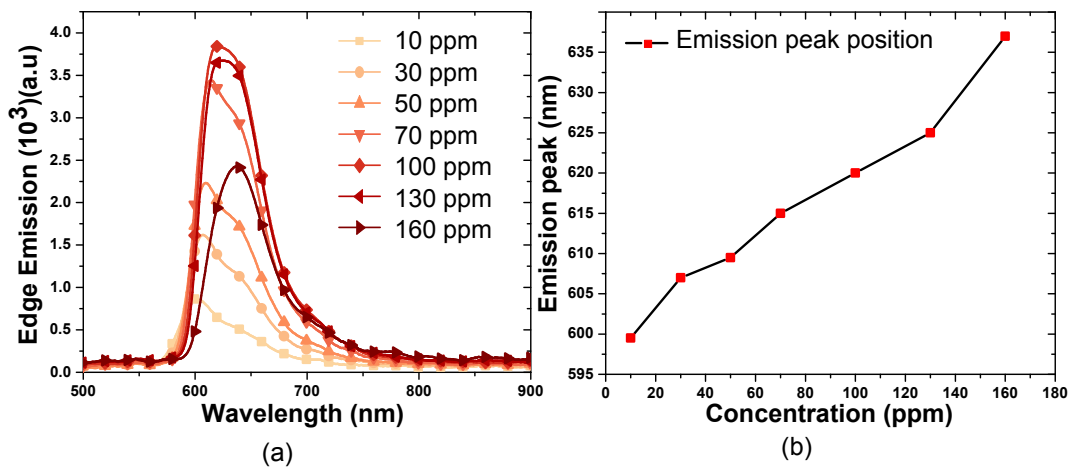


Figure 5.5: a) Edge emission intensity for various Red305 doping concentrations (10-160 ppm), b) Variation of the emission peak position on increasing the Red305 doping concentration in the waveguide.

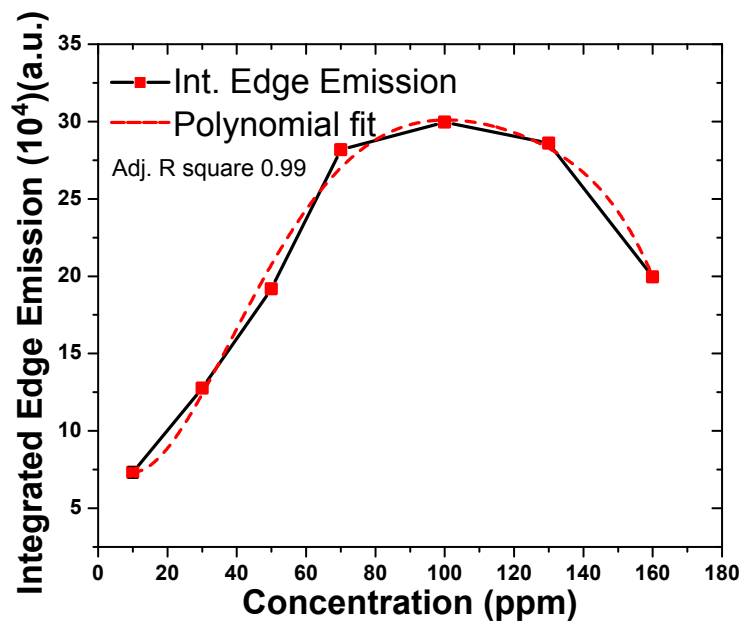


Figure 5.6: Integrated edge emission of LSC waveguide with variation in Red305 dye concentration.

5.3 Outdoor electrical characterization

Due to unavailability of a solar simulator, a decision was taken to test different LSC devices in outdoor conditions. For the electrical characterization of the LSC devices, the simultaneous real time measurement of three LSC devices along with a

blank reference was carried out on the roof of Simon Perry building, Trinity College Dublin as shown in section 3.8.3. This gave an opportunity to optimize the setup for future testing of PLSC devices in outdoor conditions. The outdoor setup was covered by a 4 mm thick low iron glass as shown in Figure 5.7. The low iron content in the glass maximized the solar energy transmittance. The low iron glass (Pilkington Optiwhite) used in this work was sourced from Nippon Sheet Glass group and had high solar transmittance of 92%.

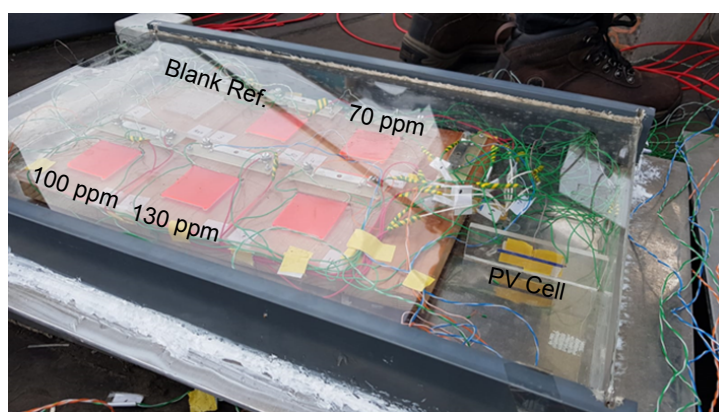


Figure 5.7: Photograph of the outdoor setup consisting of different LSC devices, blank reference and PV cell in vertical position.

Initially, all the samples with doping concentration from (30-160) ppm were connected to the data logger, but the solar cells attached to 30, 50 and 160 ppm samples were found to be broken, therefore, no data was collected for those samples. PV cell sourced from SolarCapture had 19% efficiency under standard test conditions. The solar cells were attached to one edge of the PLSC waveguide using a conductive adhesive with acrylic resin base. The PV cells illumination surface measured 50×3 mm, therefore, the part of the solar cell not attached to the PLSC waveguide was covered by black tape. The connecting wires were carefully soldered to the solar cells so as to not to damage or break the cell. A PV cell not coupled to any polymer was also tested, this PV cell was placed in a vertical position so as to mimic the position of the PV cell attached to LSC waveguide. A thermocouple was attached to the back of the PV cells by using the same adhesive

as before.

In outdoor conditions the AM 1.5 G spectrum is rarely realized. Factors such as the presence of clouds, rain, position of the solar disc can impact the solar spectra incident on the LSC devices. The experiment was carried out on 22 August 2018. It was a cloudy day with the cloud cover ranging from 6 to 9 oktas (overcast) throughout the day. The okta scale ranges from 1 to 9, where 1 represents a cloudless day and 9 represent a completely overcast day. The average solar radiation can be seen in Figure 5.8a, the time when the sun is at zenith (1 pm) approximately the clouds cover the solar disc resulting in a drastic drop in the solar radiation. The average power output throughout the day for the LSC devices, blank reference and the PV cell can be seen in Figure 5.8b. A change in the edge power output is seen due to different radiation intensity. As the cloud cover was present during the whole day it was difficult to assess its effect on the efficiency of the LSC device.

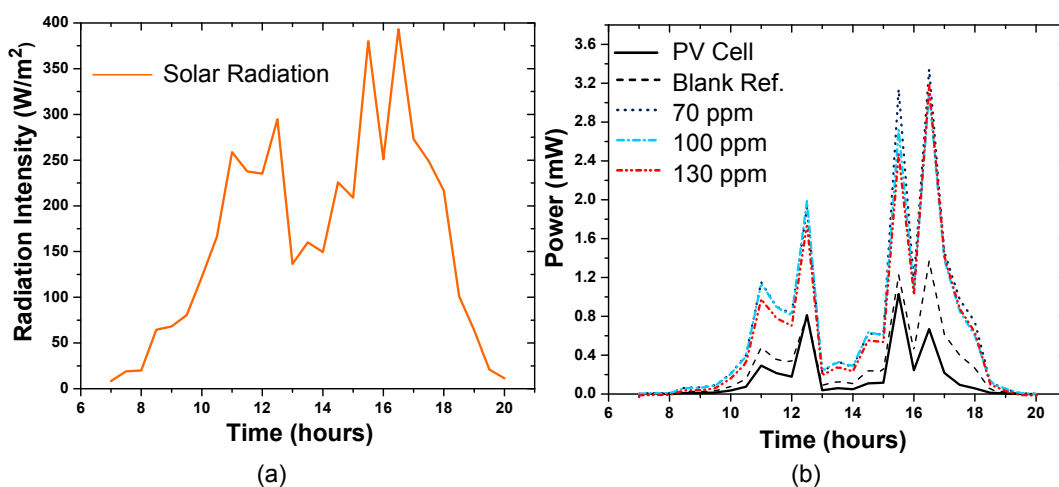


Figure 5.8: a) Average solar radiation throughout the day on 22 August 2018, b) Average power output from the LSC devices, blank reference and the stand alone PV cell throughout the day.

The edge output from the 100 ppm sample competes with the edge output from the 70 ppm sample. To understand this better the power conversion efficiency (PCE) of the LSC devices was plotted against the radiation intensity as seen in Figure 5.9. For lower radiation intensity (up to $200 W/m^2$) the PCE of both the 70 ppm and 100 ppm samples is approximately the same. 70 ppm sample average

PCE is 2.7 times the PCE of the bare PV cell. However, it should be noted that the performance of the bare PV cell is sub-optimal as it is placed vertically in the setup. The temperature of the PV cells attached to the various devices can be seen in Figure 5.9. The temperature increases on increasing the radiation intensity, as more light is incident on the PV cell and is lost as heat. For the LSC device a ten degree rise in temperature is observed on increasing the average radiation. Placing the PV cell horizontally and attaching the thermocouple to the waveguides can give more insight about the temperature variation in the waveguide and cells independently.

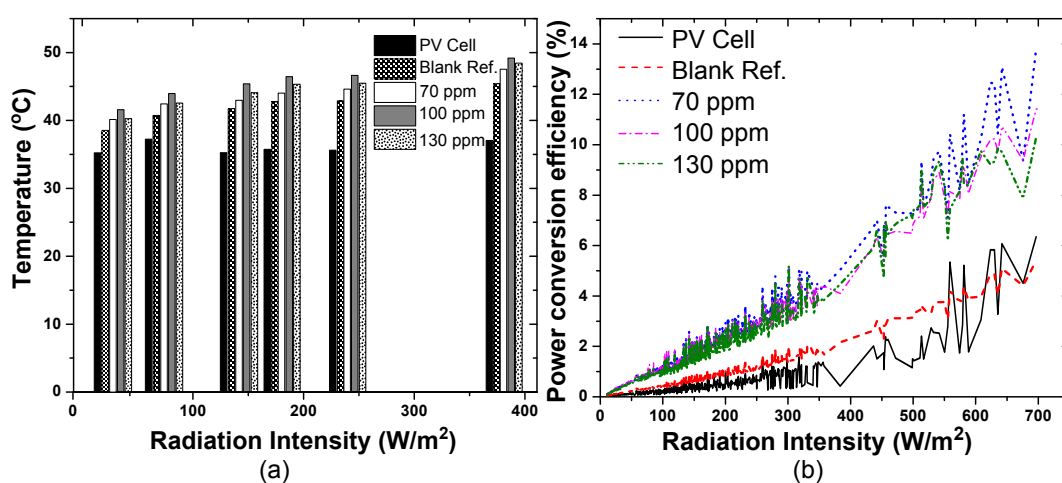


Figure 5.9: a) Average temperature of the PV cell attached to different LSC waveguides under different radiation intensity, b) Relative power conversion efficiency of the LSC devices on increasing the radiation intensity

5.4 Diffuse reflectors

As discussed in section 2.4, the amount of light trapped in an LSC is determined by the refractive index of the host matrix. For Silicone host matrix ($n=1.44$) the proportion of light lost through the back escape cone and therefore eventually recoverable is about 0.29. Metallic mirrors have been employed as the back reflector in LSC to improve the absorption of the dye (Goetzberger and Greube, 1977). The drawback of metallic mirrors is that they are not 100% reflective, the light has to encounter the rear surface many times before it reaches the edge and even at 5%(De

La Perrelle, Moss, and Herbert, 1963) losses the light reaching the edge would be less than 50%. Another option is to use a white scattering layer (Goldschmidt et al., 2009, Bailey et al., 2007, Debije et al., 2009) as a backside reflector for LSC. The diffuse back reflectors can have two consequences; i) photons that are not absorbed by the dye are reflected back into the waveguide at an angle that increases their mean path length thus increasing the probability of absorption. ii) Reflected photons that are incident on the LSC at a wide incident angle will be refracted into the waveguide at an angle close to the critical angle for TIR. These photons will subsequently reach the edge directly.

5.4.1 Titanium Dioxide nanoparticles for diffuse reflectors

TiO₂ nanoparticles were suspended into Silicone polymer to fabricate diffuse reflectors as discussed in section 3.4. A 500 microns thick aluminum sheet was used as a specular reflector. Four different concentration of TiO₂ nanoparticles was dispersed into the polymer to fabricate the reflectors. The total and scattering reflectance of the fabricated reflectors was measured using the integrating sphere setup as mentioned in section 3.3.1, the results of the reflectance measurements can be seen in Figure 5.10. TiO₂ absorbs light below 400 nm and that explains the sudden drop in the reflectance at 400 nm, whereas, the aluminum reflector reflects light in the UV region down till 300 nm. The maximum total reflectance of aluminum is 90% at 390 nm and drops to 80% at 790 nm before increasing again to 92% at 1000 nm. For the diffuse reflector the total reflectance increased on increasing the concentration of the TiO₂ nanoparticles in the film. Maximum reflectance (88%) at 500 nm is observed for the sample with 2 wt% doping concentration of TiO₂ nanoparticles.

It was found that on further increasing the concentration of the nanoparticles in the polymer resulted in the aggregation of the particles and an inhomogeneous sample as seen in Figure 5.11a. The integrated area for the diffuse reflector (2.5 wt%) and the aluminum sheet is approximately the same $\pm 3\%$. Two LSC waveg-

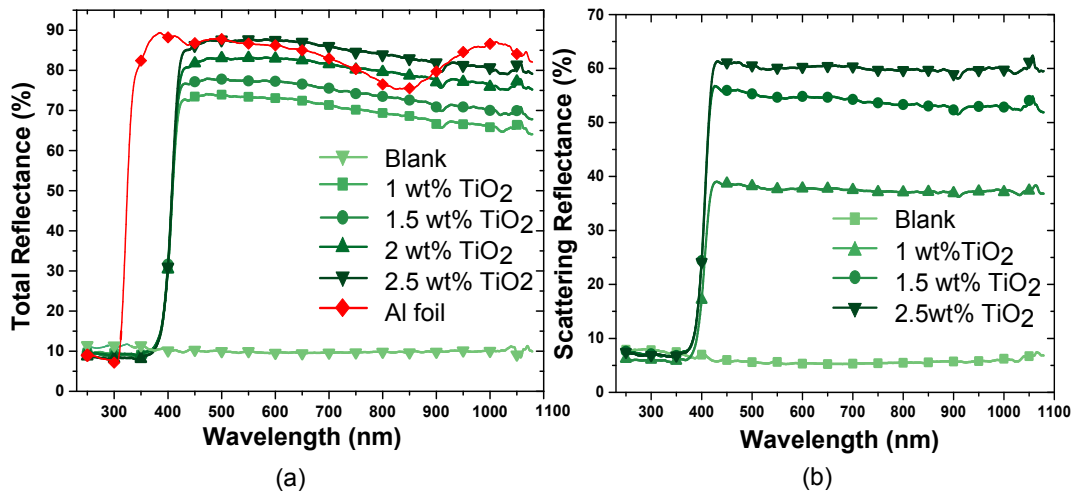


Figure 5.10: a) Total reflectance of diffuse reflector with increasing concentration of TiO_2 nanoparticles in Silicone, b) Scattering reflectance of the fabricated diffuse reflectors

guides with different doping concentrations of Red305 dye (30ppm and 70 ppm) were tested with the diffuse and specular back reflectors. The edge emission from the waveguides was measured using the edge emission setup mentioned in section 3.8.1. The reflectors were separated by an airgap (1 cm) from the waveguide, this position was fixed for the experiment. Full spectrum comprising of both UV and visible light was used as the light source. Two sets of measurements were taken for 1 cm and 2 cm beam spot size, this was achieved by moving the light source further away from the waveguide. The incident light beam on the waveguide with a diffuse back reflector can be seen in Figure 5.11b. The integrating sphere collects the light from the edge of the waveguide.

The edge emission spectrum obtained for the LSC waveguides with and without diffuse back reflectors can be seen in Figure 5.12. For both the concentrations an increase in the emission intensity is observed when employing the aluminium reflector and the diffuse reflector.

However, for the diffuse reflector an increase in the tail of the emission spectrum is also observed. The waveguides with the aluminium back reflector has significantly less edge emission than the diffuse back reflector. The reason for this is

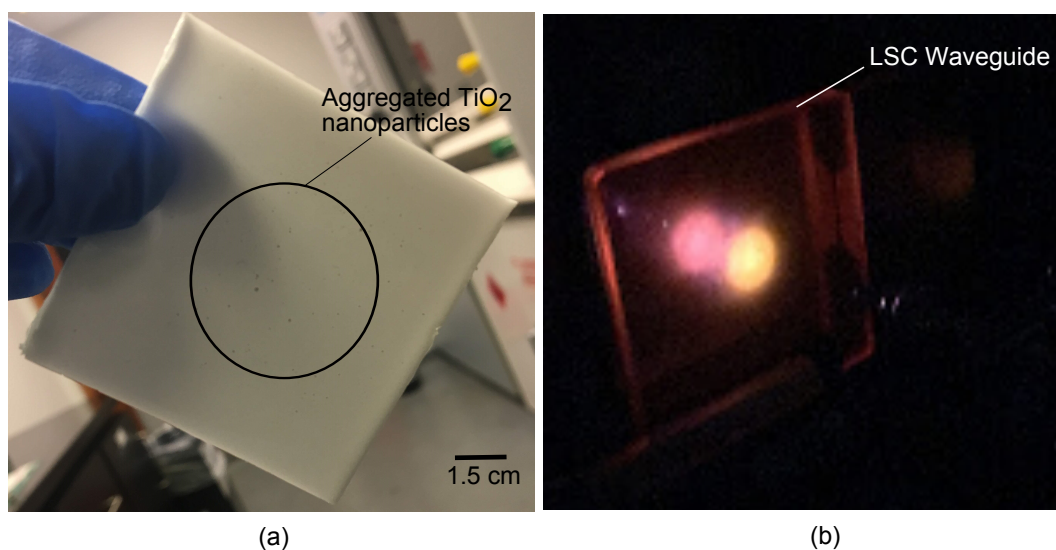


Figure 5.11: a) Aggregation of TiO₂ nanoparticles in the polymer at high concentrations. b) 1cm beam spot on the LSC waveguide with a diffuse back reflector.

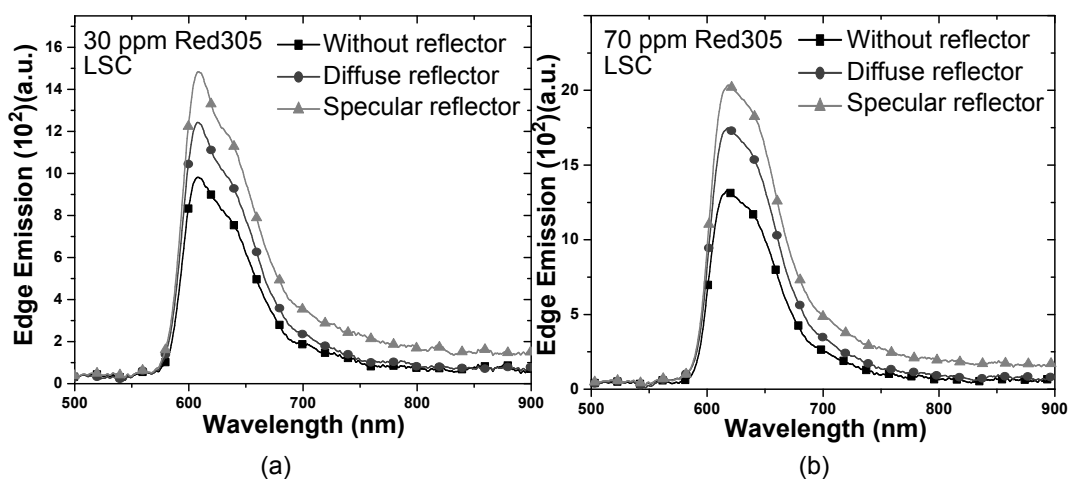


Figure 5.12: Edge emission spectra with and without back reflectors from LSC waveguides with doping concentration of a) 30 ppm and b) 70 ppm.

that the specular reflector is effective for only the wavelength range that is absorbed by the Red305 dye. All the light that is reflected back by the specular reflector but is outside the absorption range of the dye simply leaves the waveguide. However, the diffuse reflector can change the direction of the incoming light both within and outside the absorption range of the dye. The scattered radiation can directly reach the emission edge of the waveguide, and this results in the increase in the tail of the emission profile for the diffuse back reflectors.

The short range effect of the back reflectors was determined by comparing the integrated emission from all the measurements. The results for the different beam spot size can be seen in Figure 5.13. The edge emission output for the 70 ppm sample with the diffuse back reflector is 1.7 times higher than without any reflector. For the smaller beam spot size of 1 cm the increase in the edge emission with the diffuse back reflector is 1.3 times of the edge emission without the reflector. A slight increase (8%) in the edge emission is observed for the sample with the higher absorption coefficient. This result is in agreement with (Debije et al., 2009), where an increase in the edge output is observed on increasing the peak absorbance of the LSC waveguides. A 33% increase in the edge emission output is observed on increasing the beam spot size from 1 cm to 2 cm for the 70 ppm sample with the diffuse back reflector. Similarly a 20% in the edge emission is observed for the 30 ppm sample with a diffuse back reflector. A drawback of using TiO₂ NPs is that they aggregate in the matrix due to the weaker binding of the TiO₂ NPs to the polymer matrix. According to (Baudys et al., 2015) creation of better barriers to the photocatalytic mineralization process can help in increasing the lifetime of polymer films containing TiO₂ NPs.

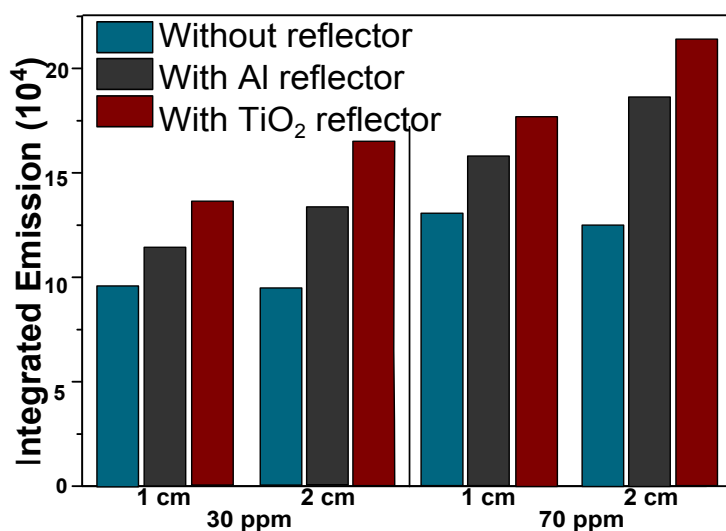


Figure 5.13: Integrated edge emission of the LSC waveguides with and without diffuse back reflector.

5.5 Conclusions

The compatibility of two types of fluorophores: Lumogen F Red305, Yellow083 dye and ZnCuInS/ZnS QDs was tested in Silicone polymer. Red305 dye formed aggregates in the polymer and that was evident by the higher calculated concentration values using the absorbance spectra. The dyes have a smaller Stokes' shift as compared to the QDs. However, Red305 dye had a high PLQY of 98 % in the host matrix, whereas the QDs had a PLQY of 20%. This makes Red305 dye a suitable candidate for a fluorophore in LSC and PLSC devices. Prior to introducing MNPs in the LSC waveguides to fabricate PLSC devices it is important to optimize the concentration of the Red305 dye for a $4.5 \times 4.5 \times 0.3 \text{ cm}^3$ waveguide.

Samples with varying concentration of the dye (10-160 ppm) were fabricated. The absorption intensity increased with concentration, however the linear fit of the integrated absorption is less than zero when the concentration is zero. This might be due to the overestimation of absorption intensity as the dye molecules form aggregates in the Silicone polymer. The total emission from the LSC waveguides was measured by placing the waveguide inside the integrating sphere. An increase in the emission intensity was observed on increasing the dye doping concentration. The emission profile changed for high doping concentration (above 50 ppm) and a red-shift from $\sim 602 \text{ nm}$ to $\sim 636 \text{ nm}$ in the emission peak was observed for 10 ppm and 160 ppm doping concentration, respectively. These changes observed in the emission spectra can be attributed to the re-absorption losses in the waveguides. This result was also corroborated by measuring the emission from the edges of the waveguide. Similar change in the edge emission profile and red-shift in the emission peak was observed. The integrated edge emission varied non-linearly with the dye doping concentration in the waveguide. The edge emission dropped after 100 ppm doping concentration. 70 ppm dye doping concentration was used in PLSC devices.

Outdoor electrical characterization of different LSC devices, blank reference and a PV cell was carried out to measure the relative power output from the de-

vices. A 2.7 times increase in the average PCE is observed for optimized LSC device as compared to the bare PV cell. A maximum power conversion efficiency of 13.8% was achieved for the 70 ppm sample with a radiation intensity of 696 W/m^2 taken from the pyranometer reading. Bare PV cell has a lower ($< 3^\circ\text{C}$) temperature than LSC device possibly due to the position of the cell.

TiO₂ nanoparticles were used to fabricate diffuse reflectors. 2.5 wt% of TiO₂ nanoparticles had comparable integrated total reflectance as the aluminium sheet that was used as a specular reflector. Upto 60% of the reflectance from the TiO₂ reflectors is diffuse. The edge emission for the LSC waveguide with a diffuse reflector is up to 1.7 times higher than without any reflector. With the diffuse reflector an increase in the tail of the emission spectrum was observed. A 33% and 20% increase is observed in the edge emission of 70 ppm and 30 ppm sample when the beam spot size is increased from 1 to 2 cm, respectively.

Chapter 6

Plasmonic Luminescent Solar Concentrator

The Red305 dye doping concentration was optimized for a $4.5 \times 4.5 \times 4.5 \text{ cm}^3$ size LSC in chapter 5, in this chapter MNPs, are dispersed into the host matrix to fabricate PLSC. The first half of the chapter deals with influencing the plasmonic coupling in the PLSC device through spacing and spectral overlap between the Au@Ag NCs and Red305 dye. The spacing between Au@Ag NCs and Red305 dye was controlled by the doping concentration of Au@Ag NCs for acquiring a homogeneous sample. The optical performance of PLSC waveguides was investigated through edge emission measurements of the plates while varying the doping concentration of Au@Ag NCs. The optical measurements were also corroborated by the electrical characterization of the PLSC devices. The latter part of the chapter deals with the outdoor characterization of PLSC device in comparison with the LSC device and a bare PV cell. The devices were studied for one month in Irish weather of rain, diffuse and direct light conditions. The diffuse reflectors fabricated in chapter 5 were used as a rear reflector with the PLSC device.

6.1 Red305 dye and Au@Ag NCs Plasmonic Luminescent Soar Concentrator

Re-absorption losses are inevitable at high Red305 doping concentrations in the LSC device (Olson, Loring, and Fayer, 1981). Introducing the MNPs can influence the fluorescence of the Red305 dye thus modifying the edge emission from the device. The excitation and emission rate of the fluorophore can be influenced by matching the plasmon band of the MNP to the absorption and emission band of the fluorophore respectively (Liu et al., 2013). The plasmonic coupling between an MNP and the fluorophore depends on various factors such as the spacing between the fluorophore and the MNP, the spectral overlap of the plasmon band with the absorption/emission band of the fluorophore, the position of the surface plasmon resonance of the MNP. Therefore, to optimize the plasmonic coupling between the fluorophore and MNP it is essential to match the SPR band of the MNP to either the absorption or emission band of the fluorophore. Moreover, the spacing plays a crucial role in influencing the emission enhancement or quenching. The spacing between the MNPs and fluorophore can be controlled either by employing a spacer such as Silica of known thickness around the MNP or controlling the concentration of the MNPs in the device. In this work, these parameters have been controlled for a PLSC device comprising of Red305 dye and Au@Ag NCs.

As pointed out in section 4.1.2 the Au@Ag NCs aspect ratio and therefore their SPR band position could be changed by varying the silver ion content in the growth solution. Au@Ag NCs sample 5 had a longitudinal peak at ~552 nm and transverse peak at ~461 nm in DCM, both the peaks are of comparable height. The NCs have an aspect ratio of 2 ± 0.2 . The absorption and emission spectra of the Red305 dye sample (70 ppm) along with the extinction spectrum of the Au@Ag NCs can be seen in Figure 6.1. The red-region represents the overlap between the SPR bands and the absorption/emission spectra of Red305 dye. A complete spectral overlap of the absorption band and the plasmon bands is observed, the offset of the longitudinal SPR peak of the Au@Ag NCs from the emission peak of the red dye was found to

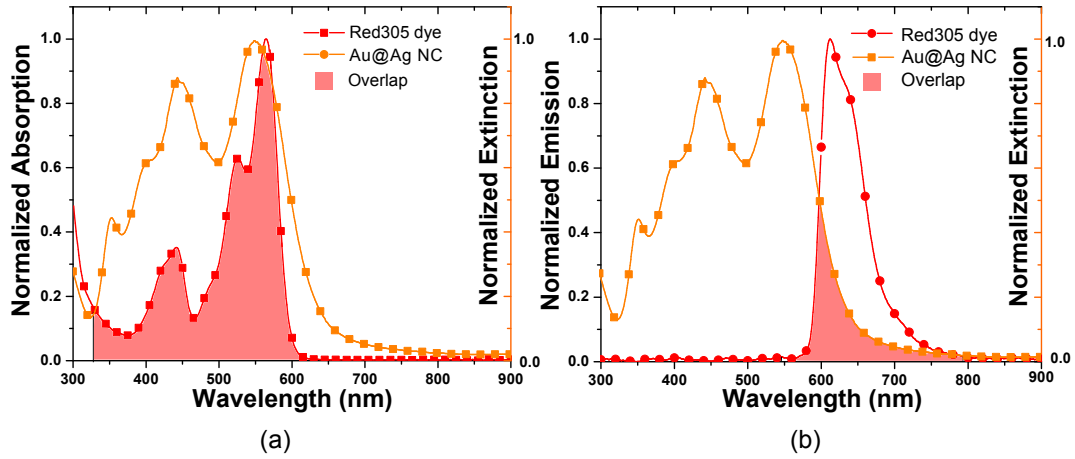


Figure 6.1: Normalized a) absorption and extinction spectra spectra of Au@Ag NCs and Red305 dye, b) emission and extinction spectra of Red305 dye and Au@Ag NCs showing the overlap between the respective spectra.

be 19.6 eV. A slight overlap of the plasmon band with the emission band can be observed.

PLSC waveguides with varying concentration of Au@Ag NCs were fabricated. The final concentration of the Au@Ag NCs in the waveguide was calculated as discussed in section 4.4. Six PLSC waveguides of size $4.5 \times 4.5 \times 0.3 \text{ cm}^3$ with Au@Ag NCs concentration ranging from 0.6 ppm-14 ppm was fabricated in the same manner as a LSC waveguide (section 3.7). PLSC waveguide containing 0.6 ppm Au@Ag NCs doping concentration can be seen in Figure 6.2b. The absorbance of the PLSC waveguides was measured using the UV-VIS spectrometer as mentioned in section 3.3. A blank solid Silicone polymer of the same dimensions as the PLSC waveguide was used as a reference for the absorption measurements Figure 6.2a. The absorption intensity increases on increasing the Au@Ag NCs concentration in the waveguide.

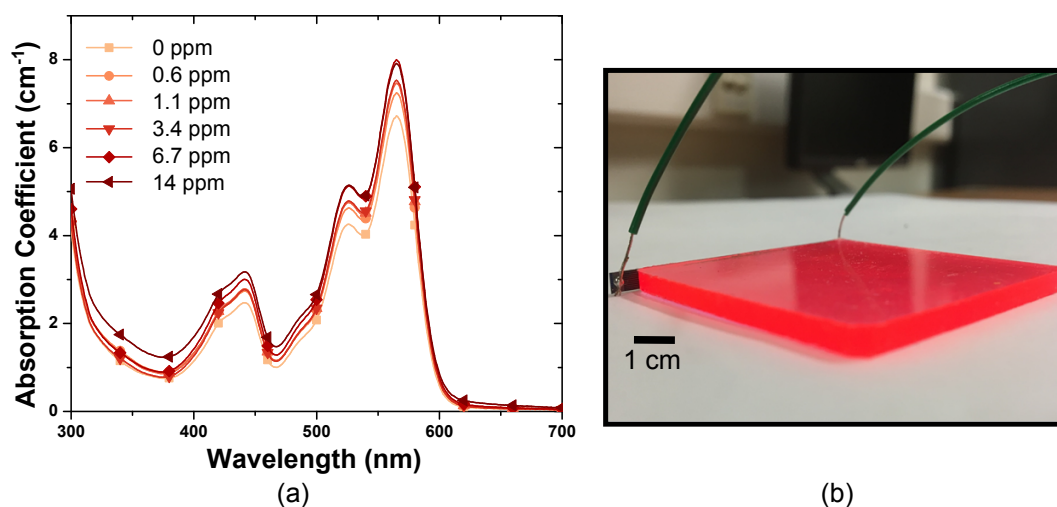


Figure 6.2: a) Absorption spectra of PLSC waveguides with increasing concentration of Au@Ag NCs, b) Photograph of a PLSC waveguide containing 0.6 ppm Au@Ag NCs concentration.

6.2 Edge emission measurement of Plasmonic Luminescent Solar Concentrator

To understand the effect of the addition of Au@Ag NCs in the waveguide, the edge emission from the PLSC waveguides was taken using the setup mentioned in section 3.8.1. A direct beam spot of 1.5 cm was illuminated at the centre of the waveguides and the edge emission was collected using the integrating sphere. It was made sure that the beam spot was of the same size for all the measurements by fixing the position using an XY translation stage. The edge emission spectra can be seen in Figure 6.3. An increase in the edge emission output is observed for the PLSC waveguide. There are mainly three mechanisms that could result in the Au@Ag NCs related emission enhancement.

In the absence of MNP, the fluorophores feel incident electric field at the excitation wavelength and emit light at the emission wavelength. The extent of absorption is determined by the absorption cross-section which is usually a fraction of the geometrical cross-section of the fluorophore. When an MNP is in the vicinity of the fluorophore the absorption cross-section of the fluorophore increases due

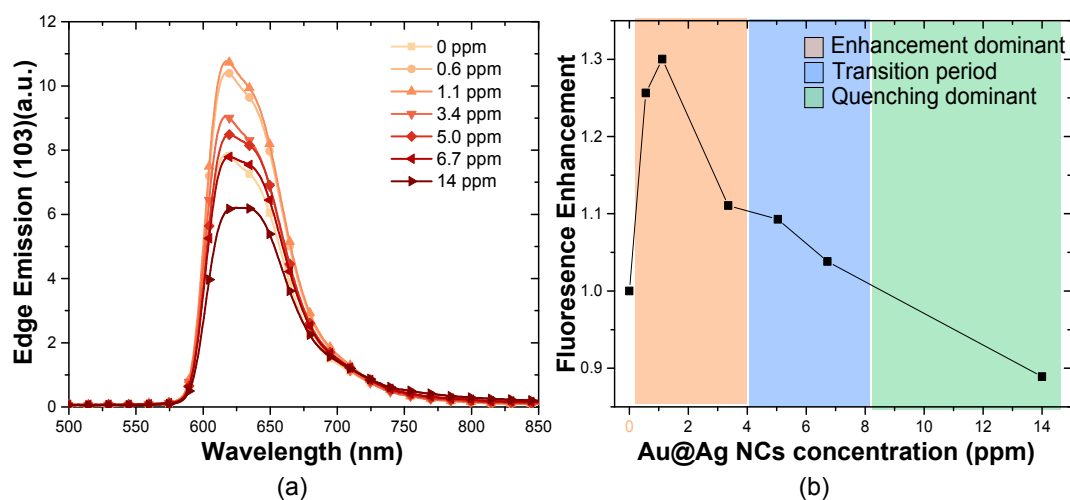


Figure 6.3: a) Edge emission spectra of PLSC layers with increasing Au@Ag NCs concentration taken using an integrating sphere. (b) Fluorescence enhancement in PLSC layers as a function of NC concentration normalized to the 0 ppm sample

to the enhancement in the local electric field around the fluorophore (Lakowicz, 2001). This enhances the excitation rate of the fluorophore. As discussed in section 2.10 near field enhancement is frequency-dependent and the highest excitation rate is achieved when the SPR band directly overlaps the absorption spectrum of the fluorophore. The spectral overlap holds for Au@Ag NCs and Red305 dye as seen in Figure 6.1a.

The radiative rate of a fluorophore is determined by the absorption coefficient of the fluorophore, thus it is invariable for a given fluorophore. Thus the PLQY of a fluorophore can be increased by decreasing the non-radiative decay rate of the fluorophore, one such way is decreasing the temperature. However, when an MNP is placed in the vicinity of a fluorophore, the MNP can increase the radiative decay rate by addition of a new channel. This increment in the radiative decay rate can increase the QY of the fluorophore as discussed in section 2.10. Maximum enhancement is achieved when the SPR band of the MNP overlaps the emission spectrum of the fluorophore. In this work, Red305 dye is the fluorophore and it has nearly unity QY, thus the addition of a new radiative channel due to the Au@Ag NCs does not have any effect on the QY.

Thirdly, the far-field coupling of the fluorophore emission to the MNP scattering can enhance the fluorescence. The far-field enhancement is most prominent when the scattering band of the MNP matches the emission spectrum of the fluorophore. The excited fluorophore acts as the donor and transfers its energy to MNP (acceptor). Scattering is dominant for MNPs with dimensions larger than 60 nm, in this work, Au@Ag NCs had a smaller size therefore, the role of this mechanism in emission enhancement is limited.

The magnitude of all the above-mentioned mechanisms depends on the distance between the fluorophore and the MNP and the orientation of the dipole moment with respect to the MNP. In this work, the concentration of the Au@Ag NCs in the waveguide is an indication of the distance between the Red305 dye molecule and Au@Ag NCs. The effect of Au@Ag NCs concentration on the edge emission of the PLSC waveguides can be seen in Figure 6.3a. It can be seen that the emission spectra are sensitive to NC concentration. A continuous change in the edge emission intensity with respect to NC doping concentration is observed for PLSC waveguides. Above 1.1 ppm NCs doping concentration a decrease in the edge emission is observed. This decrease in emission can be attributed to the increase in quenching of the fluorescence. Quenching dominates enhancement due to an increase in the probability of non-radiative transfer of energy from the excited fluorophore to the MNP (Kulakovich et al., 2002). The maximum edge emission from PLSC is a balance between the enhancement and quenching effect (Sakr and Kana, 2014).

The integrated emission of the PLSC waveguides was calculated from 400-900 nm and it was used to find the fluorescence enhancement factor for the PLSC waveguides normalized to the layer with 0 ppm of NCs. Fluorescence enhancement as a function of Au@Ag NCs concentration is presented in Figure 6.3b. At lower NC concentration (such as 0.6, 1.1 ppm) fluorescence enhancement dominates over quenching (light red region). For 6.7 ppm sample, there is hardly any enhancement in fluorescence, this has been shown as the transition period (blue region) and it de-

depends on the dye concentration. At high concentrations such as 14 ppm quenching dominates over enhancement due to NCs (green region). Enhanced electric field decays exponentially from NC surface, therefore, only red dye molecules in the range of this enhanced field are plasmonically coupled to the MNP. This explains the dominance of quenching over the enhancement of the emission due to high NC concentration in the PLSC layers, even though those layers have higher absorption intensities. As NC doping concentration increases there is a high probability that Au@Ag NC-red dye pair is in the quenching domain. The high magnitude of enhancement for such a low concentration is due to the enhanced excitation rate of the fluorophore and also due to the maximum overlap of the Red305 dye absorption spectra with the extinction spectra of NCs. These results show 30% Red305 dye fluorescence enhancement for the 1.1 ppm NC concentration sample. This proves that the concentration of red dye can be decreased without compromising on the emission of an LSC, by embedding noble MNPs in the LSC. This method can reduce re-absorption losses in an LSC that mainly occur due to the high concentration of fluorophores in the device. Re-absorption losses are one of the main loss mechanisms that prohibit the creation of efficient large scale devices, therefore introducing noble MNPs can help in future developments of these devices. Another added advantage is to prevent the aggregation of the fluorophore in the polymer at high concentration that can lead to Rayleigh scattering of the incident radiation.

6.3 Indoor performance of plasmonic luminescent solar concentrator

The electrical characterization of three samples was conducted to validate the edge emission results. A blank silicone encapsulant polymer sample was used as a reference and the current generated from these samples with respect to the voltage can be seen in Figure 6.4a. All the samples were measured three times and an average of those measurements has been plotted in Figure 6. The standard deviation be-

tween the measurements was calculated to be less than 3%. The 1.1 ppm sample power conversion efficiency was found to be 1.2 times higher than the power conversion efficiency of 0 ppm sample. The maximum power obtained for each PLSC waveguide with respect to voltage can be seen in Figure 6.4b. It should be noted that blank reference sample also produces up to 1 mW power output. The power output might be because of light incident near the edge of the sample where the PV cell is attached. The incident light directly reaches the PV cell due to the short distance between the point of incidence and the cell and due to scattering a small fraction of incident light can go through TIR and reach the solar cell attached at the edge.

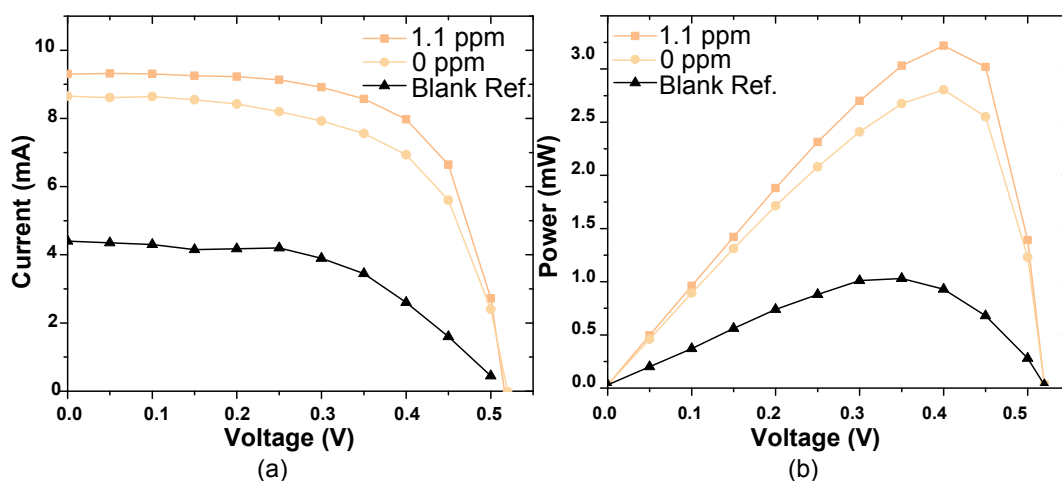


Figure 6.4: a) Current generated from PLSC device as a function of voltage relative to a blank reference and simple LSC device with Si solar cell attached to the edge, b) The power curve of the PLSC device as a function of voltage and depicting the maximum power for each sample.

6.4 Outdoor performance of plasmonic luminescent solar concentrator

The performance of PLSC device in outdoor conditions can help to understand its feasibility in a northern European climate. PLSC device with the optimized Au@Ag NCs concentration (1.1 ppm) was tested along with an LSC device with 70

ppm Red305 dye doping concentration. A blank Silicone waveguide and a bare PV cell were used as a reference. The outdoor setup can be seen in Figure 6.5. The bare PV cell was placed in a horizontal position. The horizontal bare PV cell will yield the maximum power conversion efficiency possible and its comparison with the PLSC device can give a better comparison. The setup was covered by a low iron glass similar to the one mentioned in section 5.3, and the temperature of the PV cells and the waveguides was recorded by using K-type thermocouple. The data was recorded at minute time by the data logger over a period of 40 days from 28th June 2019 to 15th August 2019. As the outdoor setup was protected by the low iron glass, data could be collected for rainy conditions.

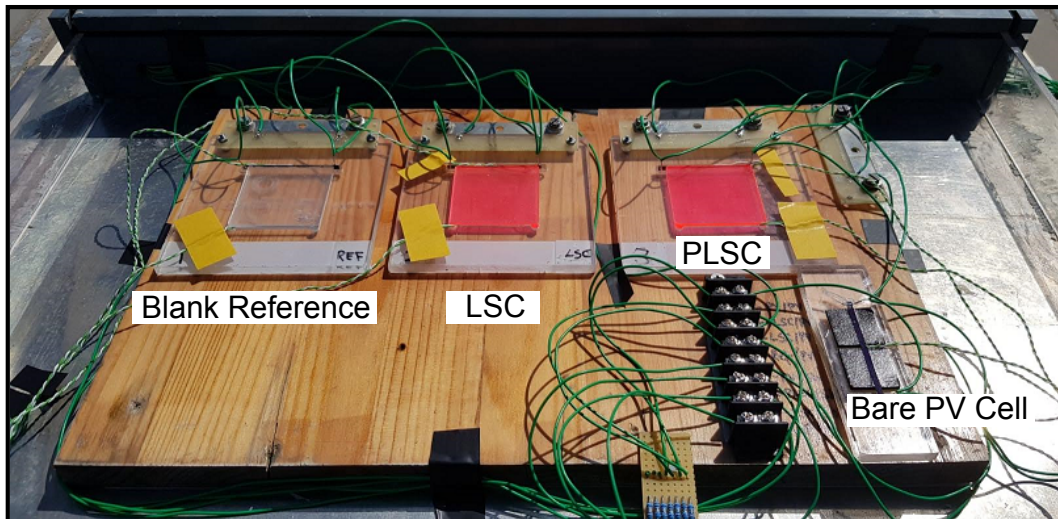


Figure 6.5: Photograph of the outdoor setup consisting of PLSC and LSC devices.

The data from a clear sunny day and a cloudy day with varying cloud cover is compared in this work. Measured solar irradiance on a sunny day (3rd July 2019) rated as 1 okta and a cloudy day (30th June, 2019) with considerable variation in the cloud cover from 3 to 6 oktas can be seen in Figure 6.6a,b. Sunrise at this location is at 5:00 and sunset is at 21:56. As can be seen from Figure 6.6a a drop in solar irradiance from 10:00 to 11:00 on 3rd July is due to a passing cloud. The edge power output from the devices and the references can be seen in Figure 6.6c,d. It is observed that the PLSC device performs on an average approximately 1.2 times

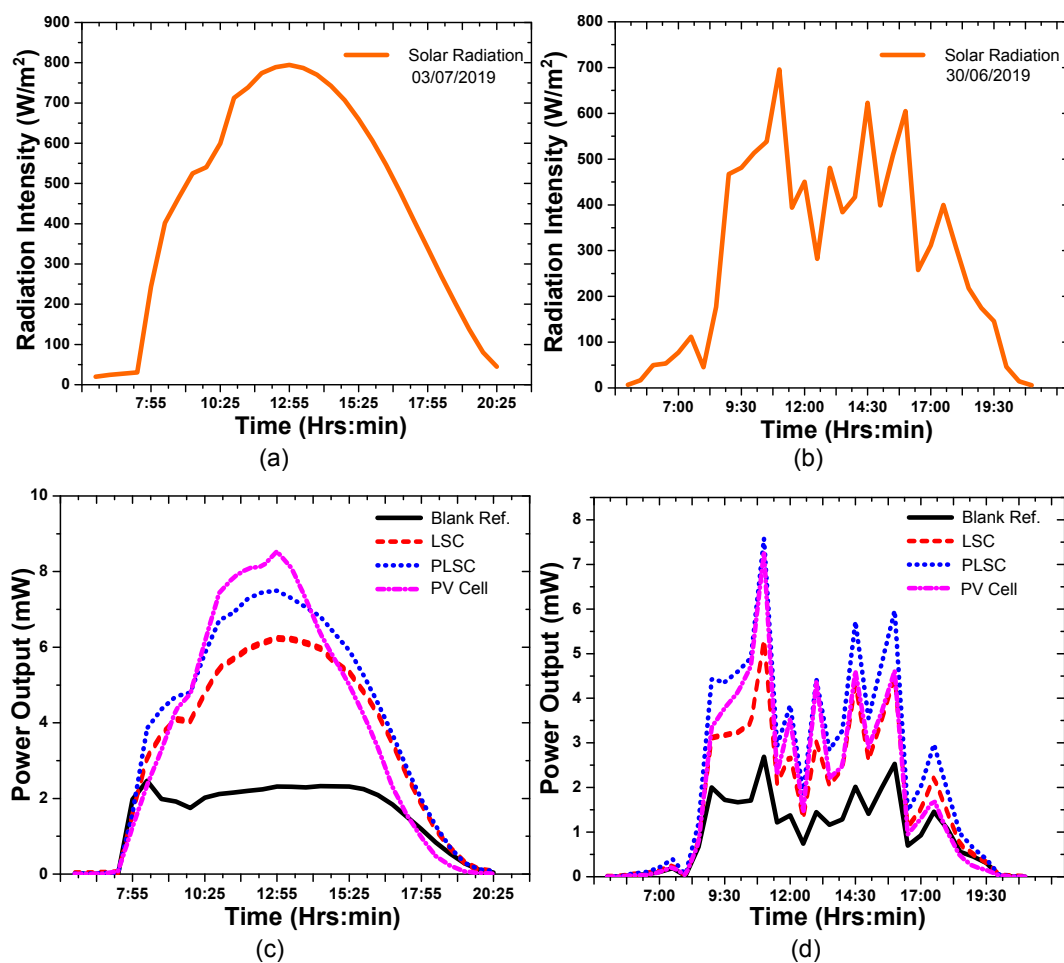


Figure 6.6: Solar irradiance from sunrise to sunset on a) 3rd July 2019 when average cloud cover was 1 oktas and b) on 30th June 2019 when the average cloud cover was 6 oktas. Average edge power output from the PLSC, LSC devices and the references on a) 3rd July 2019 and b) 30th June 2019.

better than the LSC device in both sunny and cloudy conditions.

On a sunny day when the direct to diffuse radiation ratio is high, the bare PV cell performs better than the PLSC device from 11:00 to 14:00, the PLSC device performance overtakes the bare PV cell when the solar disc is closer to the horizon at morning and evening hours. This shows a dependence of the power output on the position of the sun. For a cloudy day, the PLSC device outperforms the bare PV cell throughout the day. For the same radiation intensity when cloud covers the solar disc the fraction of diffuse light increases significantly, the spectral distribution of diffuse light is different from direct light (Hisdal, 1987). Short-wavelength

light is scattered more efficiently because of the cloud cover and that can explain the higher edge output of the PLSC device than the bare PV cell on a cloudy day. In absolute terms, the power output will be higher on a sunny day as compared to a cloudy day because of a higher number of incident photons.

6.4.1 Effect of sun's position on performance

As mentioned before PLSC device performs better than the bare PV cell during the morning and evening hours of both sunny and cloudy days as shown in Figure 6.7. In the Figure 6.7 the day has been divided into three regions morning, afternoon and evening based on the sun's altitude. Throughout the day the sun changes its position in the sky, at sunrise and sunset the altitude is zero degrees. The sun's daily maximum altitude is called solar noon and does not typically coincide with clock noon. On 30th June 2019 and 3rd July 2019 the solar noon is at 13:28 at an altitude of 60° . Morning has been considered the time when the sun's altitude increases from 0 to 30 degrees. The afternoon is when the sun's altitude changes from 30 to 60 degrees and then back to 30 degrees. The evening duration is exactly similar to the morning when the sun's altitude changes from 30 to 0 degrees at sunset.

A continuous change in the ratio of efficiency of PLSC device to the PV cell is seen on a sunny day (3rd July 2019). The ratio of efficiency is higher (orange region) when the sun's altitude is lower than 30 degrees for both morning and evening as compared to afternoon (yellow region). The drop in the ratio of efficiency in the morning of 3rd July 2019 can be attributed to the passage of clouds at that time. Diffuse radiation comes from all the angles while direct follows the path of the solar disc. When the solar disc is closer to the horizon, the sun rays travel a longer distance to reach the device thus getting more scattered and diffuse as compared to when the sun is at the zenith. A similar trend is observed on a cloudy day (30th June 2019), although due to the presence of clouds throughout the day the change in ratio is not as continuous as on the sunny day. For countries lying at high latitudes

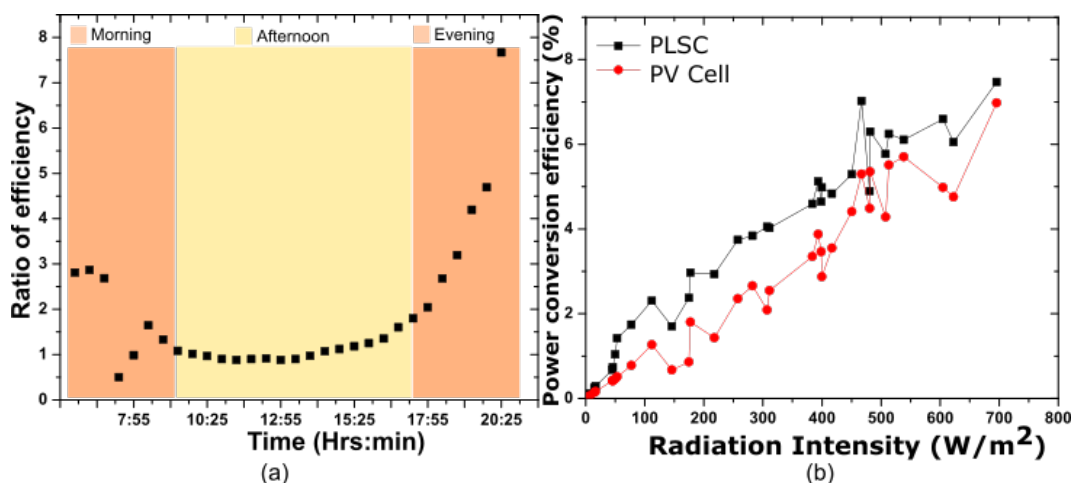


Figure 6.7: a) Ratio of power conversion efficiency of PLSC device to the bare PV cell on 3rd July 2019. The time has been divided into three regions based on the sun's altitude in the sky. and b) Power conversion efficiency of PLSC and PV cell with respect to irradiation intensity on 30th June 2019.

(such as most of the European countries) the solar disc will be closer to the horizon for a longer duration than the countries near the equator. These results show the feasibility of the PLSC device in such countries.

6.4.2 Effect of light intensity on performance

The efficiency of the PLSC device and the bare PV cell with the radiation intensity on both the days is shown in Figure 6.8a,b. The efficiency of solar cells decreases with a decrease in the radiation intensity (Herteleer, Cappelle, and Driesen, 2012). However, it is observed in Figure 6.8a that the slope of the PLSC efficiency trend is lower than the slope of the PV cell output trend. This higher efficiency of PLSC device in low light levels is explained by its performance improvement in morning and evening time of the day. The PV cell's performance is negatively impacted when they are hot (Davis, Fanney, and Dougherty, 2001; Raga and Fabregat-Santiago, 2013). It was observed that above 400 W/m² PV cells attached to the PLSC or LSC waveguide had a temperature lower than the bare PV cells as shown in Figure 6.8c,d. The maximum temperature difference between the PV cell attached to the PLSC waveguide and bare PV cell is 7°C and 11°C on the cloudy day

and sunny day respectively. Thus, the impact of the higher radiation on PV cell attached to the PLSC waveguide was lower than the bare PV cell. The temperature difference between the PLSC waveguide and PV cell attached to the waveguide is 2°C . These results show that the PLSC waveguide will be less susceptible to spikes in the radiation intensity as compared to traditional PV cell. This can prove advantageous for large scale installations as it can reduce the strain on the grid (Ahmed, Miyatake, and Al-Othman, 2008; Daud, Mohamed, and Hannan, 2014). It should be noted that the ambient temperature was less than 20°C at peak position of the sun.

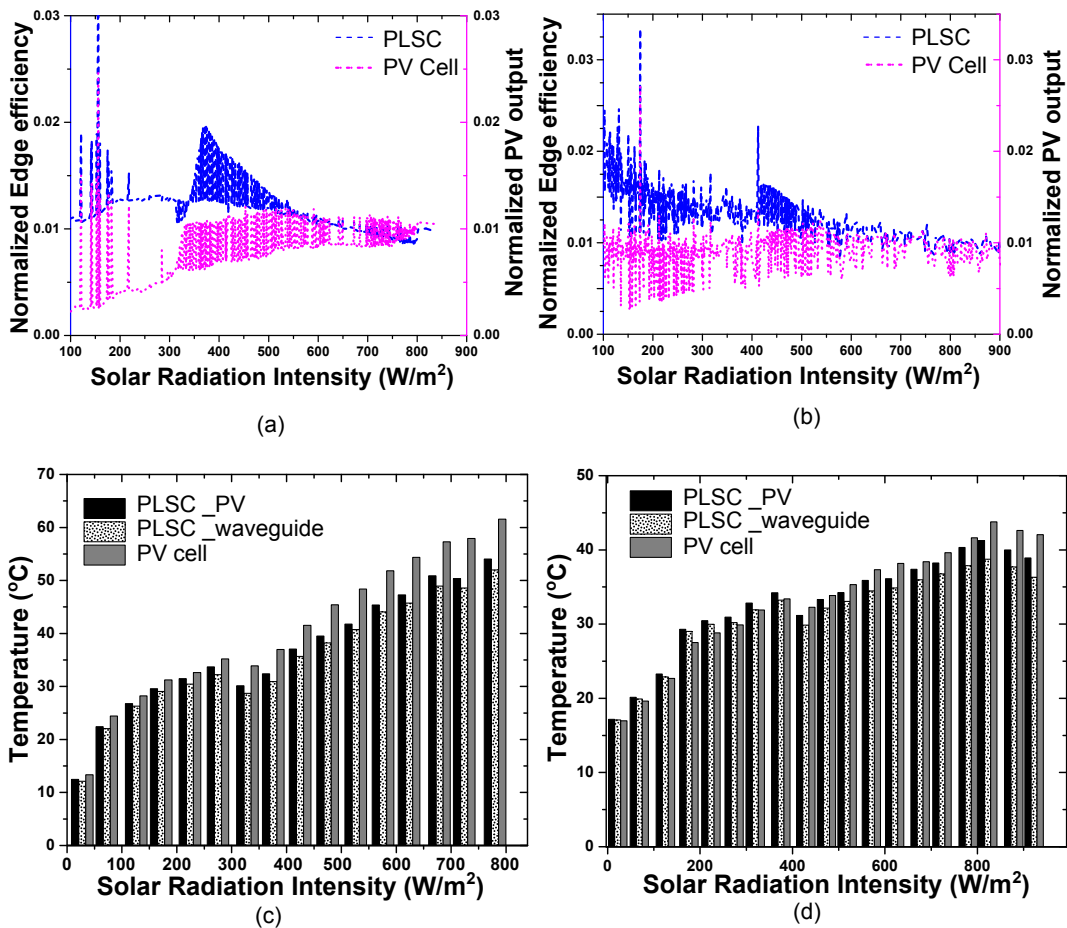


Figure 6.8: Normalized power conversion efficiency variation of PLSC device and bare PV cell on a) sunny day 3rd July 2019 and b) cloudy day 30th June 2019. Variation of the temperature of PV cell attached to PLSC, bare PV cell and PLSC waveguide on a) sunny day 3rd July 2019 and b) 30th June 2019.

6.4.3 Effect of diffuse reflector on performance

The diffuse reflector fabricated as mentioned in section 5.4.1 with 2.5 wt% doping concentration of TiO_2 nanoparticles was used as a rear reflector. The diffuse reflector was placed at a distance of 1 cm from the PLSC waveguide in the outdoor setup. Data from the LSC waveguide without a reflector and the PLSC device with the rear reflector was collected for three days. All three days had cloud cover, therefore, the results could not be compared with direct solar radiation. In this work data of 14th August 2019 has been shown, there was 7-8 oktas of varying cloud cover and intermittent rainfall. The sunrise and sunset time is 6:02 and 20:55 respectively. The solar irradiance and average power output are shown in Figure 6.9. A 23% increase is observed in the average power output of PLSC as compared to LSC device without any reflector. This shows an increase of almost 5% due to the reflector. It is possible that the higher ratio of diffuse light due to the cloud cover is scattered more by the reflector than direct light.

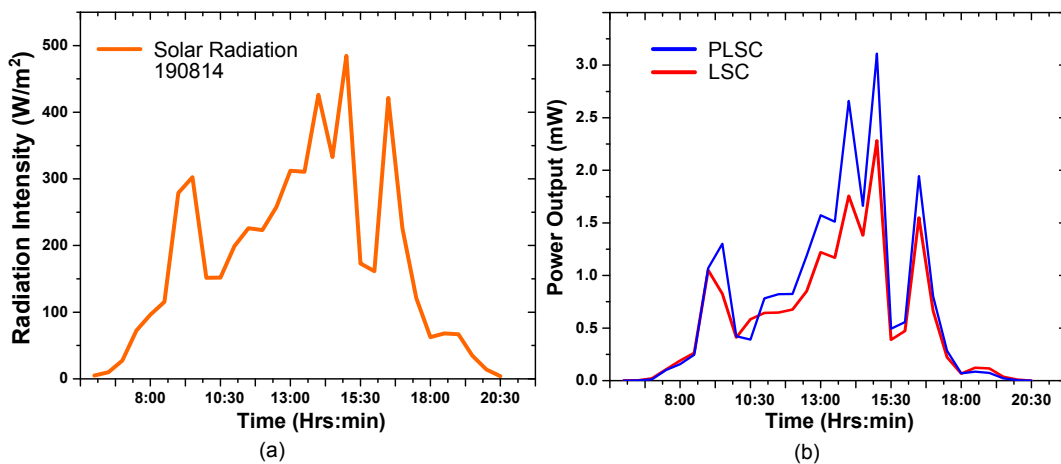


Figure 6.9: a) Solar radiation on 14th August 2019 with cloud cover rated 7-8 oktas with intermittent rain. b) Average power output of LSC and PLSC devices with reflector from sunrise to sunset.

6.4.4 Seasonal performance of PLSC device

In the previous section 6.4.1, the difference in the performance of a PLSC device in comparison to a blank PV cell on a clear summer day and a cloudy summer day

is illustrated. On a clear summer day, the PV cell outperforms the PLSC device, however, on a cloudy summer day the PLSC device has a higher power output than a PV cell as seen in Figure 6.6. The higher performance of PLSC device can be attributed to higher percentage of diffuse radiation on a cloudy day. It is important to see how the performance differs in summer and winter months as the amount of diffuse radiation is higher during winter months in Ireland .

The data collected for the whole month of July was used to plot the average hourly power output from the PV cell and PLSC device. December corresponds to the month with the lowest irradiance sum, the average hourly spectral irradiance data for December is taken from (*SolarEuropa PVGIS*). It is observed that the highest average solar irradiance (476 W/m^2 and 127.95 W/m^2) is around noon for July and December as shown in Figure 6.10a, c, respectively.

For both the months the shape of the output power curve of the PLSC device closely follows the variation in spectral irradiance, as can be seen from Figure 6.10b, d. This is similar to the observation for single days in the previous section 6.4.1. The power output of the PLSC device is higher than the PV cell in December, on an average the PLSC gives 1.6 times higher power output than the PV cell in December. As compared to July, the PLSC device performs 45% better than the PV cell in December. This shows the feasibility of PLSC device in winter months.

Spectral data on an hourly basis for both the months was used to determine the monthly energy yield. The monthly energy yield of the PLSC device is calculated to be 10.80 kWh/m^2 and 1.37 kWh/m^2 for July and December, respectively. Under STC the PV cell used in this work has a maximum power output of 28.5 mW. Following a simple method (Sark, 2007) the energy yield of this c-Si cell can be calculated. The PV cell has an energy yield of 23.97 kWh/m^2 and 3.04 kWh/m^2 for July and December, respectively. The cell generates 2.2 times the energy of the PLSC device. However, it should be noted that the temperature effects are not taken into account. Despite the higher energy yield of state-of-the-art silicon solar cell over a horizontally placed PLSC device, the PLSC device can be a good alternative over a

conventional PV in a BIPV setting.

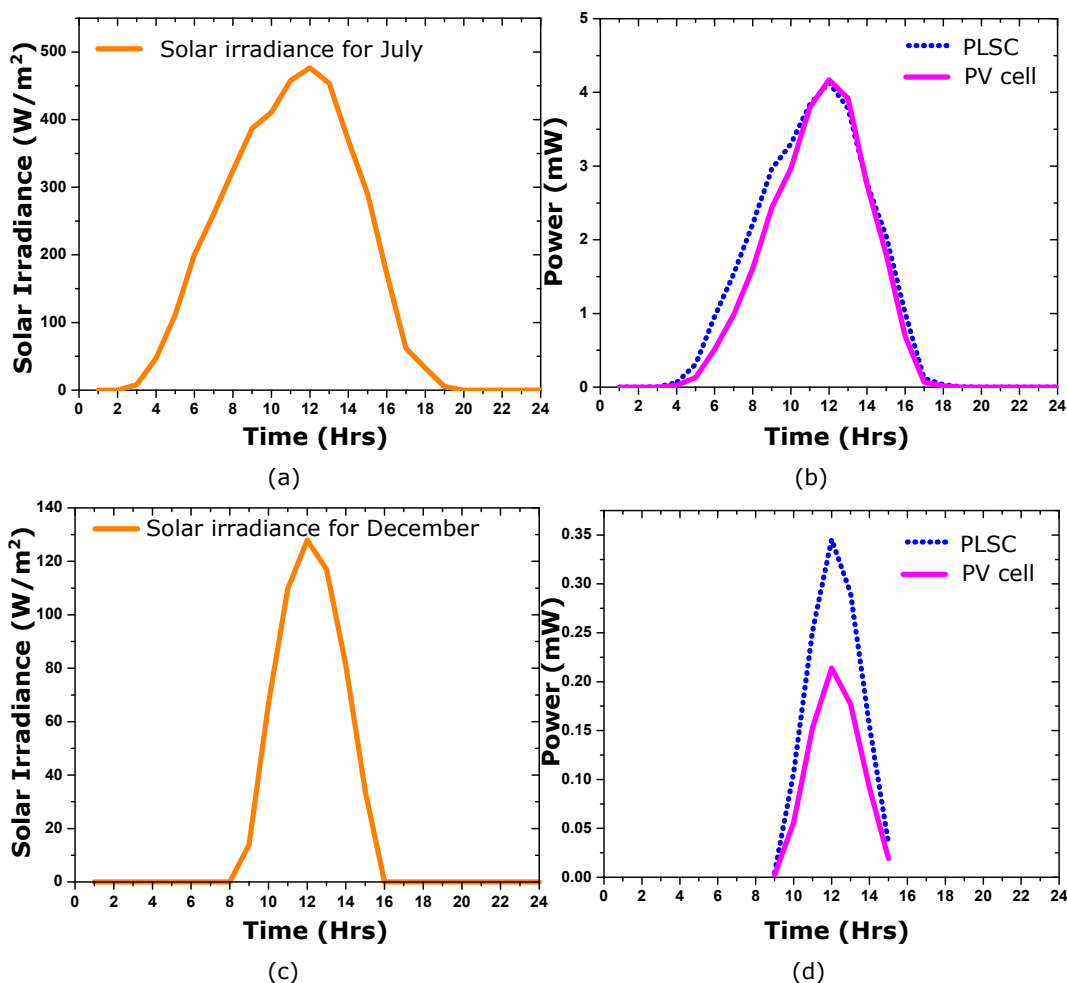


Figure 6.10: a), c) Daily average of solar irradiance for the months of July and December, respectively. b), d) Average power output of the PV cell and PLSC device for July and December, respectively.

Conclusions

This chapter investigated a PLSC device comprising of Red305 dye and Au@Ag NCs. The synthesized Au@Ag NCs from chapter 4 were used to ensure a maximum overlap with the absorption spectra of Red305 dye. The position of the longitudinal SPR band of NCs was blue-shifted with respect to the emission peak of Red305 dye. Plasmonic properties of silver were successfully exploited to increase the edge emission of PLSC. The spacing between the NCs and the dye was controlled by

changing NCs concentration in the PLSC device. Different NC concentrations (0.6-14 ppm) along with (70 ppm) red dye were dispersed in a Silicone polymer to fabricate $4.5 \times 4.5 \times 4.5 \text{ cm}^3$ PLSC devices. The maximum edge emission enhancement was observed for 1.1 ppm NC concentration, the main factor contributing to the edge emission enhancement was the increase in the excitation rate of the Red305 dye via near field enhancement. As the Red305 dye has almost unity PLQY the increase in edge emission cannot be attributed to the PLQY increase due to MNPs. The size of Au@Ag NCs is small enough to have minimal scattering thus reducing the chances of far-field enhancement. At high NC concentration of 6.7 ppm and 14 ppm, the quenching dominated the enhancement of edge emission. Edge emission results were corroborated by the electrical characterization of PLSC devices. An increase in the current was observed for the optimized PLSC sample with respect to the sample with no NCs. Power conversion efficiency was calculated to increase by 1.2 times for the optimized PLSC sample when compared to LSC with no MNP.

The optimized PLSC device was studied in outdoor conditions simultaneously with an LSC device (70 ppm), blank reference and a bare PV cell placed horizontally. The data from both sunny and cloudy days were analyzed. The key observation was that PLSC performed better than the PV cell in cloudy and diffuse light conditions. The power conversion efficiency of the PLSC device almost doubled under such conditions. The possible reason for this could be the change in the spectral ratio and higher scattering of light in cloudy conditions. The performance of the PLSC with variation in solar disc position throughout the day was investigated. It was observed that the ratio of power conversion efficiency of PLSC device to PV cell was higher in morning and evening as compared to the afternoon for both clear and diffuse conditions. The average PCE of PLSC device is 1.4 times the PCE of bare PV cell on the cloudy day. On sunny day during evening time when there were no clouds the PLSC device average PCE is 2.7 times the average PCE of the PV cell. Thus the PLSC device can be feasible in higher latitude countries where the sun is closer to the horizon for a longer duration.

Performance of the PLSC device with variation in radiation intensity was studied and it was observed that the PLSC was less adversely affected in low light as compared to PLSC. It is possible that PLSC can be used due to the less tendency to spike due to the change in lighting conditions. A diffuse reflector used as rear reflector resulted in a 5% further increase in the average power output as compared to an LSC device.

The PLSC device performed 45% than a PV cell in winter month as compared to a summer month. However, the monthly energy yield of the PLSc device is 2.2 times lower than that of a state of the art c-Si PV cell.

Chapter 7

Conclusions and Future work

Gold nanorods and gold core silver shell nanocuboids were fabricated to utilize the plasmonic properties of both gold and silver. A unified methodology was developed from the synthesis to the phase transfer and quantitation of the Au NRs and Au@Ag NCs in the host matrix (Silicone polymer). To ensure high shape and size yield of the MNPs, the as-synthesized MNPs were purified via multiple rounds of centrifugation. The extinction spectra of the MNPs before and after centrifugation showed a shift in the SPR peaks. For Au NRs, a red-shift in the longitudinal SPR peak meant higher aspect ratio NRs in the supernatant solution. As for Au@AgNCs presence of SPR peak at 365 nm (due to Ag shell) and blue shift in the longitudinal peak meant lower aspect ratio NCs were present in the pellet solution. The surface of the Au NRs and Au@Ag NCs was modified with PEG-SH to enable the phase transfer of the MNPs from aqueous to organic solvent that will be compatible with Silicone. A successful PEGylation was achieved for both Au NRs and Au@Ag NCs and a blue shift in the longitudinal SPR peak denoted the change in the surface of the MNPs. PEGylation simplified the phase transfer of the MNPs into an organic solvent with the help of a common solvent. A red-shift in the longitudinal SPR peak is observed for both the MNPs due to a change in the refractive index of the medium. Phase transfer into dichloromethane was achieved for Au NRs and Au@Ag NCs with a

phase transfer efficiency of 84% and 75% respectively. The concentration of the MNPs was estimated by ICP-MS technique and electron microscopy images. This helped in estimating the concentration of the MNPs in the PLSC device. The Au NRs and Au@Ag NCs were stable in the host matrix for one year and six months respectively. The established methodology was reproducible and gave a good control over the inclusion of MNPs in the host matrix.

Lumogen Red305 dye and ZnCuInS-ZnS QDs compatibility in Silicone polymer was studied. The PLQY of the red305 dye and QDs was found to be $97\pm 2\%$ and $20\pm 0.5\%$ respectively. Waveguides of size $4.5\times 4.5\times 0.3\text{ cm}^3$ with varying doping concentration (10 ppm to 160 ppm) of Red305 dye were fabricated. The total and edge emission from the waveguides was measured using an integrating sphere. Increasing the dye doping concentration increased the edge emission almost linearly for low doping concentration waveguides (till 50 ppm). High doping concentration (above 130 ppm) of the dye resulted in a deviation from the linear trend and a decrease in the integrated emission is observed. A change in the emission profile along with a red-shift in the emission peak is also observed for high doping concentration waveguides. These results show the re-absorption losses overtaking the increase in the emission intensity, mainly due to the increase in the dye doping concentration in the waveguides. Hence, 70 ppm Red305 dye doping concentration is chosen as the optimum concentration for $4.5\times 4.5\times 0.3\text{ cm}^3$ size devices. Outdoor characterization of the LSC devices, blank reference and a vertically placed bare PV cell is carried out in cloudy conditions. The 70 ppm LSC average PCE is 2.7 times the PCE of bare PV cell. Titanium dioxide nanoparticles were used to fabricate diffuse reflectors with varying concentration of the TiO_2 concentration. A 1.7 times increase was observed in the edge emission of LSC waveguide with a rear diffuse reflector than without any back reflector. These results mainly were a stepping stone in the development of the PLSC device.

Various concentration of Au@Ag NCs (0.6 ppm to 14 ppm) along with Red305 dye (70 ppm) was used to fabricate PLSC devices of size $4.5\times 4.5\times 0.3\text{ cm}^3$. Au@Ag

NCs had a maximum overlap with the absorption spectra of Red305 dye, minimal overlap with the emission spectra. The edge emission from the PLSC waveguides showed an increase in the emission intensity on increasing the Au@Ag NCs doping concentration till 1.1 ppm. However, a further increase in the Au@Ag NCs doping concentration resulted in a decrease in the emission intensity, with 14 ppm doping concentration having emission intensity lower than the LSC waveguide without any MNPs. This continuous change in the emission intensity with increasing Au@Ag NCs doping concentration in the waveguides can be explained by the decrease in the distance between the MNP and the Red305 dye molecule. A 30% enhancement in the emission intensity is obtained for 1.1 ppm Au@Ag NCs doping concentration, this enhancement in the edge emission is mainly due to the increase in the excitation rate of the Red305 dye molecule. The feasibility of the PLSC device in European weather was tested in the outdoor setup. The PLSC device was tested along with an LSC device (70 ppm), a blank reference, a bare PV cell placed horizontally. In direct light conditions the bare PV cell performance overtakes the PLSC device across midday, however, during morning and evening when the sun's position is closer to the horizon the PLSC and LSC devices perform better than the bare PV cell. In the evening time on a sunny day the PLSC device has 2.7 times the PCE of bare PV cell. The PLSC has a higher efficiency in the morning and evening and is not strongly effected by the increase in radiation intensity. This means it might not be susceptible to sudden spikes due to change in lighting conditions. A diffuse reflector was used as a rear reflector with the PLSC device and a 5% increase is observed in the power output on a cloudy day.

7.1 Contribution to knowledge

This PhD work has made the following contributions to knowledge:

- A protocol is established for incorporating uniform sized Au NRs and Au@Ag NCs in a polymer. Purification of as-synthesized anisotropic MNPs, surface functionalization and phase transfer of the MNPs into organic phase is achieved

with high efficiency. The methodology is reproducible and can help in various applications (biomedicine, sensors) that exploit the plasmonic properties of MNPs.

- The plasmonic properties of MNPs is exploited to enhance the efficiency of LSC. 30% enhancement in the edge emission, for optimum Au@Ag NCs doping concentration is achieved. The role of MNP concentration plays an important role in the enhancement or quenching of the edge emission from a PLSC device. This study shows that re-absorption losses due to high concentration of fluorophores can be reduced by using MNPs in the device.
- Outdoor test is conducted for the PLSC device and it is observed that the device performs better than bare PV cell in diffuse light. The outdoor results show the feasibility of the PLSC device in diffuse and direct light conditions in comparison to a bare PV cell. Even though the absolute efficiency of a bare PV cell is higher than PLSC but the latter shows promise for integration in facade as its efficiency is not highly dependent on angle of illumination. Seasonal performance of PLSC device in comparison to a bare PV cell is illustrated. PLSC device gives a higher average power output than the PV cell in December, this is mainly due to the higher amount of diffuse radiation during winter months in Ireland. In absolute energy yield terms a state of the art c-Si solar cell will outperform a PLSC device placed in a horizontal position. However, PLSC device holds promise in BIPV setting especially for a country like Ireland that has a high ratio of diffuse radiation throughout the year.

7.2 Recommendations for future work

- Au@Ag NCs are stable in Silicone for six months after which they aggregate in the polymer. Further research should be conducted to increase the stability of Au@Ag NCs in the host matrix. Extensive research is lacking about the functionalization of core shell NCs owing to their unique shape. One way

to increase the stability is by optimizing the PEG-SH areal density on the NCs. The areal density of PEG-SH on the NCs can be found with the help of thermal gravimetric analysis, it can give an idea about the number of PEG-SH molecules covering 1 nm^2 of the NC. Furthermore, different length of the alkyl chain of PEG-SH molecules will provide different amount of stability to the NCs.

- In this work Red305 dye has been used for PLSC. Other type of fluorophores such as rare earth complexes and QDs can be used with Au NRs and Au@Ag NCs for fabricating PLSC devices. One possibility is to match the emission spectra of the fluorophore that has a non-unity PLQY with the SPR band of MNP. Matching those two spectra can lead to enhancement of edge emission in PLSC device due to increase in the radiative decay rate of the fluorophore. The maximum fluorescence enhancement can take place when both the absorption and emission spectra of the fluorophore are matched by the SPR band of an MNP.
- The NRs and NCs can be aligned in the host matrix to enable directional emission of the fluorescence. There are many techniques to align the NRs one of them is by the application of an external electric field. The main challenge would be to achieve full alignment of the MNPs with the help of the electric field. Aligning the MNPs in host matrix would also give insight about the interaction of fluorophore with aligned MNP. TEM or Atomic force microscopy is used to study the assembly of the MNPs in polymer, but, usually the samples studied have low (microns) thickness. It will be important to find a way to study the assembly of the MNPs before and after the alignment.
- Large scale PLSC devices should be fabricated and tested along with PV module. This will help in the estimation of the cost analysis and feasibility of the PLSC device. A correct optical coupling between the PV cell and the waveguide should be done so as to ensure no air gaps that can lead to

loss of solar radiation before reaching the cell. Figure 7.1 shows the possible future application of large scale PLSC devices in BIPV, by forming a BIPV component comprising of a periodic structure of smaller Stem components.

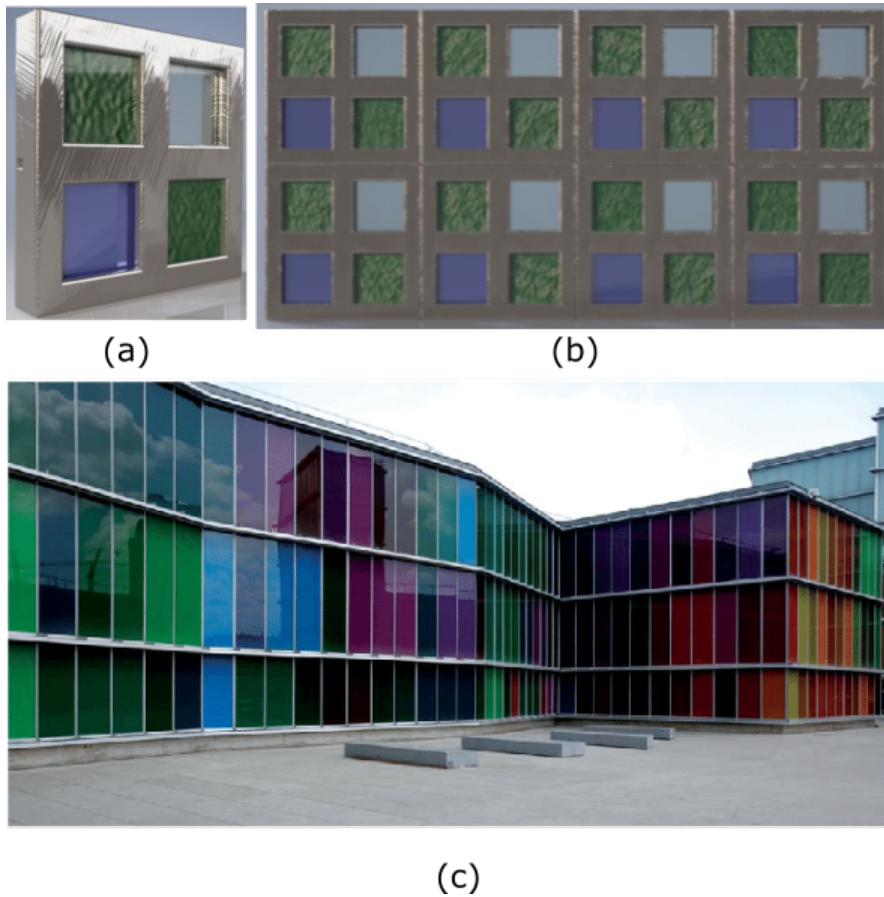


Figure 7.1: a) Stem component with different coloured PLSC devices. b) Periodic structure containing the Stem components, thus, forming a BIPV component. c) Future application of PLSC devices in the facade of the building.

(Rafiee, 2019)

Appendices

Appendix A

Silver Nanowires

In this appendix the challenges faced in the synthesis and purification of Ag NRs is discussed. Due to the difficulties in achieving a high shape yield of Ag NRs the focus was shifted to synthesize Au NRs; after which these Au NRs were further used as seeds to make Au@Ag NCs.

A.1 Detailed synthesis process of Ag NRs

Ag NRs were synthesized by the seed mediated approach, with CTAB as the capping agent (Hormozi-Nezhad et al., 2012). Silver seeds were synthesized by chemical reduction of the precursor (Jana, Gearheart, and Murphy, 2001e). A 20 ml solution was made containing 0.25 mM AgNO₃ and 0.25 mM trisodium citrate that acted as a capping agent (Henglein and Giersig, 1999). 0.6 ml of ice-cold 0.01 M NaBH₄ was added to the solution while stirring the solution vigorously for 30 seconds. A light-yellow colour was observed for the seed solution. The reducing agent was added simultaneously into the silver precursor solution to ensure reduction of all the silver ions to seeds. The seed solution should be at least 2 hours old before it is used for further processes (Ledwith, Whelan, and Kelly, 2007). It could not be used after 24 hours as a film is formed on the surface of seeds solution indicating aggregation of the seeds. The seed solution synthesis was not reproducible, therefore, it was decided to further investigate the factors that might influence the seed

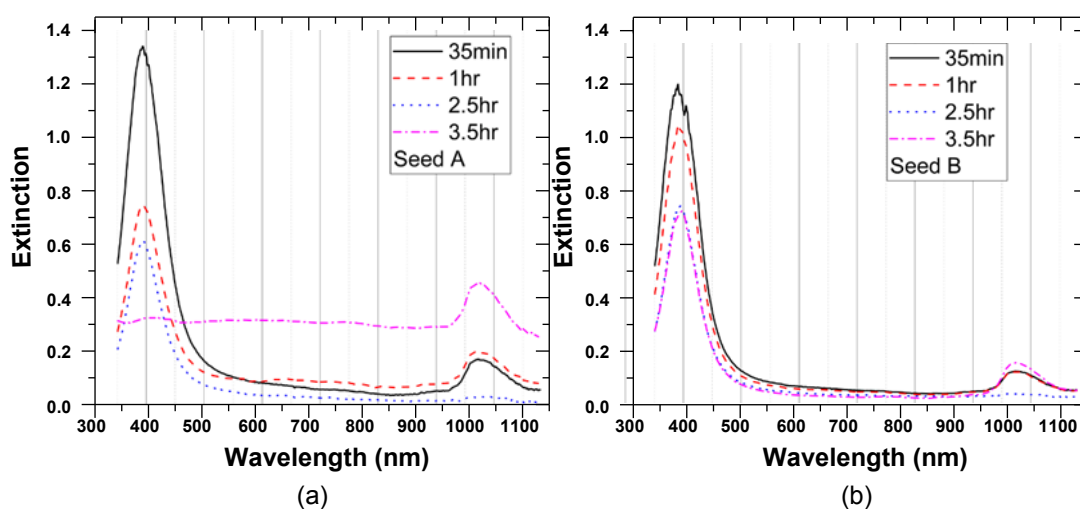


Figure A.1: UV-VIS spectra of a) Seed A and b) Seed B taken after every half an hour.

solution synthesis.

Light: Silver salt is sensitive to light, therefore, silver seeds were found to be unstable in the presence of light. It was observed that preparing the seed solution in a dark room had a significant difference to the seed solution prepared in light. Seed A that was light yellow in color was prepared with light in the room and seed B a dark yellow colored solution was prepared in a dark room, with all the other factors being constant. As can be observed for seed A in Figure A.1 the extinction intensity decreases after every half an hour, no prominent peak observed after 3.5 hours. For seed B, UV-VIS spectrum in Figure A.1 after 2.5 hours matches the spectrum after 3.5 hours thus concluding that the seeds are stable with time.

Addition of NaBH_4 : The addition of the reducing agent should be fast and simultaneous (Jana, Gearheart, and Murphy, 2001e). However, on adding ice-cold 0.6 ml of NaBH_4 solution to the seed solution, the solution turned completely black instantaneously and formed a film on the walls of the bottle. This showed that the particles had agglomerated, making the seed solution incapable of further use. It was observed that simultaneous addition of more than 0.4 ml of the reducing agent

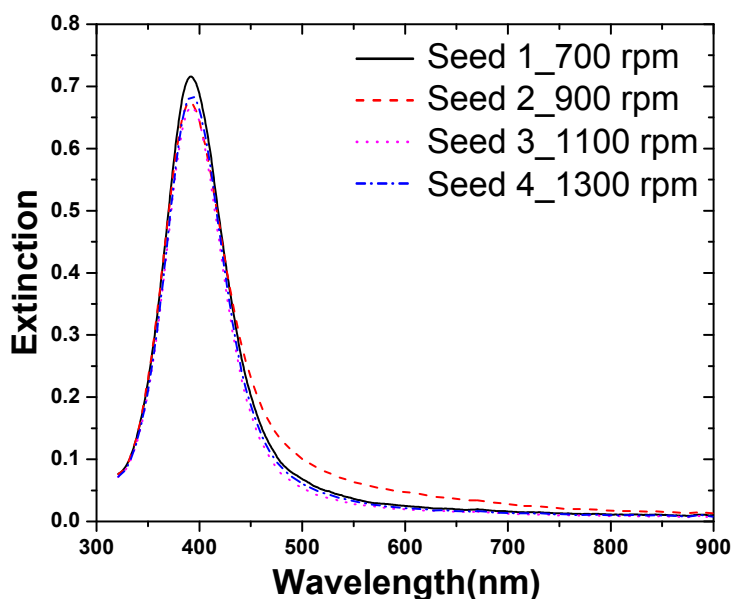


Figure A.2: UV-VIS spectra of the seed solutions with 700, 900, 1100, 1300 rpm for seeds 1-4 respectively.

resulted in particle agglomeration. To overcome this issue, the reducing agent solution was added drop-wise, this helped in obtaining yellow color of the seed solution which is characteristic of Ag seed solution.

Stirring speed: It is required to vigorously stir the seed solution while adding NaBH_4 to the solution. Different stirring speeds from 700 rpm 1300 rpm were tried FigureA.2 and not a significant difference was observed between the seed solutions.

In the growth solution; varied amount of seed solution (0.06 ml, 0.1 ml, 0.15 ml, 0.25 ml) was added to solutions containing 0.25 ml of 10 mM AgNO_3 , 0.50 ml of 0.1 M AA, and 10 ml of 0.05 M CTAB. Finally, 0.10 ml of 1 M NaOH was added to each solution. NaOH was added to increase the pH level to allow the AA to reduce the silver salt into nanorods (Lee et al., 2004). After addition of NaOH, the solution was gently shaken and within a few minutes a colour change (red, to brown, to green) occurred depending on seed concentration. The transverse plasmon band of the synthesized Ag NRs was very high in intensity as compared to the longitudinal plasmon band as can be seen in Figure A.3 the wavelength of the transverse peak is similar to where the spherical Ag NPs have a plasmon resonance thus indicating

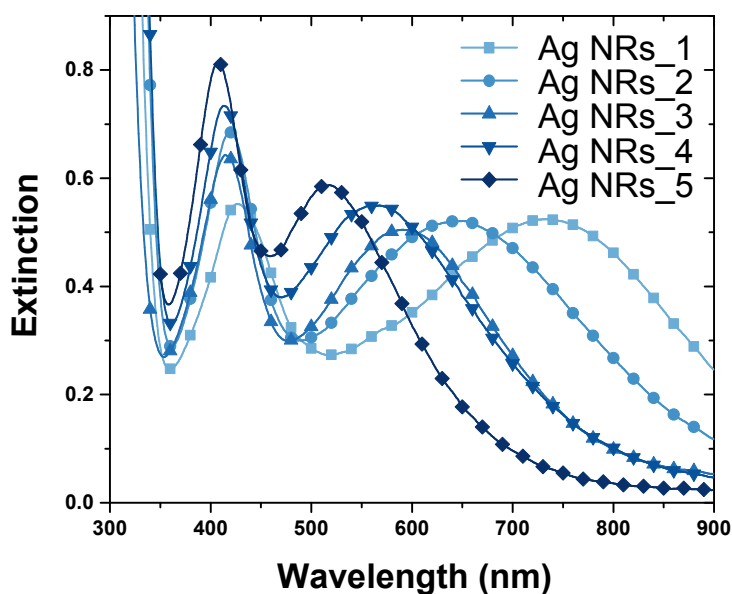


Figure A.3: UV-VIS spectra of Ag NRs samples 1-5 in DI water containing 0.05 ml, 0.1 ml, 0.15 ml, 0.35 ml and 0.4 ml seed solution in the growth solution respectively.

that there is a loweryield of NRs.

A.2 Optical properties of silver nanorods

Optical extinction spectra of the as-prepared Ag NRs solution obtained by UV-VIS spectrophotometer in Figure A.3. The UV-VIS spectra shows two prominent peaks, the transverse plasmon band red-shifts from ~ 408 nm to ~ 427 nm the longitudinal peaks vary from ~ 517 nm to ~ 733 nm for Ag NR samples 1 to 5 respectively. The ratio of the seed concentration and base (NaOH) concentration to the Ag^+ concentration are key to making larger aspecta ratio nanorods. The significant red shift in the longitudinal peak is due to the increase in the aspect ratio of the Ag NRs by decreasing the amount of seeds in the growth solution.

The transverse plasmon peak is higher in intensity when compared to the longitudinal peak. This shows that Ag spheres in the as-prepared solution are contributing significantly to the absorption spectra. A broad asymmetric FWHM of the spectra indicate poor size dispersion of Ag NRs, which is supported and confirmed

by SEM imaging. The synthesis process is reproducible with 5-10 nm shift in the SPR wavelength position of the longitudinal band. Due to the problems stated above it is imperative to purify as-prepared Ag NRs to remove the by-products and additives (CTAB) to ensure longer stability of the nanorods.

A.3 Purification of the silver nanorods

The low shape yield is evident from the UV-VIS spectra of the as-prepared Ag NRs. The as-prepared solutions of Ag NRs with less than 0.25 ml of seed solution were centrifuged at 600g for 20 minutes and the pellet was re-dispersed in DI water. Ag NRs with seed solution more than 0.25 ml were centrifuged at 4,900g for 30 minutes and the pellet was re-dispersed in DI water, at this high speed there were almost no NPs in the supernatant. The UV-VIS spectra of Ag NRs before and after centrifugation is shown in Figure A.4. Multiple centrifugation steps resulted in agglomeration of the NRs. A peak appears around 345 nm after the centrifugation as can be seen in Figure A.4a, three plasmon bands is an indication of nanotriangles in the solution (Wu, Zhou, and Wei, 2015). This peak is evident in both pellet and the supernatant solution, hence the shape separation is not complete via centrifugation. There was also an overall decrease in the intensity for all the Ag NR samples and a strong blue shift of longitudinal plasmon bands for Ag NR sample 4 particularly as can be seen in Figure A.4b. The blue shift shows that there are more by-products; spheres and shorter rods in the pellet. Different centrifugation speeds were used to separate the triangles from the nanorods but it was observed that the peak at 345 nm was always present. This finding was contrary to the recipe being followed for the synthesis of the Ag NRs. SEM imaging was carried out to further investigate this issue.

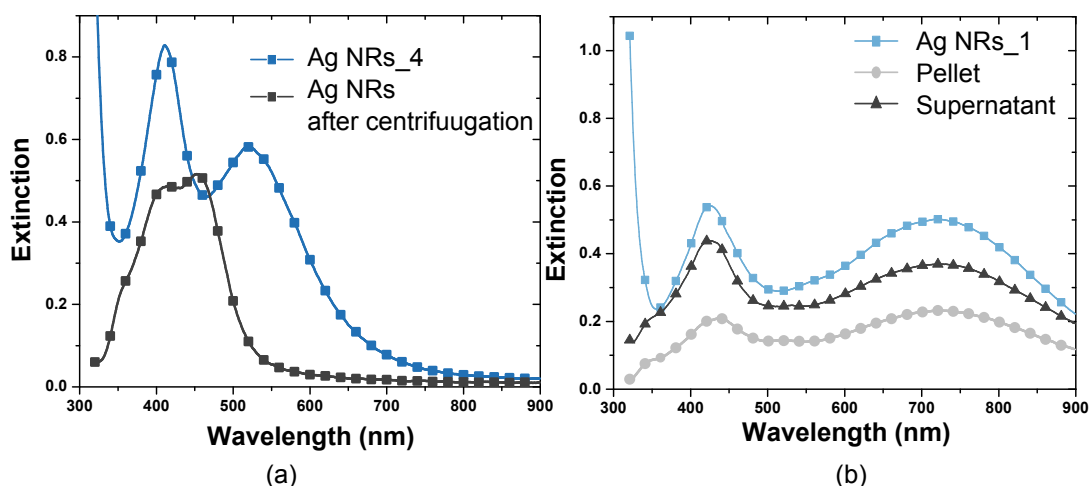


Figure A.4: UV-VIS spectra of a) Ag NRs sample 4 and b) Ag NRs sample 1 taken before and after centrifugation by re-dispersing the pellet in DI water

A.4 Morphology analysis of silver nanorods

SEM images of Ag NRs sample 1 can be seen in Figure A.5. It is observed that the yield of nanotriangles is higher than NRs, triangles are usually the by-product of the synthesis procedure. The NRs have an average length of ~ 300 nm. The average length of edge of the triangles is ~ 40 nm. The shape yield of the synthesis process is very low therefore the centrifugation process is not an effective method to separate the rods from nanorods. The aspect ratio of the rods is 8 ± 0.5 which is relatively larger than reported in the literature for Ag NRs (Jana, Gearheart, and Murphy, 2001e), having a longitudinal peak around 700 nm.

A.5 Challenges in Ag NR synthesis

- **Reproducibility:** Factors such as temperature and pH have a strong effect on the aspect ratio and yield of the Ag NRs. It was observed that a slight change in temperature, using a seed solution that was at a lower temperature than the water bath had an effect on the wavelength position of the longitudinal peak.
- **Low shape yield:** Despite optimizing the seed solution and increasing the

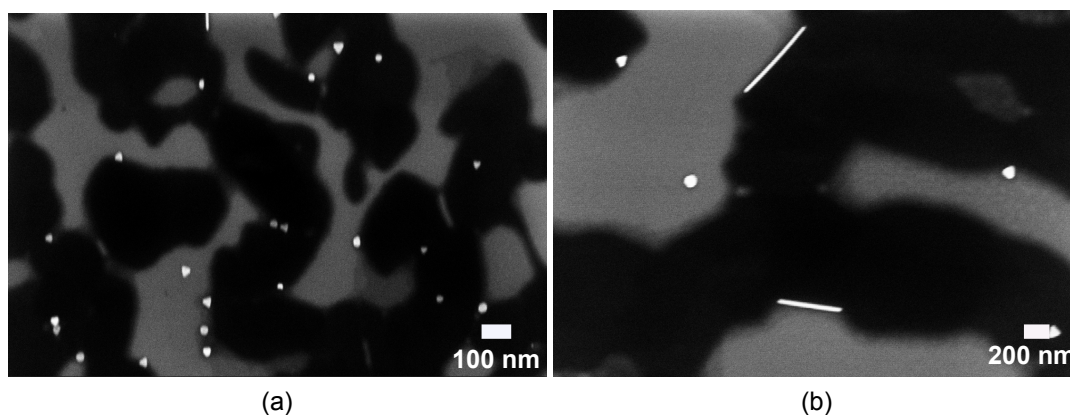


Figure A.5: SEM image of Ag NRs sample 1 after purification, the presence of nanotriangles in the solution is evident and they have approximately the same size as the spheres.

yield of the seeds, the yield of the NRs was low in the as-prepared Ag NR solution. This was evident by the UV-VIS spectra where the ratio of the longitudinal peak to the transverse peak was small. The transverse peak had the same or higher peak intensity than the longitudinal peak, this was due to the presence of a high number of by-products in the solution. The maximum reported yield for Ag NRs is 30% (Silver et al., 2009).

- By-products: The appearance of a peak at ~ 345 nm after centrifugation hinted that there were nanotriangles present in the solution.
- Purification: Even with the presence of by-products and low yield of NRs in the asprepared solution, it was found that it was difficult to separate the NRs by centrifugation. Different centrifugation speeds (600, 4900 and 8,000g) were used for varying time (15-30) minutes and data of pellet and supernatant was studied. It was found that the peak at ~ 345 nm was present for all the solutions thus indicating the presence of nanotriangles.

Appendix B

Gold nanospheres Quantitation

Two different sizes of gold nanospheres (Au NSs) were synthesized and quantified using ICP-MS. This exercise was mainly carried out to validate the quantitation methodology for different shapes of MNPs.

The seed-mediated synthesis process was used to synthesize Au nanospheres (Jana, Gearheart, and Murphy, 2001c). A seed solution was prepared by adding ice-cold NaBH_4 in a conical flask containing TSC and HAuCl_4 solution stirring at 900 rpm. The solution turned pink and was used two hours after preparation. The growth solution consisted of 0.25mM HAuCl_4 and 0.08M CTAB solution. For Au NSs sample A, 7.5 ml of growth solution was mixed with 0.1M AA, and 2.5 ml of the seed solution while stirring at 900 rpm, after 20 minutes the solution turned red. For Au NSs sample B, 9 ml of growth solution was mixed with 0.1M AA, and 1 ml of the seed solution while stirring at 900 rpm, after 20 minutes the solution turned red-brown. The as-prepared solutions can be seen in FigureB.1.

Two concentrations of each sample were prepared and the UV/VIS spectra of the samples can be seen in FigureB.1. The plasmon band is at ~ 521 nm and ~ 525 nm for sample A and sample B respectively. The NSs were imaged using SEM as seen in FigureB.2. 100 MNPs were analyzed to get the size dispersion of the MNPs. For sample A, majority of nanospheres had a diameter of ~ 5.5 nm, for sample B the nanospheres have a diameter of ~ 10.5 nm. Similarly to Au NRs and Au@Ag

Appendix B. Gold nanospheres Quantitation

NCs, Au metal content in Au NSs was found using ICP-MS. Volume of the NSs was found with the help of the SEM images. The number of Au NSs were calculated for two different concentrations for each sample. The experimentally obtained results are summarized in TableB.1.

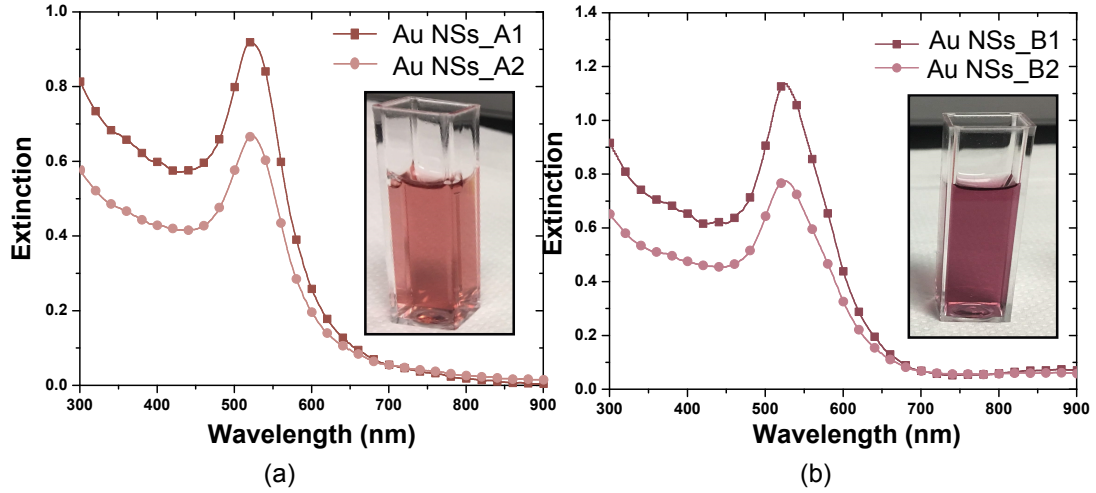


Figure B.1: Photograph and UV/VIS spectra of a) Au NSs sample 2 1 and b) Au NS sample 2.

| MNP | ICP concentration ($\mu\text{g}/\text{l}$) | Volume of Particle (m^3) | Number of metal atoms in one MNP | Number of metal atoms in total volume | Concentration of sample (N/L) |
|----------|--|------------------------------|----------------------------------|---------------------------------------|-------------------------------|
| Au NS A1 | 50 | $8.71137\text{E}-26$ | 5139.454058 | $1.52872\text{E}+16$ | $2.97448\text{E}+16$ |
| Au NS A2 | 33 | $8.71137\text{E}-26$ | 5139.454058 | $1.00896\text{E}+16$ | $1.96316\text{E}+16$ |
| Au NS B1 | 61 | $6.06131\text{E}-25$ | 35759.94293 | $1.86504\text{E}+16$ | $5.21545\text{E}+15$ |
| Au NS B2 | 37 | $6.06131\text{E}-25$ | 35759.94293 | $1.13125\text{E}+16$ | $3.16347\text{E}+15$ |

Table B.1: Number of Au NSs in a given volume.

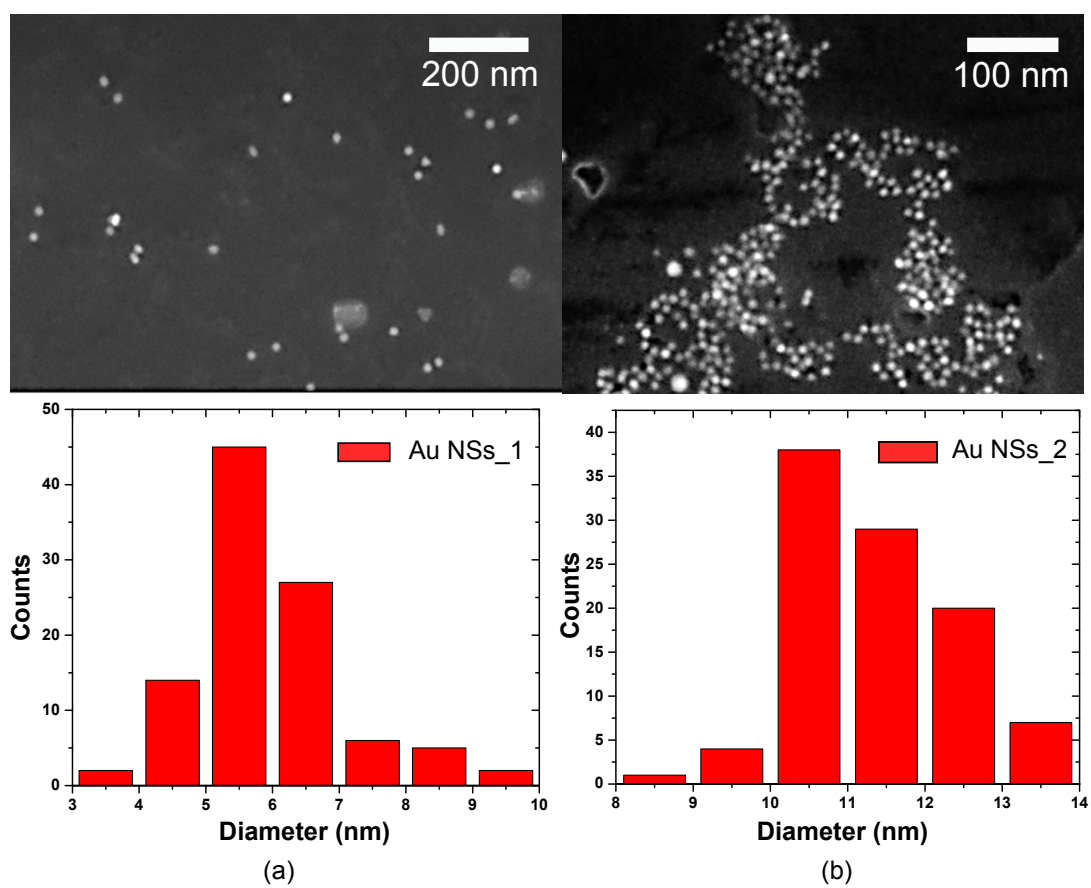


Figure B.2: SEM image and size analysis of a) Au NSs sample A and b) Au NSs sample B.

Appendix C

Lumogen Yellow083 dye in Silicone

Lumogen Yellow083 dye compatibility in the host matrix Silicone was studied. The molecular absorption spectra of Yellow083 is characterized by two distinct peaks at ~470 nm and ~440 nm and the emission peak is at ~480 nm giving a Stokes' shift of around 10 nm. Initially, samples with low concentration (1.1-2.3 ppm) of the dye were fabricated. For the low concentration samples the UV-VIS spectra can be seen in FigureC.1, the absorbance intensity is very low, thus making it difficult to measure their absorbance. Five samples with concentration varying from 10-55 ppm were synthesized in a similar manner. The absorption spectra of the sample can be seen in FigureC.1. It was observed that the absorbance profile had drastically changed on increasing the concentration of the dye in Silicone. There was an appearance of a peak at ~508 nm and the dye had a wide absorption range extending till 550 nm. This might be due to the re-absorption of light by the dye as one of the emission peak for the Yellow083 is at ~520 nm.

The maximum absorbance intensity is 0.3 which is very low considering the concentration of the sample. The concentration of the dye was calculated using the absorbance spectra to determine if the dye was functioning as expected in Silicone. The concentration of Yellow083 dye in Silicone was calculated using the Beer Lam-

Appendix C. Lumogen Yellow083 dye in Silicone

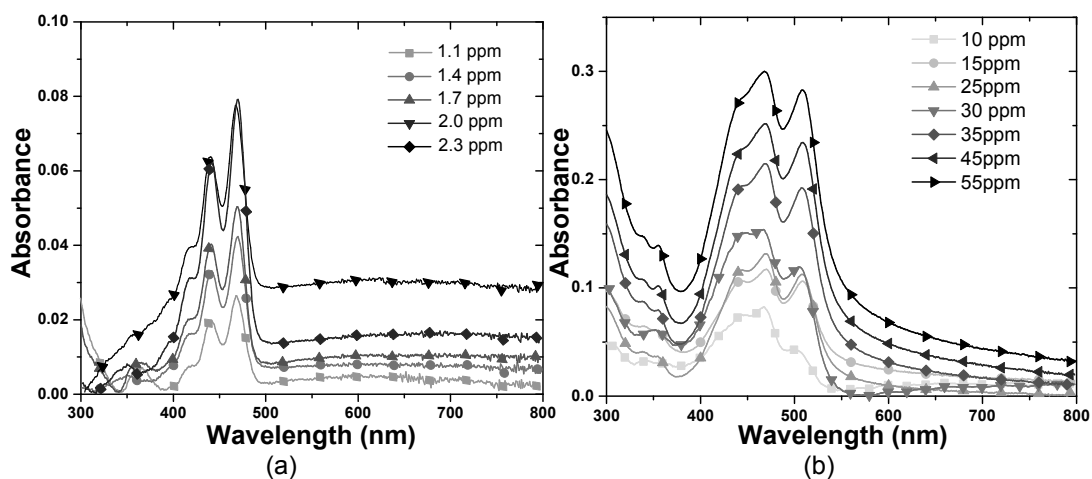


Figure C.1: UV-VIS spectra of Yellow083 dye in Silicone polymer having a) 1.1 ppm-2.3 ppm concentration, b) 10 ppm to 55 ppm concentration.

bert law, the resultant values are given in TableC.1. At low concentration values the dye completely dissolves in the polymer and this is supported by the values for low concentration (1.1-2.3 ppm) samples. However, at high concentration, the dye seems to have poor solubility in Silicone, so that less dye molecules are available to form agglomerates. This is also evident by the low absorbance values from the dye in Silicone.

Appendix C. Lumogen Yellow083 dye in Silicone

| Conc. of dye used to make samples (ppm) | Absorbance peak | Sample thickness (cm) | Conc. calculated using Beer-Lamberts law |
|---|-----------------|-----------------------|--|
| 1.1 | 0.025 | 0.3 | 0.94 |
| 1.3 | 0.04 | 0.3 | 1.50 |
| 1.7 | 0.045 | 0.3 | 1.69 |
| 2.0 | 0.08 | 0.21 | 4.29 |
| 2.3 | 0.078 | 0.3 | 2.93 |
| 10 | 0.083 | 0.3 | 3.12 |
| 15 | 0.118 | 0.25 | 5.32 |
| 25 | 0.132 | 0.23 | 6.46 |
| 30 | 0.154 | 0.3 | 5.78 |
| 35 | 0.216 | 0.28 | 8.69 |
| 45 | 0.253 | 0.27 | 10.55 |
| 55 | 0.30 | 0.27 | 12.51 |

Table C.1: Measured Yellow083 dye concentrations for Silicone samples

The total emission spectra of 10 ppm and 30 ppm sample was taken using the integrating sphere setup discussed in section 3.8.1. The excitation wavelength was set at 405 nm for this measurement. The emission spectra obtained can be seen in FigureC.2. A red-shift in the emission peak is observed on increasing the doping concentration. The emission spectra has a completely different profile as expected from Lumogen Yellow083 dye. Yellow083 dye is not compatible with the Silicone polymer especially when dealing with high concentrations.

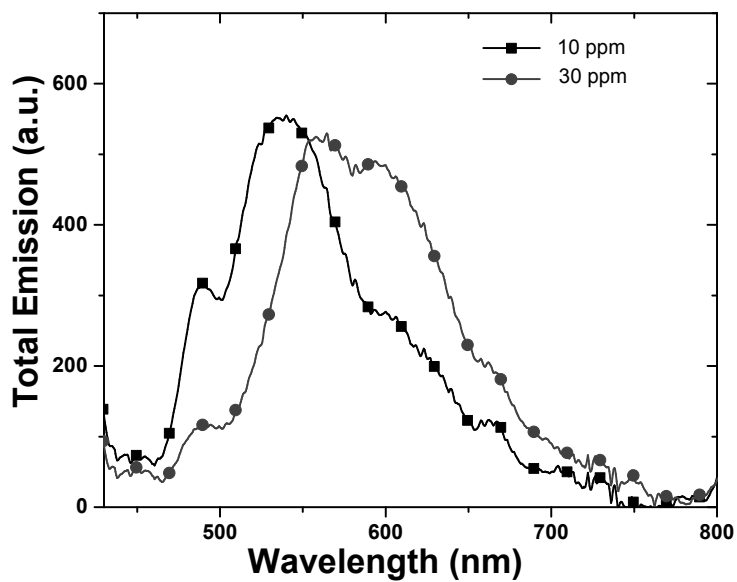


Figure C.2: Total emission spectra of 10 ppm and 30 ppm Yellow083 dye in Silicone polymer.

List of Publications

Journal publications

- Sethi, Arunima, et al. "Broadband Plasmonic Coupling and Enhanced Power Conversion Efficiency in Luminescent Solar Concentrator." *Solar Energy Materials and Solar Cells*, vol. 203, 2019, p. 110150, doi:10.1016/j.solmat.2019.110150.
- Sethi, Arunima, et al. "A Unified Methodology for Fabrication and Quantification of Gold Nanorods, Gold Core Silver Shell Nanocuboids and Their Polymer Nanocomposites." *Langmuir*, 2019, doi:10.1021/acs.langmuir.9b01481.

Book chapter

- H. Ahmed, A. Sethi, J. Doran, and S. J. McCormack, Plasmonic Interaction in Enhanced Luminescent Down-Shifting Layers for Photovoltaic Devices. Book Chapter in the book "Plasmonics: Advances in Research and Applications". ISBN: 978-1-153610-174-4 to be published January 2017 by Nova Science Publishers, Inc. Hauppauge, New York, USA.

Conference proceedings

- Sethi, Arunima, S. Chandra, H. Ahmed and S. J. McCormack, 2017. Gold Nanorods for application in Plasmonic Luminescent Solar Concentrators. *13th Photovoltaic Science, Applications and Technology Conference C99 (PVSAT-13)*, April 5-7, 2017, Bangor, UK.

-
- Sethi, Arunima, S. Chandra , H. Ahmed, Gilligan, S. and S. J. McCormack, 2017. Phase transfer and polymer compatibility of gold and gold core silver shell nanorods for luminescent solar devices. *35 th EU Photovoltaic Solar Energy Conference and Exhibition (PVSEC), September 25-29, 2017, Amsterdam, The Netherlands.*
 - Sethi, Arunima, S. Chandra , H. Ahmed and S. J. McCormack, 2018. Fluorescent organic dyes in a silicone encapsulant composite for Luminescent Solar Concentrators. *World Conference On Photovoltaic Energy Conversion (WCPEC-7) June 10-15, 2018 Waikoloa, Hawaii, U.S.A.*
 - Rafiee, Mehran, S. Chandra , H. Ahmed, **Sethi, Arunima** and S. J. McCormack, 2018 Monte Carlo Ray Tracing Modelling of Multi-Crystalline Silicon Photovoltaic Cell Enhanced by Luminescent Material. *World Conference On Photovoltaic Energy Conversion (WCPEC-7) June 10-15, 2018 Waikoloa, Hawaii, U.S.A.*

'References'

- Ah, Chil Seong, Seung Do Hong, and Du-Jeon Jang (2001). "Preparation of Au-core-Ag-shell nanorods and characterization of their surface plasmon resonances". In: *The Journal of Physical Chemistry B* 105.33, pp. 7871–7873 (cited on page - 41).
- Ahmed, Nabil A, Masafumi Miyatake, and AK Al-Othman (2008). "Power fluctuations suppression of stand-alone hybrid generation combining solar photovoltaic/wind turbine and fuel cell systems". In: *Energy Conversion and Management* 49.10, pp. 2711–2719 (cited on page - 127).
- Ahmed, Waqqar et al. (2009). "Quantitative analysis of gold nanorod alignment after electric field-assisted deposition". In: *Nano letters* 9.11, pp. 3786–3794 (cited on page - 37).
- Ahn, Tai-Sang et al. (2007). "Self-absorption correction for solid-state photoluminescence quantum yields obtained from integrating sphere measurements". In: *Review of Scientific Instruments* 78.8, p. 086105 (cited on pages - 58, 59).
- Akbulut, Ozge et al. (2012). "Separation of nanoparticles in aqueous multiphase systems through centrifugation". In: *Nano letters* 12.8, pp. 4060–4064 (cited on page - 76).
- Alonso-González, P et al. (2012). "Resolving the electromagnetic mechanism of surface-enhanced light scattering at single hot spots". In: *Nature communications* 3, p. 684 (cited on page - 29).
-

-
- Amendola, Vincenzo et al. (2017). "Surface plasmon resonance in gold nanoparticles: a review". In: *Journal of Physics: Condensed Matter* 29.20, p. 203002 (cited on page - 32).
- Aruda, Kenneth O et al. (2013). "Identification of parameters through which surface chemistry determines the lifetimes of hot electrons in small Au nanoparticles". In: *Proceedings of the National Academy of Sciences* 110.11, pp. 4212–4217 (cited on page - 31).
- Attia, Yasser A et al. (2015). "Photostability of gold nanoparticles with different shapes: the role of Ag clusters". In: *Nanoscale* 7.26, pp. 11273–11279 (cited on page - 30).
- Bailey, Sheldon T et al. (2007). "Optimized excitation energy transfer in a three-dye luminescent solar concentrator". In: *Solar Energy Materials and Solar Cells* 91.1, pp. 67–75 (cited on pages - 22, 108).
- BaniáYaseen, AI et al. (2014). "Facile phase transfer of gold nanoparticles from aqueous solution to organic solvents with thiolated poly (ethylene glycol)". In: *RSC Advances* 4.95, pp. 52676–52679 (cited on page - 89).
- Barber, DJ and Ian C Freestone (1990). "An investigation of the origin of the colour of the Lycurgus Cup by analytical transmission electron microscopy". In: *Archaeometry* 32.1, pp. 33–45 (cited on page - 27).
- Barnham, Keith et al. (2000). "Quantum-dot concentrator and thermodynamic model for the global redshift". In: *Applied Physics Letters* 76.9, pp. 1197–1199 (cited on page - 22).
- BASF. *Lumogen F Collector Dyes: Technical Information*. URL: <http://www2.basf.us/additives/pdfs/p3201e.pdf> (cited on page - 97).
- Batchelder, JS, AH Zewail, and T Cole (1981). "Luminescent solar concentrators. 2: Experimental and theoretical analysis of their possible efficiencies". In: *Applied Optics* 20.21, pp. 3733–3754 (cited on page - 15).
-

-
- Baudys, M et al. (2015). "Weathering tests of photocatalytic facade paints containing ZnO and TiO₂". In: *Chemical Engineering Journal* 261, pp. 83–87 (cited on page - 111).
- Bergren, Matthew R et al. (2018). "High-performance CuInS₂ quantum dot laminated glass luminescent solar concentrators for windows". In: *ACS Energy Letters* 3.3, pp. 520–525 (cited on page - 22).
- Bharadwaj, Palash and Lukas Novotny (2007). "Spectral dependence of single molecule fluorescence enhancement". In: *Optics Express* 15.21, pp. 14266–14274 (cited on page - 34).
- Biagioni, Paolo, Jer-Shing Huang, and Bert Hecht (2012). "Nanoantennas for visible and infrared radiation". In: *Reports on Progress in Physics* 75.2, p. 024402 (cited on page - 27).
- Blaber, Martin G, Matthew D Arnold, and Michael J Ford (2010). "A review of the optical properties of alloys and intermetallics for plasmonics". In: *Journal of Physics: Condensed Matter* 22.14, p. 143201 (cited on page - 33).
- Boer, Dick KG de et al. (2011). "Polarization-independent filters for luminescent solar concentrators". In: *Applied Physics Letters* 98.2, p. 021111 (cited on page - 24).
- Bose, Rahul et al. (2007). "Novel configurations of luminescent solar concentrators". In: *Twenty-second EU PVSEC*, pp. 210–214 (cited on page - 25).
- Bronstein, Noah D et al. (2015). "Quantum dot luminescent concentrator cavity exhibiting 30-fold concentration". In: *Acs Photonics* 2.11, pp. 1576–1583 (cited on pages - 22, 24).
- Brust, Mathias et al. (1994). "Synthesis of thiol-derivatised gold nanoparticles in a two-phase liquid–liquid system". In: *Journal of the Chemical Society, Chemical Communications* 7, pp. 801–802 (cited on page - 86).
- Carbó-Argibay, Enrique et al. (2010). "The Crystalline Structure of Gold Nanorods Revisited: Evidence for Higher-Index Lateral Facets". In: *Angewandte Chemie International Edition* 49.49, pp. 9397–9400 (cited on page - 41).
-

-
- Chandra, Subhash et al. (2012). “Enhanced quantum dot emission for luminescent solar concentrators using plasmonic interaction”. In: *Solar Energy Materials and Solar Cells* 98, pp. 385–390 (cited on page - 25).
- Chang, Ser-Sing et al. (1999). “The shape transition of gold nanorods”. In: *Langmuir* 15.3, pp. 701–709 (cited on page - 39).
- Chen, Ou et al. (2013). “Compact high-quality CdSe–CdS core–shell nanocrystals with narrow emission linewidths and suppressed blinking”. In: *Nature materials* 12.5, p. 445 (cited on page - 23).
- Chen, Yeechi, Keiko Munechika, and David S Ginger (2007). “Dependence of fluorescence intensity on the spectral overlap between fluorophores and plasmon resonant single silver nanoparticles”. In: *Nano letters* 7.3, pp. 690–696 (cited on pages - 33, 34).
- Cheng, Mu-Tian, Shao-Ding Liu, and Qu-Quan Wang (2008). “Modulating emission polarization of semiconductor quantum dots through surface plasmon of metal nanorod”. In: *Applied Physics Letters* 92.16, p. 162107 (cited on page - 37).
- Conibeer, Gavin (2007). “Third-generation photovoltaics”. In: *Materials today* 10.11, pp. 42–50 (cited on page - 3).
- Coropceanu, Igor and Mounji G Bawendi (2014). “Core/shell quantum dot based luminescent solar concentrators with reduced reabsorption and enhanced efficiency”. In: *Nano letters* 14.7, pp. 4097–4101 (cited on pages - 16, 23).
- Corrado, Carley et al. (2016). “Power generation study of luminescent solar concentrator greenhouse”. In: *Journal of Renewable and Sustainable Energy* 8.4, p. 043502 (cited on page - 15).
- Currie, Michael J et al. (2008). “High-efficiency organic solar concentrators for photovoltaics”. In: *Science* 321.5886, pp. 226–228 (cited on page - 22).
- Daud, Muhamad Zalani, Azah Mohamed, and MA Hannan (2014). “An optimal control strategy for DC bus voltage regulation in photovoltaic system with battery energy storage”. In: *The Scientific World Journal* 2014 (cited on page - 127).
-

-
- Davis, Mark W, A Hunter Fanne, and Brian P Dougherty (2001). "Prediction of building integrated photovoltaic cell temperatures". In: *Journal of Solar Energy Engineering* 123.3, pp. 200–210 (cited on page - 126).
- De La Perrelle, ET, TS Moss, and H Herbert (1963). "The measurements of absorptivity and reflectivity". In: *Infrared Physics* 3.1, pp. 35–43 (cited on page - 107).
- Debije, MG, DJ Broer, and CWM Bastiaansen (2007). "Effect of dye alignment on the output of a luminescent solar concentrator". In: *Proceedings of the 22nd European photovoltaic solar energy conference*, pp. 87–89 (cited on page - 24).
- Debije, MG et al. (2009). "The effect of an organic selectively-reflecting mirror on the performance of a luminescent solar concentrator". In: *24th European Photovoltaic Solar Energy Conference (EU PVSEC 2004)*. WIP, pp. 373–376 (cited on pages - 24, 108, 111).
- Debije, Michael G et al. (2011). "Promising fluorescent dye for solar energy conversion based on a perylene perinone". In: *Applied Optics* 50.2, pp. 163–169 (cited on page - 22).
- Dresselhaus, MS and G Dresselhaus (1962). "Interband transitions for metals in a magnetic field". In: *Physical Review* 125.2, p. 499 (cited on page - 29).
- Edelenbosch, Oreane Y et al. (2013). "Luminescent solar concentrators with fiber geometry". In: *Optics express* 21.103, A503–A514 (cited on page - 97).
- Edgar, Jonathan A, Andrew M McDonagh, and Michael B Cortie (2012). "Formation of gold nanorods by a stochastic "popcorn" mechanism". In: *ACS nano* 6.2, pp. 1116–1125 (cited on page - 40).
- El-Bashir, SM, FM Barakat, and MS AlSalhi (2013). "Metal-enhanced fluorescence of mixed coumarin dyes by silver and gold nanoparticles: Towards plasmonic thin-film luminescent solar concentrator". In: *Journal of Luminescence* 143, pp. 43–49 (cited on page - 25).
- El-Bashir, SM, FM Barakat, and MS AlSalhi (2014). "Double layered plasmonic thin-film luminescent solar concentrators based on polycarbonate supports". In: *Renewable energy* 63, pp. 642–649 (cited on pages - 25, 26).
-

-
- Europe, Solar Power. *BUILDING-INTEGRATED SOLAR*. Accessed: 2020-01-30. URL: <https://www.solarpowereurope.org/priorities/solar-buildings/> (cited on page - 25).
- Friedman, Peter S (1981). "Luminescent solar concentrators". In: *Optical Engineering* 20.6, p. 206887 (cited on page - 16).
- Fthenakis, Vasilis and Ken Zweibel (2003). *CdTe PV: Real and perceived EHS risks*. Tech. rep. National Renewable Energy Lab.(NREL), Golden, CO (United States) (cited on page - 4).
- Gans, R v (1915). "Form of ultramicroscopic particles of silver". In: *Ann. Phys* 47.10, pp. 270–284 (cited on page - 30).
- Gao, Jinxin, Christopher M Bender, and Catherine J Murphy (2003). "Dependence of the gold nanorod aspect ratio on the nature of the directing surfactant in aqueous solution". In: *Langmuir* 19.21, pp. 9065–9070 (cited on page - 40).
- Garcia, Miguel A (2011). "Surface plasmons in metallic nanoparticles: fundamentals and applications". In: *Journal of Physics D: Applied Physics* 44.28, p. 283001 (cited on pages - 27, 28).
- Gierhart, Brian C et al. (2007). "Frequency dependence of gold nanoparticle superassembly by dielectrophoresis". In: *Langmuir* 23.24, pp. 12450–12456 (cited on page - 37).
- GlobalMarketOutlook (2018). URL: <http://www.solarpowereurope.org/wp-content/uploads/2018/09/Global-Market-Outlook-2018-2022.pdf> (cited on page - 3).
- Goetzberger, A and W Greube (1977). "Solar energy conversion with fluorescent collectors". In: *Applied physics* 14.2, pp. 123–139 (cited on pages - 13, 18, 20, 107).
- Goetzberger, Adolf and Volker Wittwer (1981). "Fluorescent planar collector-concentrators: a review". In: *Solar Cells* 4.1, pp. 3–23 (cited on page - 21).
-

-
- Goldschmidt, Jan Christoph et al. (2009). "Increasing the efficiency of fluorescent concentrator systems". In: *Solar Energy Materials and Solar Cells* 93.2, pp. 176–182 (cited on pages - 22, 24, 108).
- Gomez-Grana, Sergio et al. (2013). "Au@ Ag nanoparticles: Halides stabilize {100} facets". In: *The journal of physical chemistry letters* 4.13, pp. 2209–2216 (cited on pages - 41, 42).
- Gou, Linfeng and Catherine J Murphy (2005). "Fine-tuning the shape of gold nanorods". In: *Chemistry of materials* 17.14, pp. 3668–3672 (cited on page - 83).
- Gramlich, Gabriela, Jiayun Zhang, and Werner M Nau (2002). "Increased antioxidant reactivity of vitamin C at low pH in model membranes". In: *Journal of the American Chemical Society* 124.38, pp. 11252–11253 (cited on page - 40).
- Green, Martin A (2001). "Third generation photovoltaics: Ultra-high conversion efficiency at low cost". In: *Progress in Photovoltaics: Research and Applications* 9.2, pp. 123–135 (cited on page - 10).
- Group, ITRPV Working et al. (2014). *International Technology Roadmap for Photovoltaic (ITRPV) 2013 Results* (cited on page - 3).
- Gãşmez-Graãsa, Sergio et al. (2012). "Surfactant (Bi)Layers on Gold Nanorods". In: *Langmuir* 28.2. PMID: 22165910, pp. 1453–1459. DOI: [10.1021/la203451p](https://doi.org/10.1021/la203451p). eprint: <https://doi.org/10.1021/la203451p>. URL: <https://doi.org/10.1021/la203451p> (cited on page - 85).
- H. Sargent, E (2005). "Infrared quantum dots". In: *Advanced Materials* 17.5, pp. 515–522 (cited on page - 16).
- Haiss, Wolfgang et al. (2007). "Determination of size and concentration of gold nanoparticles from UV- Vis spectra". In: *Analytical chemistry* 79.11, pp. 4215–4221 (cited on pages - 50, 83).
- Hammond, Geoff et al. (2008). *Inventory of carbon & energy: ICE*. Vol. 5. Sustainable Energy Research Team, Department of Mechanical Engineering (cited on page - 25).
-

-
- Henglein, Arnim and Michael Giersig (1994). "Radiolytic formation of colloidal tin and tin-gold particles in aqueous solution". In: *The Journal of Physical Chemistry* 98.28, pp. 6931–6935 (cited on page - 39).
- Henglein, Arnim and Michael Giersig (1999). "Formation of colloidal silver nanoparticles: capping action of citrate". In: *The Journal of Physical Chemistry B* 103.44, pp. 9533–9539 (cited on page - 141).
- Herteleer, Bert, Jan Cappelle, and Johan Driesen (2012). "Quantifying low-light behaviour of photovoltaic modules by identifying their irradiance-dependent efficiency from data sheets". In: *European Photovoltaic Solar Energy Conference, Date: 2012/09/23-2012/09/28, Location: Frankfurt*. WIP Wirtschaft und Infrastruktur GmbH & Co Planungs KG; Sylvensteinstr. 2 (cited on page - 126).
- Hisdal, Vidar (1987). "Spectral distribution of global and diffuse solar radiation in Ny-Ålesund, Spitsbergen". In: *Polar Research* 5.1, pp. 1–27 (cited on page - 124).
- Hormozi-Nezhad, M Reza et al. (2012). "Controlling aspect ratio of colloidal silver nanorods using response surface methodology". In: *Colloids and Surfaces A: Physicochemical and Engineering Aspects* 393, pp. 46–52 (cited on page - 141).
- Huang, Chih-Ching, Zusing Yang, and Huan-Tsung Chang (2004). "Synthesis of dumbbell-shaped Au- Ag core- shell nanorods by seed-mediated growth under alkaline conditions". In: *Langmuir* 20.15, pp. 6089–6092 (cited on page - 41).
- Huang, Huang-Chiao et al. (2009). "Simultaneous enhancement of photothermal stability and gene delivery efficacy of gold nanorods using polyelectrolytes". In: *Acs Nano* 3.10, pp. 2941–2952 (cited on page - 87).
- IEA (2016). *Key World Energy Statistics* (cited on page - 1).
- IEA (2018a). *Global Energy and CO2 Status Report*. URL: <https://webstore.iea.org/global-energy-co2-status-report-2018> (cited on page - 1).
- IEA (2018b). *Renewables Information Overview* (cited on page - 2).
- IEA Atlas of energy (2016). URL: <http://energyatlas.iea.org/#!/tellmap/1118783123/0> (cited on page - 2).
- IPCC (2015) (cited on page - 2).
-

-
- ISE, Fraunhofer (2019). *Photovoltaics Report* (cited on page - 3).
- Jahn, Martin et al. (2016). "Plasmonic nanostructures for surface enhanced spectroscopic methods". In: *Analyst* 141.3, pp. 756–793 (cited on page - 36).
- Jana, Nikhil R, Latha Gearheart, and Catherine J Murphy (2001a). "Evidence for seed-mediated nucleation in the chemical reduction of gold salts to gold nanoparticles". In: *Chemistry of materials* 13.7, pp. 2313–2322 (cited on page - 39).
- Jana, Nikhil R, Latha Gearheart, and Catherine J Murphy (2001b). "Seed-mediated growth approach for shape-controlled synthesis of spheroidal and rod-like gold nanoparticles using a surfactant template". In: *Advanced Materials* 13.18, pp. 1389–1393 (cited on page - 40).
- Jana, Nikhil R, Latha Gearheart, and Catherine J Murphy (2001c). "Seeding growth for size control of 5- 40 nm diameter gold nanoparticles". In: *Langmuir* 17.22, pp. 6782–6786 (cited on pages - 39, 149).
- Jana, Nikhil R, Latha Gearheart, and Catherine J Murphy (2001d). "Wet chemical synthesis of high aspect ratio cylindrical gold nanorods". In: *The Journal of Physical Chemistry B* 105.19, pp. 4065–4067 (cited on page - 39).
- Jana, Nikhil R, Latha Gearheart, and Catherine J Murphy (2001e). "Wet chemical synthesis of silver nanorods and nanowires of controllable aspect ratio—Electronic supplementary information (ESI) available: UV–VIS spectra of silver nanorods. See <http://www.rsc.org/suppdata/cc/b1/b100521i>". In: *Chemical Communications* 7, pp. 617–618 (cited on pages - 41, 141, 142, 146).
- Jiang, Guoqian et al. (2012a). "Gold nanorods dispersed in homopolymer films: optical properties controlled by self-assembly and percolation of nanorods". In: *ACS nano* 6.2, pp. 1578–1588 (cited on page - 92).
- Jiang, Ruibin et al. (2012b). "Unraveling the evolution and nature of the plasmons in (Au core)–(Ag shell) nanorods". In: *Advanced Materials* 24.35, OP200–OP207 (cited on pages - 73, 74, 82).
-

-
- Johnson, Christopher J et al. (2002). "Growth and form of gold nanorods prepared by seed-mediated, surfactant-directed synthesis". In: *Journal of Materials Chemistry* 12.6, pp. 1765–1770 (cited on page - 40).
- Khan, AF et al. (2010). "Eu³⁺ doped silica xerogel luminescent layer having antireflection and spectrum modifying properties suitable for solar cell applications". In: *Materials Research Bulletin* 45.11, pp. 1562–1566 (cited on page - 22).
- Kleinman, Samuel L et al. (2012). "Structure enhancement factor relationships in single gold nanoantennas by surface-enhanced Raman excitation spectroscopy". In: *Journal of the American Chemical Society* 135.1, pp. 301–308 (cited on page - 31).
- Kreibig, Uwe and Michael Vollmer (1995). "Theoretical considerations". In: *Optical Properties of Metal Clusters*. Springer, pp. 13–201 (cited on page - 28).
- Krumer, Zachar et al. (2017). "Compensation of self-absorption losses in luminescent solar concentrators by increasing luminophore concentration". In: *Solar Energy Materials and Solar Cells* 167, pp. 133–139 (cited on page - 24).
- Kulakovich, Olga et al. (2002). "Enhanced luminescence of CdSe quantum dots on gold colloids". In: *Nano Letters* 2.12, pp. 1449–1452 (cited on page - 120).
- Lakowicz, Joseph R (2001). "Radiative decay engineering: biophysical and biomedical applications". In: *Analytical biochemistry* 298.1, pp. 1–24 (cited on pages - 34–36, 119).
- Lakowicz, Joseph R (2004). "Radiative decay engineering 3. Surface plasmon-coupled directional emission". In: *Analytical biochemistry* 324.2, pp. 153–169 (cited on pages - 35, 36).
- Lal, Surbhi, Stephan Link, and Naomi J Halas (2007). "Nano-optics from sensing to waveguiding". In: *Nature photonics* 1.11, p. 641 (cited on page - 36).
- Le Ru, Eric and Pablo Etchegoin (2008). *Principles of Surface-Enhanced Raman Spectroscopy: and related plasmonic effects*. Elsevier (cited on pages - 30, 36).
-

-
- Ledwith, Deirdre M, Aine M Whelan, and John M Kelly (2007). "A rapid, straightforward method for controlling the morphology of stable silver nanoparticles". In: *Journal of Materials Chemistry* 17.23, pp. 2459–2464 (cited on page - 141).
- Lee, Gil-Jae et al. (2004). "Preparation of silver nanorods through the control of temperature and pH of reaction medium". In: *Materials Chemistry and Physics* 84.2-3, pp. 197–204 (cited on page - 143).
- Lee, Kyeong-Seok and Mostafa A El-Sayed (2005). "Dependence of the enhanced optical scattering efficiency relative to that of absorption for gold metal nanorods on aspect ratio, size, end-cap shape, and medium refractive index". In: *The Journal of Physical Chemistry B* 109.43, pp. 20331–20338 (cited on page - 33).
- Li, Chen et al. (2015). "Large Stokes shift and high efficiency luminescent solar concentrator incorporated with CuInS₂/ZnS quantum dots". In: *Scientific reports* 5, p. 17777 (cited on page - 22).
- Liao, Hongwei and Jason H Hafner (2005). "Gold nanorod bioconjugates". In: *Chemistry of Materials* 17.18, pp. 4636–4641 (cited on page - 87).
- Liao, PF and A Wokaun (1982). "Lightning rod effect in surface enhanced Raman scattering". In: *The Journal of Chemical Physics* 76.1, pp. 751–752 (cited on page - 30).
- Link, Stephan and Mostafa A El-Sayed (2003). "Optical properties and ultrafast dynamics of metallic nanocrystals". In: *Annual review of physical chemistry* 54.1, pp. 331–366 (cited on page - 31).
- Liu, Mingzhao and Philippe Guyot-Sionnest (2004). "Synthesis and optical characterization of Au/Ag core/shell nanorods". In: *The Journal of Physical Chemistry B* 108.19, pp. 5882–5888 (cited on pages - 41, 42).
- Liu, Si-Yun et al. (2013). "Simultaneous excitation and emission enhancement of fluorescence assisted by double plasmon modes of gold nanorods". In: *The Journal of Physical Chemistry C* 117.20, pp. 10636–10642 (cited on page - 116).
- Luque, Antonio and Steven Hegedus (2003). *Photovoltaic science and engineering*. Wiley Online Library (cited on page - 11).
-

-
- Maier, Stefan Alexander (2007). *Plasmonics: fundamentals and applications*. Springer Science & Business Media (cited on pages - 28, 29).
- Malola, Sami et al. (2013). "Birth of the localized surface plasmon resonance in monolayer-protected gold nanoclusters". In: *Acs Nano* 7.11, pp. 10263–10270 (cited on page - 31).
- Man, SQ et al. (2007). "Energy transfer in Pr³⁺/Yb³⁺ codoped tellurite glasses". In: *Optical Materials* 30.2, pp. 334–337 (cited on page - 22).
- Mateen, Fahad et al. (2017). "Metal nanoparticles based stack structured plasmonic luminescent solar concentrator". In: *Solar Energy* 155, pp. 934–941 (cited on pages - 25, 26).
- Mateen, Fahad et al. (2019). "Nitrogen-doped carbon quantum dot based luminescent solar concentrator coupled with polymer dispersed liquid crystal device for smart management of solar spectrum". In: *Solar Energy* 178, pp. 48–55 (cited on pages - 22, 23).
- Mayer, Kathryn M et al. (2010). "A single molecule immunoassay by localized surface plasmon resonance". In: *Nanotechnology* 21.25, p. 255503 (cited on page - 32).
- Meinardi, Francesco, Francesco Bruni, and Sergio Brovelli (2017). "Luminescent solar concentrators for building-integrated photovoltaics". In: *Nature Reviews Materials* 2.12, p. 17072 (cited on pages - 5, 26).
- Meinardi, Francesco et al. (2015). "Highly efficient large-area colourless luminescent solar concentrators using heavy-metal-free colloidal quantum dots". In: *Nature nanotechnology* 10.10, p. 878 (cited on page - 22).
- Meinardi, Francesco et al. (2017). "Highly efficient luminescent solar concentrators based on earth-abundant indirect-bandgap silicon quantum dots". In: *Nature Photonics* 11.3, p. 177 (cited on pages - 22, 23).
- Mello Donegá, Celso de (2011). "Synthesis and properties of colloidal heteronanocrystals". In: *Chemical Society Reviews* 40.3, pp. 1512–1546 (cited on page - 16).
-

-
- Micic, Olga I et al. (1994). "Synthesis and characterization of InP quantum dots".
In: *The Journal of Physical Chemistry* 98.19, pp. 4966–4969 (cited on page - 16).
- Mie, Gustav (1908). "Beitrage zur Optik truber Medien, speziell kolloidaler Metallosungen". In: *Annalen der physik* 330.3, pp. 377–445 (cited on page - 27).
- MIT (2015). *Future of Solar Energy* (cited on page - 2).
- Mokri, Alaeddine and Mahieddine Emziane (2011). "Concentrator photovoltaic technologies and market: a critical review". In: *World Renewable Energy Congress-Sweden; 8-13 May; 2011; Linköping; Sweden*. 057. Linköping University Electronic Press, pp. 2738–2742 (cited on page - 4).
- Moraitis, P, REI Schropp, and WGJHM van Sark (2018). "Nanoparticles for luminescent solar concentrators-A review". In: *Optical Materials* 84, pp. 636–645 (cited on page - 15).
- Moudam, Omar et al. (2009). "Europium complexes with high total photoluminescence quantum yields in solution and in PMMA". In: *Chemical Communications* 43, pp. 6649–6651 (cited on page - 22).
- Mulder, Carlijn L et al. (2009). "Luminescent solar concentrators employing phycobilisomes". In: *Advanced Materials* 21.31, pp. 3181–3185 (cited on page - 21).
- Mulder, Carlijn L et al. (2010). "Dye alignment in luminescent solar concentrators: I. Vertical alignment for improved waveguide coupling". In: *Optics Express* 18.101, A79–A90 (cited on page - 24).
- Mulvaney, Paul, Michael Giersig, and Arnim Henglein (1993). "Electrochemistry of multilayer colloids: preparation and absorption spectrum of gold-coated silver particles". In: *The Journal of Physical Chemistry* 97.27, pp. 7061–7064 (cited on page - 39).
- Murphy, Catherine J et al. (2008). "Chemical sensing and imaging with metallic nanorods". In: *Chemical Communications* 5, pp. 544–557 (cited on page - 30).
- Needell, David R et al. (2018). "Design criteria for micro-optical tandem luminescent solar concentrators". In: *IEEE Journal of Photovoltaics* 99, pp. 1–9 (cited on page - 24).
-

-
- Nikoobakht, Babak and Mostafa A El-Sayed (2001). “Evidence for bilayer assembly of cationic surfactants on the surface of gold nanorods”. In: *Langmuir* 17.20, pp. 6368–6374 (cited on page - 86).
- Nikoobakht, Babak and Mostafa A El-Sayed (2003). “Preparation and growth mechanism of gold nanorods (NRs) using seed-mediated growth method”. In: *Chemistry of Materials* 15.10, pp. 1957–1962 (cited on pages - 40, 71, 76).
- Novotny, Lukas (1996). “Single molecule fluorescence in inhomogeneous environments”. In: *Applied physics letters* 69.25, pp. 3806–3808 (cited on page - 36).
- NREL Cell Efficiency chart (2018). URL: <https://www.nrel.gov/pv/cell-efficiency.html> (cited on page - 4).
- Okuno, Yoshifumi et al. (2008). “Rapid formation of silver shells on gold nanorods in a micellar solution of hexadecyltrimethylammonium chloride”. In: *Chemistry letters* 38.1, pp. 60–61 (cited on page - 42).
- Okuno, Yoshifumi et al. (2010). “Uniform and controllable preparation of Au–Ag core–shell nanorods using anisotropic silver shell formation on gold nanorods”. In: *Nanoscale* 2.8, pp. 1489–1493 (cited on page - 42).
- Oliveira, Michele Cândida Carvalho de et al. (2019). “Comparison and analysis of performance and degradation differences of crystalline-Si photovoltaic modules after 15-years of field operation”. In: *Solar Energy* 191, pp. 235–250 (cited on page - 59).
- Olson, RW, Roger F Loring, and MD Fayer (1981). “Luminescent solar concentrators and the reabsorption problem”. In: *Applied optics* 20.17, pp. 2934–2940 (cited on pages - 21, 116).
- Optical-grade Spectralon material SRM-990 datasheet. URL: https://www.labsphere.com/site/assets/files/1827/pb-13021-000_rev_03_og_spectralon-1.pdf (cited on page - 57).
- Outlook, BP Energy (2012). *energy outlook 2030*. BP Publishers: London (cited on page - 1).
-

-
- Parent, C et al. (1986). "Nd³⁺–Yb³⁺ energy transfer in glasses with composition close to LiLnP₄O₁₂ metaphosphate (Ln= La, Nd, Yb)". In: *Journal of luminescence* 36.1, pp. 49–55 (cited on page - 17).
- Peters, M et al. (2007). "Application of photonic structures on fluorescent concentrators". In: *Proceedings of the 22nd European Photovoltaic Solar Energy Conference*, pp. 177–81 (cited on page - 24).
- Prescott, Stuart W and Paul Mulvaney (2006). "Gold nanorod extinction spectra". In: *Journal of applied physics* 99.12, p. 123504 (cited on page - 31).
- Proise, Florian (2014). "Study and realisation of micro/nano photovoltaic cells and their concentration systems". PhD thesis. Paris 6 (cited on page - 11).
- Rafiee, Mehran (2019). "Largescale Advanced Luminescent Solar Devices for Building Integration". PhD thesis. Trinity College, University of Dublin (cited on page - 138).
- Raga, Sonia R and Francisco Fabregat-Santiago (2013). "Temperature effects in dye-sensitized solar cells". In: *Physical Chemistry Chemical Physics* 15.7, pp. 2328–2336 (cited on page - 126).
- Rahme, Kamil et al. (2013). "Highly stable PEGylated gold nanoparticles in water: applications in biology and catalysis". In: *RSC advances* 3.43, pp. 21016–21024 (cited on page - 87).
- Reda, SM (2007). "Stability and photodegradation of phthalocyanines and hematoporphyrin doped PMMA as solar concentrators". In: *Solar Energy* 81.6, pp. 755–760 (cited on page - 21).
- Reinders, Angèle HME et al. (2016). "Leaf roof—Designing luminescent solar concentrating PV roof tiles". In: *2016 IEEE 43rd Photovoltaic Specialists Conference (PVSC)*. IEEE, pp. 3447–3451 (cited on page - 15).
- Reisfeld, R and Y Kalisky (1981). "Nd³⁺ and Yb³⁺ germanate and tellurite glasses for fluorescent solar energy collectors". In: *Chemical Physics Letters* 80.1, pp. 178–183 (cited on pages - 16, 17).
-

-
- Reisfeld, Renata and Christian K Jørgensen (1982). "Luminescent solar concentrators for energy conversion". In: *Solar Energy Materials*. Springer, pp. 1–36 (cited on page - 13).
- Resch-Genger, Ute et al. (2008). "Quantum dots versus organic dyes as fluorescent labels". In: *Nature methods* 5.9, p. 763 (cited on page - 16).
- Rostro-Kohanloo, Betty C et al. (2009). "The stabilization and targeting of surfactant-synthesized gold nanorods". In: *Nanotechnology* 20.43, p. 434005 (cited on page - 87).
- Rurack, Knut and Monika Spieles (2011). "Fluorescence quantum yields of a series of red and near-infrared dyes emitting at 600- 1000 nm". In: *Analytical chemistry* 83.4, pp. 1232–1242 (cited on page - 22).
- Sakr, Mahmoud E and MTA Kana (2014). "Fluorescence enhancement/quenching of pyrromethene laser dyes hybridized with gold nanoparticles". In: *Arab Journal of Nuclear Science and Applications* 47.1, pp. 86–98 (cited on page - 120).
- Sanguineti, Alessandro et al. (2013). "High Stokes shift perylene dyes for luminescent solar concentrators". In: *Chemical Communications* 49.16, pp. 1618–1620 (cited on page - 22).
- Sansregret, J et al. (1983). "Light transport in planar luminescent solar concentrators: the role of DCM self-absorption". In: *Applied optics* 22.4, pp. 573–577 (cited on page - 21).
- Sark, Wilfried GJHM van (2007). "Teaching the relation between solar cell efficiency and annual energy yield". In: *European journal of physics* 28.3, p. 415 (cited on page - 129).
- Scarabelli, Leonardo et al. (2015). *A tips and tricks practical guide to the synthesis of gold nanorods* (cited on page - 70).
- SETHI, ARUNIMA et al. (2019). "A unified methodology for fabrication and quantification of gold nanorods, gold core silver shell nanocuboids and their polymer nanocomposites". In: *Langmuir* (cited on page - 84).
-

-
- Shah, AV et al. (2004). “Thin-film silicon solar cell technology”. In: *Progress in photovoltaics: Research and applications* 12.2-3, pp. 113–142 (cited on page - 3).
- Sharma, Vivek, Kyoungweon Park, and Mohan Srinivasarao (2009). “Shape separation of gold nanorods using centrifugation”. In: *Proceedings of the National Academy of Sciences* 106.13, pp. 4981–4985 (cited on pages - 48, 76).
- Shcherbatyuk, GV et al. (2010). “Viability of using near infrared PbS quantum dots as active materials in luminescent solar concentrators”. In: *Applied Physics Letters* 96.19, p. 191901 (cited on pages - 22, 23).
- Shockley, William and Hans J Queisser (1961). “Detailed balance limit of efficiency of p-n junction solar cells”. In: *Journal of applied physics* 32.3, pp. 510–519 (cited on page - 11).
- Sholin, V, JD Olson, and SA Carter (2007). “Semiconducting polymers and quantum dots in luminescent solar concentrators for solar energy harvesting”. In: *Journal of applied physics* 101.12, p. 123114 (cited on page - 16).
- Silver, P et al. (2009). “Synthesis of size-controlled faceted tunable plasmonic properties and self-assembly of these nanorods”. In: *ACS Nano* 3, pp. 21–26 (cited on page - 147).
- Slooff, Lenneke H et al. (2008). “A luminescent solar concentrator with 7.1% power conversion efficiency”. In: *physica status solidi (RRL)–Rapid Research Letters* 2.6, pp. 257–259 (cited on page - 22).
- Smestad, G et al. (1990). “The thermodynamic limits of light concentrators”. In: *Solar Energy Materials* 21.2-3, pp. 99–111 (cited on pages - 12, 17).
- Smith, Danielle K, Nathan R Miller, and Brian A Korgel (2009). “Iodide in CTAB prevents gold nanorod formation”. In: *Langmuir* 25.16, pp. 9518–9524 (cited on page - 75).
- SolarEuropa PVGIS. URL: <http://re.jrc.ec.europa.eu/pvgis/apps4/pvest.php> (cited on pages - 13, 129).
-

-
- Song, Hyung-Jun et al. (2017). "Performance limits of luminescent solar concentrators tested with seed/quantum-well quantum dots in a selective-reflector-based optical cavity". In: *Nano letters* 18.1, pp. 395–404 (cited on page - 24).
- Surve, Megha, Victor Pryamitsyn, and Venkat Ganesan (2007). "Dispersion and percolation transitions of nanorods in polymer solutions". In: *Macromolecules* 40.2, pp. 344–354 (cited on page - 92).
- Tebbe, Moritz et al. (2015). "Silver-overgrowth-induced changes in intrinsic optical properties of gold nanorods: From noninvasive monitoring of growth kinetics to tailoring internal mirror charges". In: *The Journal of Physical Chemistry C* 119.17, pp. 9513–9523 (cited on pages - 41–43).
- Thermocouple Selection Guide* (2019). URL: <https://docs-emea.rs-online.com/webdocs/15e5/0900766b815e5302.pdf> (cited on page - 65).
- Thierry, Benjamin et al. (2009). "A robust procedure for the functionalization of gold nanorods and noble metal nanoparticles". In: *Chemical Communications* 13, pp. 1724–1726 (cited on page - 87).
- Toscano, Giuseppe et al. (2012). "Surface-enhanced Raman spectroscopy: nonlocal limitations". In: *Optics letters* 37.13, pp. 2538–2540 (cited on page - 30).
- Van Sark, Wilfried GJHM et al. (2008). "Luminescent Solar Concentrators-A review of recent results". In: *Optics Express* 16.26, pp. 21773–21792 (cited on pages - 15, 22).
- Viehmann, W and RL Frost (1979). "Thin film waveshifter coatings for fluorescent radiation converters". In: *Nuclear Instruments and Methods* 167.3, pp. 405–415 (cited on page - 25).
- Wang, Tongxin et al. (2011a). "Luminescent solar concentrator employing rare earth complex with zero self-absorption loss". In: *Solar Energy* 85.11, pp. 2571–2579 (cited on page - 22).
- Wang, Xin et al. (2011b). "Europium complex doped luminescent solar concentrators with extended absorption range from UV to visible region". In: *Solar Energy* 85.9, pp. 2179–2184 (cited on page - 22).
-

-
- Wang, Zijun et al. (2018). "Carbon dots based nanocomposite thin film for highly efficient luminescent solar concentrators". In: *Organic Electronics* 62, pp. 284–289 (cited on page - 23).
- Weber, WH and John Lambe (1976). "Luminescent greenhouse collector for solar radiation". In: *Applied optics* 15.10, pp. 2299–2300 (cited on page - 13).
- Werner, Jürgen H, Julian Mattheis, and Uwe Rau (2005). "Efficiency limitations of polycrystalline thin film solar cells: case of Cu (In, Ga) Se₂". In: *Thin Solid Films* 480, pp. 399–409 (cited on page - 4).
- Wilson, Lindsay Robert (2010). "Luminescent solar concentrators: a study of optical properties, re-absorption and device optimisation". PhD thesis. Heriot-Watt University (cited on page - 96).
- Wilson, LR and BS Richards (2009). "Measurement method for PLQY of fluorescent organic dyes in PMMA for luminescent solar concentrators". In: *Applied Optics* 48, pp. 212–220 (cited on pages - 15, 21, 57, 96).
- Wu, Chunfang, Xue Zhou, and Jie Wei (2015). "Localized surface plasmon resonance of silver nanotriangles synthesized by a versatile solution reaction". In: *Nanoscale research letters* 10.1, p. 354 (cited on page - 145).
- Wu, Kaifeng, Hongbo Li, and Victor I Klimov (2018). "Tandem luminescent solar concentrators based on engineered quantum dots". In: *Nature Photonics* 12.2, p. 105 (cited on pages - 22, 23).
- Xia, Younan and Naomi J Halas (2005). "Shape-controlled synthesis and surface plasmonic properties of metallic nanostructures". In: *MRS bulletin* 30.5, pp. 338–348 (cited on page - 30).
- Xu, Xiaoyou et al. (2004). "Electrophoretic analysis and purification of fluorescent single-walled carbon nanotube fragments". In: *Journal of the American Chemical Society* 126.40, pp. 12736–12737 (cited on page - 23).
- Yablonoitch, Eli (1980). "Thermodynamics of the fluorescent planar concentrator". In: *JOSA* 70.11, pp. 1362–1363 (cited on page - 17).
-

-
- Yu, Yu-Ying et al. (1997). "Gold nanorods: electrochemical synthesis and optical properties". In: *The Journal of Physical Chemistry B* 101.34, pp. 6661–6664 (cited on page - 76).
- Zande, Bianca MI van der, Ger JM Koper, and Henk NW Lekkerkerker (1999). "Alignment of rod-shaped gold particles by electric fields". In: *The Journal of Physical Chemistry B* 103.28, pp. 5754–5760 (cited on page - 38).
- Zande, Bianca MI Van der et al. (2000). "Colloidal dispersions of gold rods: synthesis and optical properties". In: *Langmuir* 16.2, pp. 451–458 (cited on page - 39).
- Zastrow, Armin (1994). "Physics and applications of fluorescent concentrators: a review". In: *Optical Materials Technology for Energy Efficiency and Solar Energy Conversion XIII*. Vol. 2255. International Society for Optics and Photonics, pp. 534–548 (cited on page - 20).
- Zhao, Haiguang et al. (2016). "Absorption Enhancement in Giant Core/Alloyed-Shell Quantum Dots for Luminescent Solar Concentrator". In: *Small* 12.38, pp. 5354–5365 (cited on pages - 22, 23).
- Ziegler, John Paul et al. (2014). *Luminescent solar concentrator*. US Patent 8,866,001 (cited on page - 22).
- Zuloaga, Jorge and Peter Nordlander (2011). "On the energy shift between near-field and far-field peak intensities in localized plasmon systems". In: *Nano letters* 11.3, pp. 1280–1283 (cited on page - 27).
-